UNIVERSITY of CALIFORNIA
Santa Barbara

Supersoft Emission from Thermonuclear Burning on Hydrogen-Accreting White Dwarfs

A dissertation submitted in partial satisfaction of the
requirements for the degree of

Doctor of Philosophy

in

Physics

by

William Michael Wolf

Committee in charge:

Professor Lars Bildsten, Co-chair

Professor D. Andrew Howell, Co-chair

Professor Omer Blaes

September 2017

The dissertation of William Michael Wolf is approved:

Professor Omer Blaes

Professor D. Andrew Howell, Co-chair

Professor Lars Bildsten, Co-chair

August 2017

To my father, Michael Wolf, who helped build my passion for Astronomy when he helped me build my first telescope.

Acknowledgements

The work in this dissertation could not have been completed without the help of a great number of people. Chief among them is my advisor, Lars Bildsten. Lars has been a wonderful mentor through my graduate career. He has taught me how to think like a scientist and instilled in me the values necessary to have fruitful collaborations in an open scientific environment. The depth of his patience and his uncanny ability to put me back on track when I start to wander down a rabit hole cannot be overstated.

I also thank Andy Howell, my co-advisor, who gave me the valuable perspective of an observer. While my theoretical work with Lars has always had an eye towards explaining and predicting observations, working with Andy has allowed me to get my hands dirty working with datasets and thinking about the minutiae of observational astronomy. This perspective has made me into the well-rounded astrophysicist I am today.

A large part of this work relied on the open source software instrument `MESA`. I would not have been nearly as productive without access to `MESA`, so I must thank the `MESA` community in general, and the lead developer, Bill Paxton, in particular. The `MESA` community has made my work fit into a larger whole, where research is done out in the open and can be fully reproduced by anyone who wishes. Open, reproducible science is now part of my academic DNA.

The community of astronomers at UCSB has provided a warm environment for my academic growth. Through teaching assignments, astronomy seminars, journal clubs, and daily tea, I found a scholarly home and an outlet for energy outside of my research as webmaster and a seminar organizer. Specific graduate students and postdocs have also been indisepensible. I thank Federica Bianco, Ben Dilday, and Melissa Graham for getting me started with my first project when I knew nothing about using my computer for astronomy research. I thank Matteo Cantiello, Ben Brown, Sumin Tang, and Jim Fuller for many stimulating conversations related to my reserach and stellar astrophysics in general. I give an especially big thanks to Kevin Moore for serving as a mentoring graduate student in my early years, and to Jared Brooks and Evan Bauer for somehow doing the same even as younger graduate students.

Outside of the department, I have relied on many friends for support and for non-academic social interaction when I didn't want to think about stars for a bit. In particular, my roommates over the years, Thomas Malkowski, Hunter Banks, Srinivasan Venkatesh, Brayden Ware, Eric Rind, Sara Sterphone, and Bill Flaherty have provided a bedrock for my social life. Coming home to these people every night has been a delight and helped form a support system while away from my family. I also thank the faith community at Saint Mark's University Parish in Isla Vista. In particular, I've appreciated how the music ministry there has given me an outlet for my faith as well as my passion for singing and playing piano.

Saint Mark's also introduced me to my beloved girlfriend, Jael Martínez, who in the two years I've known her has become the love of my life. Her magnetic personality and stimulating conversation, at times, made it difficult to focus on work. But more often,

her genuine interest in my studies and unwavering encouragment inspired me to redouble my efforts to complete my research.

Finally, I must thank my family for their support and love. Our family has always had a passion for education in math and science. I grew up with my mom, Missy, teaching high school mathematics. My sister Lisa also taught mathematics before moving on to work in various capacities for ACT, helping schools measure the growth of their students. My sister Gina, now also teaches high school mathematics. My sister Susie pursued a Ph. D. in mathematics and now teaches it as a professor. All, in their own way, have provided models for me to follow in their personal and professional lives. Finally, I must acknowledge my father, Mike Wolf, to whom this dissertation is dedicated. He instilled a passion for astronomy in me at a young age when he helped me build my first telescope, an eight-inch Newtonian reflector. That passion never died and has taken me to the edge of our knowledge of stellar astrophysics. Unfortunately Mike died unexpectedly just as I was getting started with the work that became chapter 2 of this dissertation. I know he would be as proud as anyone of this achievement, and I will forever remember him as the wonderful man he was and how instrumental he was at getting me to this point.

Curriculum Vitae

William M. Wolf

EDUCATION

Doctor of Philosophy, Physics — expected September 2017
University of California, Santa Barbara, Santa Barbara, CA
Advisors: Lars Bildsten and Andy Howell
Thesis: Supersoft Emission from Hydrogen-Accreting White Dwarfs

Master of Arts, Physics — April 2013
University of California, Santa Barbara, Santa Barbara, CA
Advisors: Lars Bildsten and Andy Howell

Bachelor of Science, Physics — May 2010
Eastern Illinois University, Charleston, IL
University Honors; Summa Cum Laude
Summer 2009 REU at University of Rochester

- Advisor: Eric Blackman
- Topic: Astrophysical Jets

Bachelor of Arts, Mathematics — May 2010
Eastern Illinois University, Charleston, IL
University Honors; Summa Cum Laude
Departmental Honors

- Advisor: Leonardo Comerford
- Thesis: Conjugacy in Hyperbolic Groups

ACADEMIC EXPERIENCE

Research Assistant — June 2011 – Present
Department of Physics, UC Santa Barbara

- Studied hydrogen accretion and burning on white dwarf stars, focusing on the resulting emission of supersoft X-rays. Worked primarily with Lars Bildsten.
- Searched for superluminous supernovae in the Supernova Legacy Survey dataset. Worked primarily with Andy Howell on this project.

Teaching Assistant — September 2010 – May 2016
Department of Physics, UC Santa Barbara

- Served as an instructor for lab sections and aide in open lab time for the following courses:
  - PHYS 134: Observational Astrophysics (Spring 2012)
  - PHYS 3L: Introductory Physics for Engineers Lab (Fall 2011, Fall 2010)

- Served as a facilitator for discussion sections and/or a grader for the following courses:
  - PHYS 133 Galaxies and Cosmology (Winter 2012)
  - PHYS 1: Introductory Physics for Engineers (Winter 2012)
  - PHYS 133: Stellar Structure (Fall 2011, Fall 2010)
  - ASTRO 2: Introductory Cosmology (Spring 2011)
  - ASTRO 1: Introductory Astronomy (Winter 2011)
- Helped with instruction of the graduate course PHYS 232: Stellar Structure as a resource for students in using the 1D stellar evolution software instrument `MESA star` (Fall 2013) and as a guest lecturer (Spring 2016).

Mentor June 2013 – June 2015
Department of Physics, UC Santa Barbara

- Closely mentored a visiting undergraduate student, Timothy Cunningham, on a project that would later become his Masters' thesis. Taught concepts of radiative transfer and stellar structure as well as more general skills like figure design and academic writing. Timothy is now a doctoral student at the University of Warwick.

PUBLICATIONS

7. Prajs, S.; Sullivan, M.; Smith, M.; Levan, A.; Karpenka, N. V.; Edwards, T. D. P.; Walker, C. R.; **Wolf, William M.**; Balland, C.; Carlberg, R.; Howell, A.; Lidman, C.; Pain, R.; Pritchet, C.; Ruhlmann-Kleider, V. The Volumetric Rate of Superluminous Supernovae at z 1. 2016, Monthly Notices of the Royal Astronomical Society. Volume 463. Issue 2. 16pp.

6. Arcavi, I.; **Wolf, William M.**; Howell, D. A.; Bildsten, L.; Leloudas, G.; Hardin, D.; Prajs, S.; Perley, D. A.; Svirski, G.; Gal-Yam, A.; Katz, B.; McCully, C.; Cenko, S. B.; Lidman, C.; Sullivan, M.; Valenti, S.; Astier, P.; Balland, C.; Carlberg, R. G.; Conley, A.; Fouchez, D.; Guy, J.; Pain, R.; Palanque-Delabrouille, N.; Perrett, K.; Pritchet, C. J.; Regnault, N.; Rich, J.; and Ruhlmann-Kleider, V. Rapidly Rising Transients in the Supernova-Superluminous Supernova Gap. 2016, The Astrophysical Journal, Volume 819, Issue 1, article id. 35, 22pp.

5. Soraisam, M. D.; Gilfanov, M.; **Wolf, William M.**; and Bildsten, L. Population of post-nova supersoft X-ray Sources. 2016, The Monthly Notices of the Royal Astronomical Society, Volume 455, Issue 1, p.668-679. January 2016.

4. Cunningham T.; **Wolf, William M.**; and Bildsten, L. Photoionization Heating of Nova Ejecta by the Post-outburst Supersoft Source. 2015, The Astrophysical Journal, Volume 803, Issue 3, article id. 76, 7pp.

3. Tang, S.; Kaplan, David L.; Phinney, E. S.; Prince, Thomas A.; Breton, Rene P.; Bellm, E.; Bildsten, L.; Cao, Y.; Kong, A. K. H.; Perley, D. A.; Sesar, B.; **Wolf, William M.**; and Yen, T.-C. Identification of the Optical Counterpart

Fermi Black Widow Millisecond Pulsar PSR J1544+4937. 2014, The Astrophysical Journal Letters, Volume 791, article id. L5, 5pp.

2. Tang, S.; Bildsten, L.; **Wolf, William M.**; Li, K. L.; Hong, A. K. H.; Cao, Y.; Cenko, B. S.; De Cia, A.; Kasliwal, M. M.; Kulkarni, S. R.; Laher, R. R., Masci; F., Nugent, P. E.; Perley, D. A.; Prince, T. A.; and Surace, J. An Accreting White Dwarf Near the Chandrasekhar Limit in the Andromeda Galaxy. 2014, The Astrophysical Journal, Volume 786, Issue 1, article id. 61, 8pp.

1. **Wolf, William M.**; Bildsten, L.; Brooks, J.; and Paxton, B. 2013. Hydrogen Burning on Accreting White Dwarfs: Stability, Recurrent Novae, and the Post-nova Supersoft Phase. 2013, The Astrophysical Journal, Volume 777, Issue 2, article id. 136, 15 pp.

MANUSCRIPT IN PREPARATION

Wolf, William M.; Townsend, R. H. M.; and Bildsten, L. Oscillations in Post-Outburst Novae. To be submitted to the Astrophysical Journal August 2017.

LECTURES

Public Lectures

2. **Wolf, William M.** Clasical Novae: Inside Out Stars Evolving in Reverse. Astronomy on Tap Santa Barbara, M8RX, Santa Barbara, CA, USA, November 16, 2016.

1. **Wolf, William M.** Stellar Explosions. Retirement Symposium for Professor Jim Conwell, Eastern Illinois University, Charleston, Illinois, USA, November 6, 2015.

Invited Talks

3. **Wolf, William M.** Introduction to MESA. ZTF Summer Undergraduate Institute. California Institute of Technology, Pasadena, California, USA, June 21, 2017.

2. **Wolf, William M.** Theory of Nova Thermonuclear Runaways. Conference on Shocks and Particle Acceleration in Novae and Supernovae. Simons Foundation and Columbia University, New York, New York, USA, June 23-25, 2016.

1. **Wolf, William M.** Nova Populations: Models vs. Observations. Stellar Remnants at the Junction: Comparing Accreting White Dwarfs, Neutron Stars, and Black Holess. Junction, Texas, USA, May 2-6, 2016.

Contributed Talks

6. **Wolf, William M.** & Bildsten, L. Helium Flashes on Steadily Burning White Dwarfs. Twentieth European White Dwarf Workshop. University of Warwick, Coventry, CV4 7AL, United Kingdom, July 25 - 19, 2016.

5. **Wolf, William M.**, Cunningham, T., & Bildsten, L. Photoionization Heating of Nova Ejecta. Physics of Cataclysmic and Compact Binaries. Columbia University, New York, USA, October 30 - November 2, 2014.

4. **Wolf, William M.**, Tang, S., Bildsten, L., et al. Post-nova Supersoft Sources, Recurrent Novae, and the Fastest Recurrent Novae Yet Discovered. Type Ia Supernovae: Progenitors, Explosions, and Cosmology. University of Chicago, Chicago, USA, September 15-19, 2014.

3. **Wolf, William M.**, Bildsten, L. Helium Flashes on Steadily Burning White Dwarfs. Thirteenth Annual Theoretical Astrophysics in Southern California Meeting, UCLA, Los Angeles, California, USA, December, 2013.

2. **Wolf, William M.**, Bildsten, L., Brooks, J., and Paxton, B. Steady State Burning on White Dwarfs and Recurrent Novae. Observational Signatures of Type Ia Supernova Progenitors II, Lorentz Center, Leiden, The Netherlands, September 2013.

1. **Wolf, William M.**, Bildsten, L., Brooks, J., and Paxton, B. MESA Models for Accreting White Dwarfs with Stable Burning. Twelfth Annual Theoretical Astrophysics in Southern California Meeting, Carnegie Observatories, Pasadena, California, USA, November, 2012.

SERVICE

MESA Users List 2012 – Present

- Ask and answer questions relating to the installation and use of the `MESA` software instrument.
- See archive of contributions here: `http://bit.ly/2pH0VIa`

Teaching Assistant, MESA Summer School Summers 2012 – Present

- Helped to organize and execute laboratory excercies for the annual `MESA` summer school.
- Assisted the following lecturers and topics:
  - Jim Fuller: Wave Transport in Stars August 2016
  - Craig Wheeler: Massive Star Explosions August 2015
  - Lars Bildsten: Stellar Response to Mass Loss August 2014
  - Lars Bildsten: Helium Core Burning August 2013
  - Lars Bildsten: Accreting White Dwarfs August 2012

Referee, Astrophysical Journal 2014 – Present

- Refereed four articles for publication in the Astrophysical Journal

Webmaster, UCSB Astronomy and Astrophysics 2014 – 2017

- Completely redesigned website and kept it up to date, accounting for changes in faculty, postdocs, and students. Implemented selected research, faculty search, automatic "recent papers on the arxiv" features.
- `http://www.physics.ucsb.edu/~astrogroup`

COMPUTER SKILLS

- Programming Languages: Ruby, Python, Mathematica, IDL, and Fortran 95
- Markup Languages: LaTeX, Markdown
- Internet Tools: HTML5, CSS3, Javascript (JQuery, CoffeeScript), Bootstrap, Ruby on Rails (Rspec, Cucumber)
- Scientific Packages: Numpy, Scipy, Matplotlib, Tioga
- Scientific Software Instruments: MESA, Cloudy
- Operating Systems: Mac, Unix/Linux.
- Version Control Systems: Git

CODING PROJECTS

Here are several tools I've written to aid in the use of `MESA` and analyzing the data it produces. All are open source and available through Github. These are detailed on the "Projects" section of my web page: `http://wmwolf.github.io/projects/`.

MesaScript

- Powerful domain-specific language for creating complex inlists
- Written in Ruby
- `http://wmwolf.github.io/MesaScript/`

MesaReader

- Eases access to `MESA` output for plotting or analysis
- Python: `http://wmwolf.github.io/py_mesa_reader/`
- Ruby/Tioga: `http://wmwolf.github.io/MESA_Reader/`

Mesa CLI

- Command line interface for automating many common tasks in MESA
- Written in Ruby
- `http://wmwolf.github.io/mesa_cli/`

Abstract

Supersoft Emission from Thermonuclear Burning on Hydrogen-Accreting White Dwarfs

by

William Michael Wolf

Thermonuclear burning of hydrogen on white dwarfs (WDs) is an inevitable occurence for accreting WDs in binary systems. After the onset of thermally-unstable nuclear burning, the WD rapidly expands and ejects much of its hydrogen-rich matter. Once it regains thermal equilibrium, it contracts and becomes a luminous ($L \sim 10^4\ L_\odot$) source of supersoft X-rays. This supersoft phase can last anywhere from days (for novae on massive WDs) to millions of years (for persistent supersoft sources). In this dissertation, we explore how the supersoft phase of accreting WDs proceeds and what observations of it reveal about the underlying WD. We present stellar models of persistent supersoft sources and novae. We then use these models to explain the isothermal nature of the ejecta as observed in the radio. We also use these models to test the efficacy of g-modes excited in the burning layer as an explanation of observed oscillations in the supersoft phase of novae. While we find excited modes, their periods are too short to account for the observed oscillations.

Contents

Chapter 1

Introduction

Most stars end their lives as white dwarfs (WDs). Many, like the sun eventually, simply run out of fuel in their cores, and after expelling their outer envelope in a planetary nebula, they leave behind a hot cinder with a mass on the order of a solar mass and a radius similar to Earth's. This newly born WD slowly cools and crystallizes over timescales comparable to the age of the universe. Other stars in binary systems have their outer envelopes stripped from them in the dance of mass transfer characteristic of interacting binaries, revealing a newborn WD.

WDs' uses as laboratories for basic physics, like diffusion and degenerate equations of state (Fontaine et al., 1977; Saumon et al., 1995; Massacrier et al., 2011; Michaud et al., 2015), as well as their ubiquity as end states of stars, make single WDs an interesting field of their own. But when WDs in binaries accrete matter from a companion, they exhibit rich behavior arising from accretion (e.g. dwarf novae) or thermonuclear burning

(e.g. classical/recurrent novae, supersoft sources). Accreting WDs are also one of the proposed progenitors for type Ia supernovae, but their efficacy in this capacity is still debated (Maoz et al., 2014).

The focus of this dissertation is hydrogen burning on accreting WDs and how that burning influences observations of classical novae, recurrent novae, and supersoft sources across the electromagnetic spectrum. Before diving into these topics, we first visit some basic terms and concepts relevant to accreting WDs and thermonuclear burning in a thin shell.

1.1 Accreting White Dwarfs

The accretion of hydrogen-rich material occurs in several classes of binary systems. The most prominent binary star classes for this work are cataclysmic variables, symbiotic stars, and thermal timescale mass transferring systems. We discuss each of these before outlining how thermonuclear burning occurs in them.

1.1.1 Cataclysmic Variables

Cataclysmic variables are short-period ($P_{\rm orb} \sim 1 - 10$ hours) binary stars consisting of a WD and a low-mass companion star that is filling its Roche lobe and stably transferring material to the WD via an accretion disk (Robinson, 1976). In this configuration, the orbital separation at first shrinks due to angular momentum losses from magnetic braking from the donor ($P_{\rm orb} \gtrsim 3$ hours), transferring mass in the range of

$\dot{M} \sim 10^{-9} - 10^{-7}\ M_{\odot}\ \mathrm{yr}^{-1}$. Once the donor is eroded sufficiently, it becomes fully convective and shrinks inside of its Roche lobe, and magnetic braking ceases to be effective at shrinking the orbit. Instead, gravitational waves slowly bring the binary back into contact at an orbital period of around $P_{\mathrm{orb}} \approx 2$ hours with accretion rates in this regime of $\dot{M} \sim 10^{-12} - 10^{-10}\ M_{\odot}\ \mathrm{yr}^{-1}$.

1.1.2 Symbiotic Stars

At much longer orbital periods of $P_{\mathrm{orb}} \sim 1 - 10$ years, symbiotic stars consist of a WD accreting material captured from the wind of a Red giant star rather than siphoning off material through the binary's inner Lagrange point (Kenyon, 1986; Mikolajewska et al., 1988). Mass transfer rates vary depending on the orbital separation and the intensity of the wind from the donor star, but they are estimated to be in the range of $\dot{M} \sim 10^{-8} - 10^{-5}\ M_{\odot}\ \mathrm{yr}^{-1}$.

1.1.3 Thermal Timescale Mass Transfer Systems

A third means of transferring hydrogen-rich material is through thermal timescale mass transfer as in van den Heuvel et al. (1992); Kahabka & van den Heuvel (1997); Langer et al. (2000). In this scenario, a WD is in a binary system with a more massive star as it leaves the main sequence. After exhausting core hydrogen, the donor star expands on a thermal timescale. At orbital periods of $P_{\mathrm{orb}} \sim$ days, this expanding star overflows its Roche lobe and thermally unstable mass transfer occurs at a rapid pace of $\dot{M} \sim$

$M_{\rm donor}/t_{\rm thermal,donor} \sim 10^{-8} - 10^{-5}\ M_\odot\ {\rm yr}^{-1}$.

1.1.4 Intermittent Accretion

For each of the systems presented above, mass from the donor is usually transferred to the WD surface through an accretion disk (notable exceptions include strongly magnetized WDs where matter is channeled to the poles). These accretion disks host interesting phenomena of their own. In particular, cataclysmic variables with average accretion rates of $\left\langle \dot{M} \right\rangle \lesssim 10^{-9}\ M_\odot\ {\rm yr}^{-1}$ are thermally unstable. For most of the time, these disks deposit mass onto the WD surface at a much smaller rate than mass is added to the disk. After a buildup of matter and a rise in disk temperature, a change in the ionization state causes the disk to rapidly deposit matter until the disk has been depleted of much of its mass. These events are called dwarf novae, and they occur on timescales of months to years. In this work, we consider timescales that are longer than a typical dwarf nova and/or accretion rates above which the disks are perpetually in a "high" state, so throughout this work, any accretion rate $\dot{M}$ is always considered an average value.

1.2 Thermonuclear Shell Burning on White Dwarfs

In the model where a "cold" WD (with central temperature $T_c \lesssim 5 \times 10^7$ K) has a steady supply of hydrogen-rich matter at its surface, three main outcomes are possible, depending on the mass of the WD and the accretion rate $\dot{M}$:

1. High $\dot{M}$: shell flash followed by steady burning in an extended form

2. Intermediate $\dot{M}$: shell flash followed by steady burning in a compact form

3. Low $\dot{M}$: intermittent shell flashes, i.e. novae

In any case, matter accumulates near the surface until a shell flash ensues, after which the longer-term outcome manifests. We now outline the onset and evolution of the shell flash and the subsequent possible outcomes.

1.2.1 A Typical Shell Flash

When deposited onto a WD at nearly any rate, hydrogen-rich material ignites when heating via hydrogen fusion outstrips the radiative cooling from the atmosphere. This occurs when the mass of the hydrogen-rich layer ΔM, reaches a criticial ignition mass $\Delta M_{\rm ign}$ which depends on the WD mass, its core temperature, the rate the matter is accreted $\dot{M}$, and the precise composition of the accreted material (Prialnik & Kovetz, 1995; Townsley & Bildsten, 2004; Yaron et al., 2005; Shen & Bildsten, 2009).

Once an ignition has occurred, the temperature at the base of the hydrogen-rich layer rises rapidly, and the high temperature sensitivity of hydrogen burning via the CNO burning drive convection in the envelope. The convection spreads over the accreted layer until the thermal timescale at the outer convection boundary is comparable to the nuclear heating timescale at the base. At this point, the nuclear luminosity far exceeds the local Eddington luminosity, so the excess luminosity goes into mechanical energy expanding the WD atmosphere to many times its quiescent radius (Fujimoto, 1982b; Iben, 1982). The expansion continues until the nuclear luminosity at the base of the convective region

can be matched by the photospheric luminosity (typically $L \sim 10^4\ L_\odot$), after which the convection dies out and the envelope becomes radiative. If accretion persists through this expansion and if $\dot{M} > \dot{M}_{\rm crit}$, the outcome is option 1 above. Here $\dot{M}_{\rm crit}$ is the rate that hydrogen-rich material is consumed at the base, so matter is accreting faster than the WD can process it to helium. The WD remains inflated as much as the binary allows, and accretion is tempered by mass loss to a net rate of $\dot{M}_{\rm crit}$ (Nomoto et al., 1979).

In most shell flashes, though, $\dot{M} < \dot{M}_{\rm crit}$ and some combination of optically thick winds, binary interaction, and/or dynamical ejection cause the majority of the accreted envelope to be lost from the binary with typical ejecta velocities of $v_{\rm ej} \sim 1000$ km s^{-1} (Bode & Evans, 2008; Prialnik & Kovetz, 1995; Kato & Hachisu, 1994). During this time, the ejecta appear as a bright optical source known as a "nova" (not to be confused with dwarf novae, which are an accretion, rather than thermonuclear phenomenon). Even after becoming optically thin to optical and shorter wavelengths, the ejecta can still be observed in the radio, often taking on a biconical morphology (Bode & Evans, 2008).

After ΔM has been reduced by mass loss to a certain value $\Delta M_{\rm crit}$, the WD shrinks back to a more compact form and mass loss ceases at nearly constant bolometric luminosity $L \sim 10^4\ L_\odot$ (Kato et al., 2014). With such a small size and high luminosity, the WD maintains high effective temperatures of $T_{\rm eff} \sim 10^5 - 10^6$ K. The WD thus shines brightly in the far UV and soft X-rays, and is often referred to as a supersoft source (SSS). If $\dot{M} > \dot{M}_{\rm stable}$, the WD becomes a persistent SSS, remaining so as long as the accretion stream is maintained (option 2 above). Here $\dot{M}_{\rm stable}$ is the minimum rate of

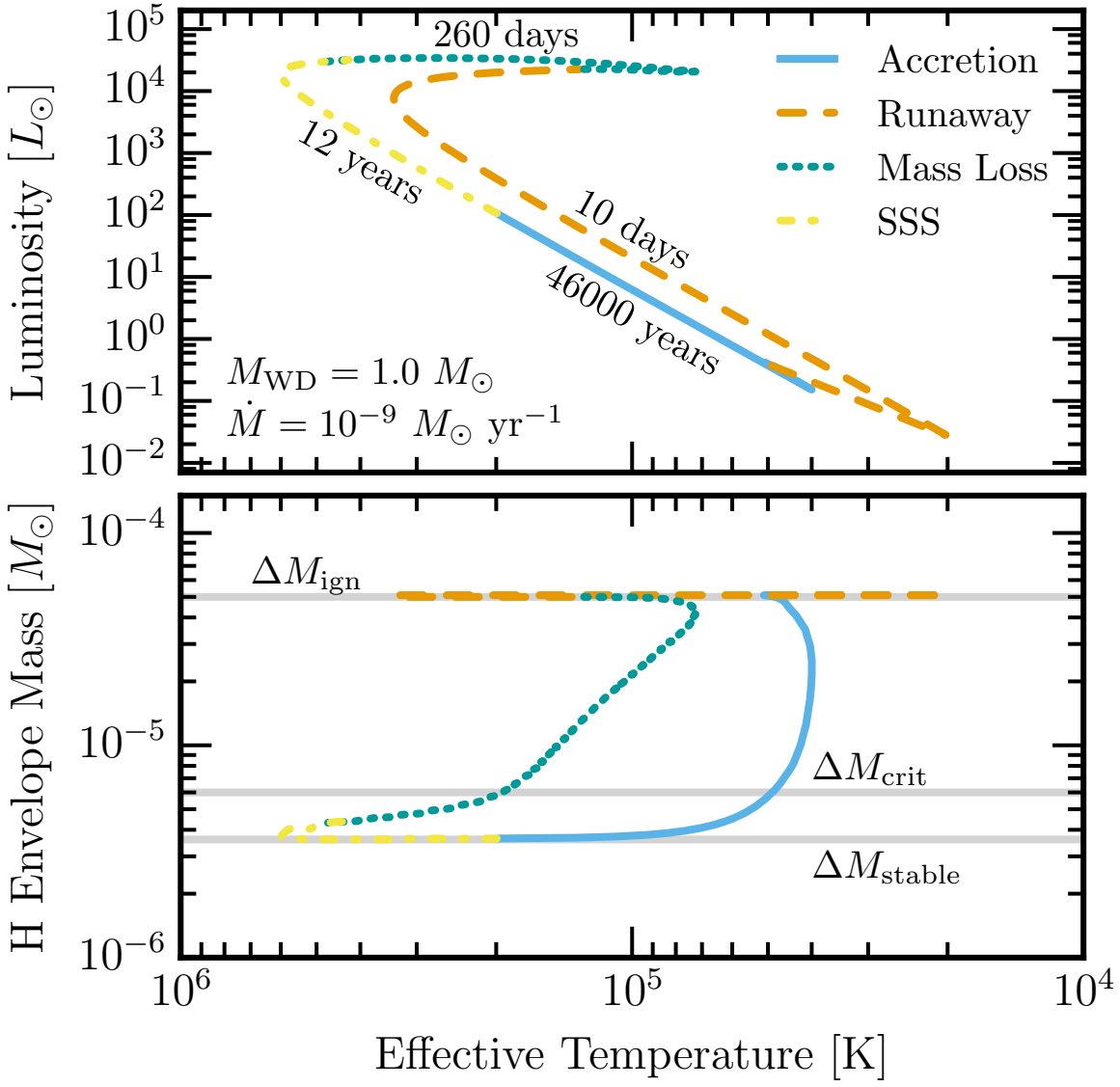

Figure 1.1 A typical nova cycle for a 1.0 $M_\odot$ WD accreting solar material at $10^{-9}\ M_\odot\ {\rm yr}^{-1}$. **Top Panel**: Evolution through the theorist's HR diagram with each distinct phase in a different line style. Time spent in each phase is indicated. **Bottom Panel**: Evolution of the hydrogen-rich envelope's mass with respect to the effective temperature. Values for the critical envelope masses are indicated by horizontal lines.

fuel consumption that allows for stable and steady burning, and its calculation is a main focus of chapter 2.

If $\dot{M} < \dot{M}_{\rm stable}$, nuclear fuel is consumed faster than it can be replenished. The hydrogen layer is eroded via nuclear burning until ΔM drops below some minimum hydrogen layer mass $\Delta M_{\rm stable}$, below which radiative cooling overwhelms nuclear heating, and the WD returns to a cool and quiet accreting state. The long-term outcome is then option 3 above, where the cycle repeats itself, giving rise to classical or recurrent novae on timescales as short as six months (Fujimoto, 1982a; Kato et al., 2014). Note that the distinction between "classical" and "recurrent" novae is a human one. All novae are thought to be recurrent in that they occur over and over again. Classical novae are those that have only been observed in outburst once (they may recur on timescales of tens of thousands of years), whereas recurrent novae are those that have been observed in outburst multiple times (with typical recurrence times of tens of years). Often we will refer to both classes simply as "novae". Figure 1.1 shows the evolution of the envelope mass ΔM for a typical nova cycle as well as its path through the HR diagram.

1.2.2 Utility of the Supersoft Phase

This dissertation aims to characterize persistent SSSs and the post-outburst SSS phase of novae. In doing this, we relate the primary observables of these objects in radio and X-rays to models of SSSs and thus the underlying WD. We find that supersoft emission and its effects on radio emission provide powerful diagnostics for determining the progenitor

systems of persistent SSSs and novae.

1.3 Overview

In chapter 2, we explore how WDs respond to the accretion of solar composition material via steady and stable burning or periodic novae. In chapter 3 we study how the phase of burning after a classical nova influences the thermal state of the ejecta and resulting radio observations. And in chapter 4 we explore how pulsations in this same phase may explain observed oscillations in X-ray data. Finally in chapter 5, we identify some open questions and logcial next steps from this work.

1.4 Permissions and Attributions

1. The content of chapter 2 is the result of a collaboration with Lars Bildsten, Sumin Tang, Bill Paxton, and Jared Brooks, and has previously appeared in Wolf et al. (2013) and Tang et al. (2014). It is reproduced here with the implicit permission of AAS Journals: http://journals.aas.org/authors/apc.html#Reproduction.

2. The content of chapter 3 is the result of a collaboration with Timothy Cunningham and Lars Bildsten, and has previously appeared in Cunningham et al. (2015). It is reproduced here with the implicit permission of AAS Journals: http://journals.aas.org/authors/apc.html#Reproduction.

3. The content of chapter 4 and appendix A is the result of a collaboration with Rich

Townsend and Lars Bildsten, and at the time of submission is being prepared for submission to the Astrophysical Journal.

Chapter 2

Stability, Recurrent Novae, and the Post-Nova Supersoft Phase

In this chapter, we examine the properties of white dwarfs (WDs) accreting hydrogen-rich matter in and near the stable burning regime of accretion rates as modeled by time-dependent calculations done with Modules for Experiments in Stellar Astrophysics (`MESA`). We report the stability boundary for WDs of masses between 0.51 $M_{\odot}$ and 1.34 $M_{\odot}$ as found via time-dependent calculations. We also examine recurrent novae that are accreting at rates close to, but below, the stable burning limit and report their recurrence times. Our dense grid in accretion rates finds the expected minimum possible recurrence times as a function of the WD mass. This enables inferences to be made about the minimum WD mass possible to reach a specific recurrence time. We compare our computational models of post-outburst novae to the stably burning WDs and explicitly

calculate the duration and effective temperature ($T_{\rm eff}$) of the post-novae WD in the supersoft phase. We agree with the measured turnoff time - $T_{\rm eff}$ relation in M31 by Henze and collaborators, infer WD masses in the 1.0-1.3 $M_{\odot}$ range, and predict ejection masses consistent with those observed. We close by commenting on the importance of the hot helium layer generated by stable or unstable hydrogen burning for the short-and long-term evolution of accreting white dwarfs.

2.1 Introduction

The outcome of accretion of hydrogen-rich material onto the surface of a white dwarf (WD) is relevant to classical novae (Gallagher & Starrfield, 1978), recurrent novae, supersoft sources (SSS) (van den Heuvel et al., 1992; Nomoto et al., 2007), and even the single degenerate scenario (SDS) for type Ia supernovae progenitors (Nomoto, 1982; Nomoto et al., 1984; Cassisi et al., 1998). The outcome depends on the mass of the accreting WD, $M_{\rm WD}$, the accretion rate, $\dot{M}$, and the core temperature, T_c (Sienkiewicz, 1980; Townsley & Bildsten, 2004; Yaron et al., 2005; Nomoto et al., 2007; Shen & Bildsten, 2007). If the accretion rate is too large, the burning can't match it, causing the rapidly accreting matter to pile up into a red giant-like structure (Paczynski & Zytkow, 1978; Nomoto et al., 1979). At lower accretion rates, hydrogen can be stably burned to helium at the same rate that is being accreted (Paczynski & Zytkow, 1978; Sienkiewicz, 1980; Iben, 1982; Fujimoto, 1982a; Paczynski, 1983; Livio et al., 1989; Cassisi et al., 1998; Shen & Bildsten, 2007; Nomoto et al., 2007). If the accretion rate is lower yet, the hydrogen supply rate

is too low to match the stably burning luminosity, so a low-luminosity accreting state is realized while hydrogen accumulates until a thermonuclear runaway occurs, quickly burning the hydrogen and driving a radius increase and mass loss from the WD that appears as a classical or recurrent nova.

Understanding these phenomena first requires understanding the physics of stable burning. Previous studies (Sienkiewicz, 1980; Nomoto et al., 2007; Shen & Bildsten, 2007) assumed a steady burning state and studied the stability of their solutions in response to linear perturbations. While numerous time-dependent simulations of WDs accreting hydrogen-rich material are already in the literature, many either started with the matter pre-accreted and studied the ensuing outburst or selected initial conditions which are not erased until several flashes have established asymptotic behavior (Iben, 1982). Only Paczynski & Zytkow (1978), Sion et al. (1979), Iben (1982), Livio et al. (1989), Shara et al. (1993), Kovetz & Prialnik (1994), Cassisi et al. (1998), and Yaron et al. (2005) examined the time-dependent problem for durations long enough to observe multiple flashes or stable burning. To date, there is no comprehensive time-dependent study of WDs accreting solar composition material over the full range of the stable burning regime for a large range of WD masses. Yaron et al. (2005) was the most complete prior effort, but did not calculate a dense grid in $\dot{M}$ space near the lower stability boundary.

WDs accreting just below the stability boundary will go through periodic hydrogen shell flashes on relatively short timescales, or recurrent novae (RNe). There are currently ten known RNe in our galaxy (Schaefer, 2010) with recurrence times on the order of

decades. Those RNe with shortest recurrence times have been understood to be massive WDs (see Figure 9 of Nomoto 1982). Since the measured time between outbursts is often an important factor in estimating $M_{\rm WD}$, we require a solid understanding of the mass-recurrence time relation near the lower stability boundary.

At lower $\dot{M}$'s ($\lesssim 10^{-8}\ M_\odot\,{\rm yr}^{-1}$), WDs undergo classical nova cycles whose recurrence times are too long to measure on human timescales (Yaron et al., 2005). Mass determinations of such systems must then rely on other observed parameters. After a CN outburst, the ejected mass is optically thick, obscuring the view of the hot WD below. After a turn-on time, $t_{\rm on}$, the ejecta becomes optically thin, revealing an SSS. Still later, at some turn-off time $t_{\rm off}$ after the outburst, the X-ray luminosity powered by burning in the hydrogen-rich remnant (Starrfield et al., 1974) decreases and the nova event is over. Hachisu & Kato (2010) have offered a way to fit the observed timescales to models in order to infer $M_{\rm WD}$. Tuchman & Truran (1998) and Sala & Hernanz (2005) argue that the mass left in the hydrogen-rich WD envelope after mass loss is determined primarily by $M_{\rm WD}$ and secondarily by the composition of the envelope. This remnant envelope mass is expected to undergo stable hydrogen burning in the post-outburst SSS phase at nearly constant luminosity. If this remaining envelope mass and luminosity are known as a function $M_{\rm WD}$, the duration of the SSS phase can be predicted, allowing a correlation between the measured turn-off time of a CN and $M_{\rm WD}$. With the increasingly large samples of CNe like that of Henze et al. (2011) in M31 and Schwarz et al. (2011) in our own galaxy, we can now test these methods on a meaningful number of CNe.

In this chapter, we present models of WDs with masses ranging from $M_{\rm WD} = 0.51\ M_\odot$ to 1.34 $M_\odot$ accreting solar composition material as simulated by `MESA` (Paxton et al., 2011; Denissenkov et al., 2013; Paxton et al., 2013). The conditions for stable hydrogen burning are found, as are the characteristics of unstable models. We compare recurrence times to the previous results from Iben (1982), Livio et al. (1989), Cassisi et al. (1998), and Yaron et al. (2005). We start in §2.2 by discussing the input physics used to produce the accreting models. Then in §2.3, we present the relevant background on stable burning as well as the characteristics of our steadily (and stably) burning models. We investigate unstable burning on WDs accreting at rates near, but below, the stable boundary in §2.4 with comparisons to previous time-dependent calculations explored in §2.5. We study applications to classical novae in §2.6 and 2.7, and further implications and questions are addressed in §2.8, where we comment on the inevitable flashes in the accumulating helium layer.

2.2 Simulation Details and Model Building

Initial WD models were created in `MESA` by evolving stars between 4 and 12 $M_\odot$ from ZAMS through the main sequence, RGB, and AGB through to the white dwarf cooling track. Typically when this is done, very small time steps are required to get through the thermal pulses during the AGB phase. To get around this, the convection in the outer envelope is artificially made more efficient so that the full computations need not be followed (Paxton et al., 2013). Additionally, the larger initial models used enhanced winds

to speed up the process, which is why they didn't undergo core collapse. These processes do not impact our results since the physics of interest is in the accreted envelope and nearly independent of the degenerate interior. This process was also used and discussed in Denissenkov et al. (2013).

After the initial WD models were created, they were cooled to a central temperature of $T_c = 3 \times 10^7$ K, hot enough so that the initial flash is not too violent. The results of Yaron et al. (2005) show that for accretion rates in the stable regime, the accumulated Helium layer is at $T \approx 10^8$ K, making the results of hydrogen-rich accretion nearly independent of $T_c < 10^8$ K, a result we also justify in §2.3. We assume that all WDs are not rotating and that convective overshoot does not occur. To model the nuclear burning, we used `MESA`'s `cno_extras_o18_to_mg26_plus_fe56` network, which accounts for hot CNO burning as well as other heavier isotopes' presence. Radiative opacities are from the OPAL tables (Iglesias & Rogers, 1993, 1996). The spatial and temporal resolutions were adjusted to finer and finer levels until no more substantive changes were observed in the stability/instability boundary or in the reported observables (recurrence times, burning layer temperatures, envelope masses, etc.). This typically resulted in models with between 7000 and 10000 mass zones that are dynamically sized in space and time so that a burning region in an active nova or steady burner is well-resolved, typically occupying around half of the mass zones.

The accreted material has solar composition, with $X = 0.70$, $Y = 0.28$, and metal fractions taken from Lodders (2003), though the OPAL opacities assume a different set of

metal fractions for solar composition. Initializing the accretion often required irradiating the atmosphere before starting accretion so as to ease the thermal readjustment of the outer layers. Any unphysical effects this would have on the model are undone after the ensuing flash(es) that erase the initial conditions (Paczynski & Zytkow, 1978; Sion et al., 1979; Cassisi et al., 1998). The first flash heats the outer layers so that the irradiation is no longer needed for computational convenience. After several flashes (in unstable models) or hydrogen sweeping times, $\Delta M_{\rm H}/(X\dot{M})$, where $\Delta M_{\rm H}$ is the total hydrogen mass (for stably burning models), any hydrogen present in the envelope during the initial accumulation phase has already been burned to helium or ejected. It is after this initial "memory erasing", with irradiation deactivated that we begin our exploration.

For this study, we employ two mass loss prescriptions: super Eddington winds and Roche lobe overflow. For the purposes of our calculation, the RNe systems are assumed to be wide binaries. This is not the case for all RNe. With this assumption, the only active mass loss prescription is the super Eddington wind scheme described in Denissenkov et al. (2013). In this prescription, winds are only active if the photosphereic luminosity of the star exceeds an effective Eddington luminosity which is a mass-average of the local Eddington luminosity from the outer-most cell down to where the optical depth first exceeds 100. The excess luminosity over this effective Eddington luminosity comes in the form of mass ejection moving at the surface escape velocity. Both of these mass ejection scenarios take place over an extended period of time until $L < L_{\rm Edd}$ or $R < R_{\rm RL}$, usually indicating the end of the nova's excursion to the red in the HR diagram. The

tighter binaries in which CNe are found can result in either of these ejection scenarios, so we present results with both assumptions in §2.6, where we also describe the Roche lobe wind prescription in more detail. The inlists for these simulations are available on `http://www.mesastar.org`.

We explore a wide range of WD masses for accretion rates in and near the stable burning regime, so we prepared C-O WDs of masses 0.51 $M_\odot$, 0.60 $M_\odot$, 0.70 $M_\odot$, 0.80 $M_\odot$, 1.00 $M_\odot$, and O-Ne WDs of masses 1.10 $M_\odot$, 1.20 $M_\odot$, 1.30 $M_\odot$, and 1.34 $M_\odot$. Then, using earlier studies of stability regimes (Sienkiewicz, 1980; Nomoto et al., 2007; Shen & Bildsten, 2007), we chose accretion rates within and near the stable burning regime. For each WD we then relaxed the accretion rate to the desired rate and allowed the model to evolve for at least 30 envelope turnover times to erase all history, typically accreting $< 10^{-3}$ $M_\odot$. While the study of much longer-term accretion is certainly warranted (Cassisi et al., 1998; Piersanti et al., 1999), we wanted to initially avoid introducing significant temporal changes to the models resulting from their increasing mass due to secular accumulation of helium. At the end of this accretion period, we take the measurements shown in Figures 2.1 and 2.2.

2.3 Steadily Burning Models

The conditions for stable burning of hydrogen-rich material are detailed in Shen & Bildsten (2007) for a simple one-zone model of burning. The qualitative results are that steady-state burning becomes stable when an increase in temperature causes the cooling

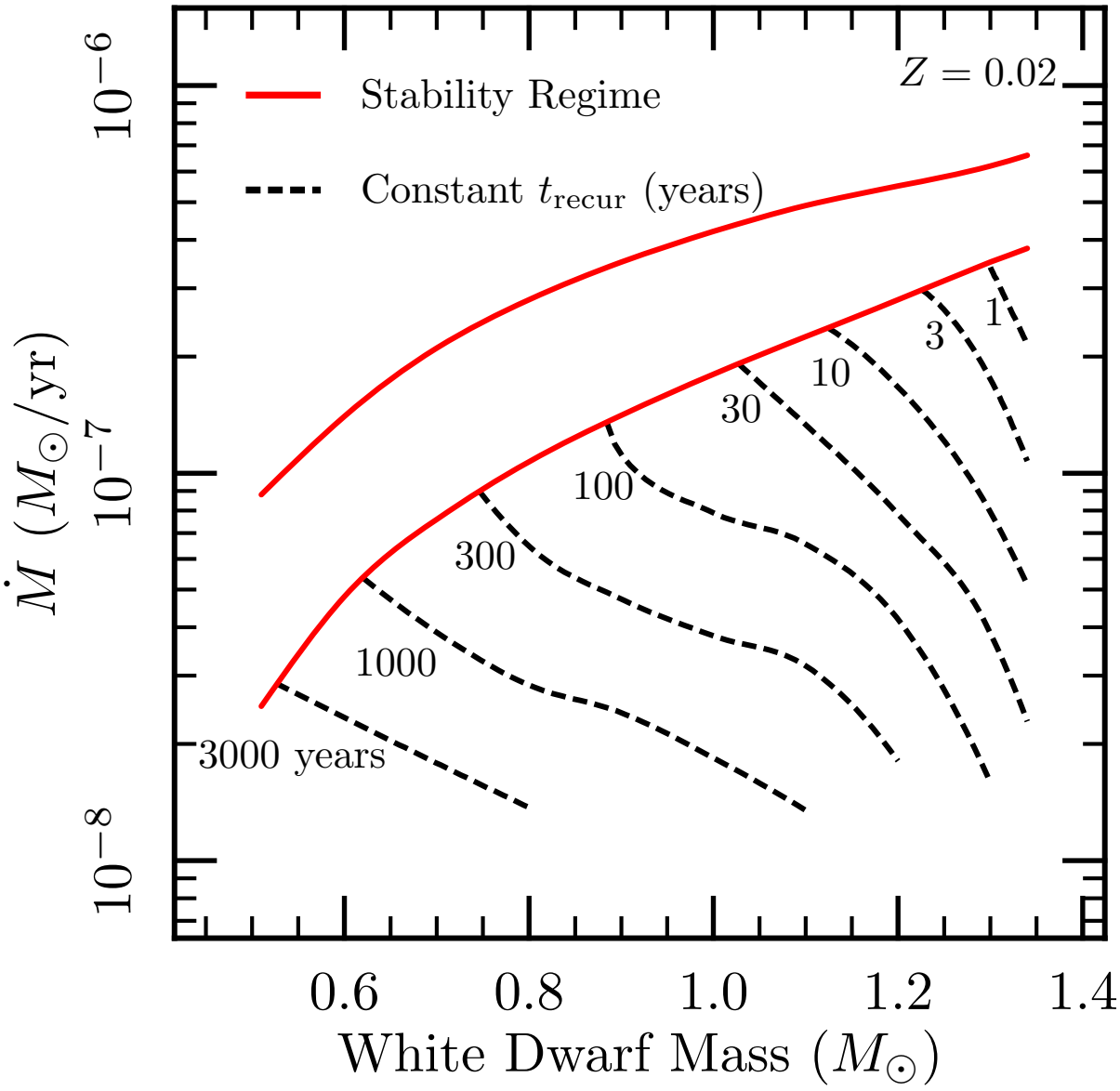

Figure 2.1 Location of the stable-burning regime on the $M - \dot{M}$ plane. The lower red line represents $\dot{M}_{\rm stable}$, the lowest possible accretion rate which exhibits stable and steady burning for a given WD mass. The upper red line gives the highest such accretion rate, $\dot{M}_{\rm RG}$. WDs accreting at rates above $\dot{M}_{\rm RG}$ will still burn stably, but not at the rate that the matter is being accreted, causing the matter to pile up, forming a red giant-like structure. Also shown in dashed black lines are lines of constant recurrence time (in years) for recurrent novae as interpolated from our grid.

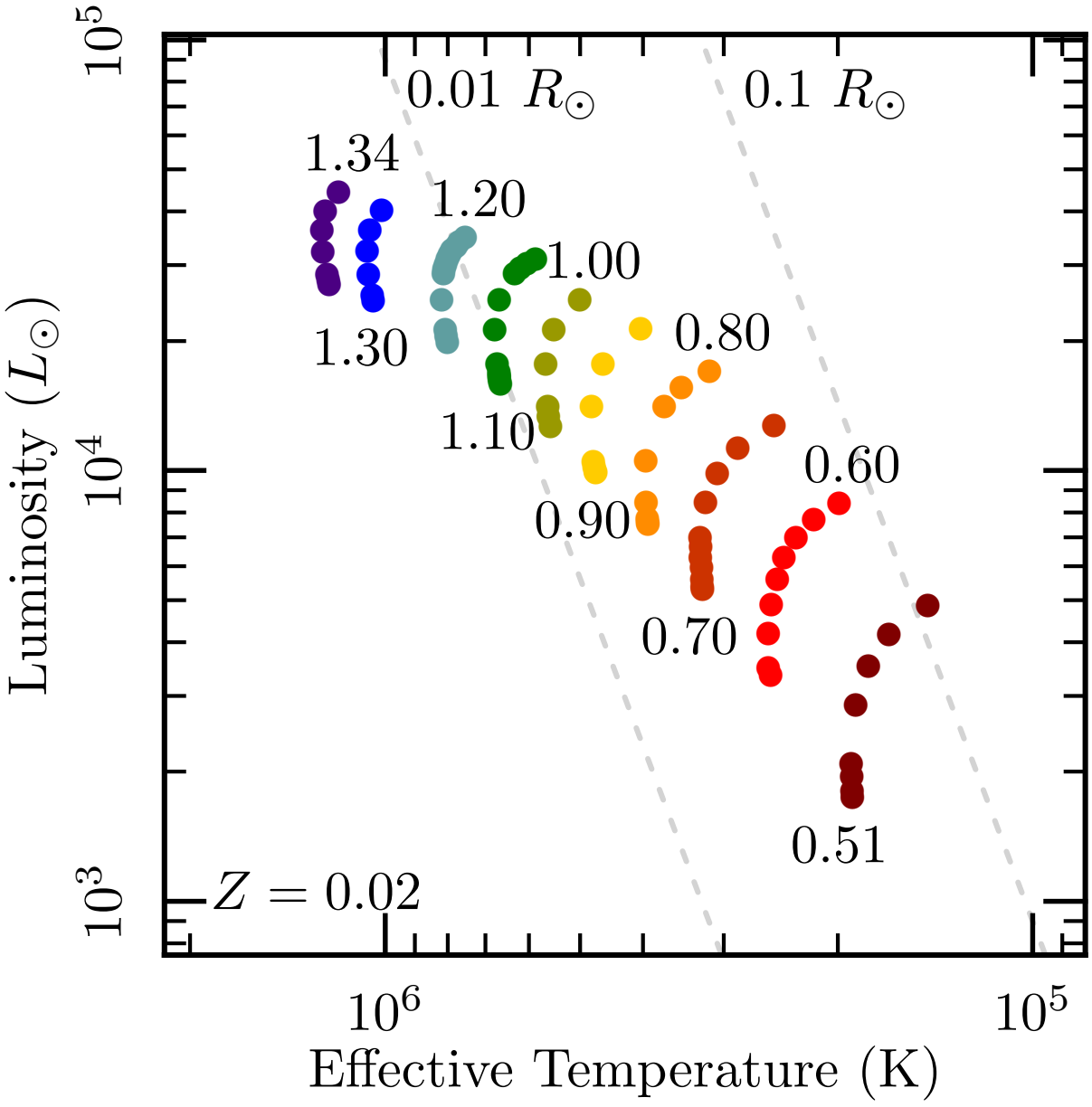

Figure 2.2 Positions of stable burning models of accreting WDs on the HR diagram. The different colors indicate the different WD masses used in the simulations. Lines of constant radii are drawn for $R = 0.01\ R_\odot$ and $0.1\ R_\odot$. The most luminous point for each mass corresponds to the WD accreting at $\dot{M} = \dot{M}_{\rm stable} + 0.8(\dot{M}_{\rm RG} - \dot{M}_{\rm stable})$. At accretion rates close to $\dot{M}_{\rm RG}$, the radius becomes ill-defined as the envelope slowly expands, so we only report those WDs with well-established radii.

rate to increase more than the energy generation rate. At accretion rates below a certain critical value, $\dot{M}_{\rm stable}$, a temperature perturbation would cause the nuclear heating rate to grow faster than the cooling rate causing a thermonuclear runaway that burns the fuel at a rate faster than accretion, triggering a limit-cycle of accumulation and explosion (i.e. novae). Time-dependent calculations naturally reveal the lower stability bound, as unstable periods of hydrogen burning manifest themselves. Table 2.1 summarizes these results, indicating the lower limiting accretion rate for stable burning, $\dot{M}_{\rm stable}$, the total mass of hydrogen, $\Delta M_{\rm H}$, the hydrogen sweeping time, $t_{\rm sweep} = \Delta M_{\rm H}/(X\dot{M}_{\rm stable})$, and the luminosity. Additionally Table 2.2 shows the pressure, density, temperature, fraction of pressure due to gas pressure, and hydrogen mass fraction at the point where the exiting luminosity is half of the total luminosity. Finally, we show the thickness of the shell from the half-luminosity point to the surface of the WD as a fraction of the total radius, R, demonstrating that these burning shells are only marginally thin, enhancing their stability. For the range of masses shown in Figure 2.1, the lower red line represents the values of $\dot{M}_{\rm stable}$. WDs in the region below the lower red line in Figure 2.1 would be recurrent novae.

The upper edge of the stable regime is more subtle. Fujimoto (1982a) and Iben (1982) note that for any WD, there is a maximum envelope mass that can sustain steady-state burning. This corresponds with a plateau in luminosity that is related to the core mass-luminosity relation first found by Paczynski (1970) in AGB cores. In transitioning to a more AGB-like envelope, the luminosity is limited to a maximum value governed by the

core mass, and so increasing $\dot{M}$ just causes more matter to pile on to the envelope while steady-state burning at the plateau luminosity continues at the base of the envelope. From this plateau luminosity, we then identify a hydrostatic upper limit to the accretion rate, $\dot{M}_{\rm RG} = L_{\rm plateau}/XQ_{\rm CNO}$. Shen & Bildsten (2007) explicitly showed that this leads to an upper bound on the stable regime that is tightly constrained to $\dot{M}_{\rm RG} \approx 3\dot{M}_{\rm stable}$. It is always the case that $\dot{M}_{\rm RG}$ is a stronger upper limit on the accretion rate than that set by the Eddington luminosity, $\dot{M}_{\rm Edd} = L_{\rm Edd}/XQ_{\rm CNO}$, but in our code it often manifested itself by triggering super Eddington winds since the increase in radius caused the opacity in the outer layers to diverge from pure electron scattering.

For a given mass, increasing $\dot{M}$ to $\dot{M}_{\rm RG}$ causes the WD to travel along a path in the HR diagram to higher L and $T_{\rm eff}$ until it hits a "knee", at which point the luminosity continues to grow, but the effective temperature decreases, indicating a radial expansion of the envelope. This knee can be seen in Figure 2.2. The regime inhabited by these stably and steadily burning WDs in the HR diagram is also known to hold many of the supersoft sources (Nomoto et al., 2007), making these stable burners excellent candidates as the source of the soft X-rays. At high enough $\dot{M}$'s, hydrogen burning is outpaced by accretion, causing a radial expansion in the envelope and a build-up of hydrogen (Nomoto et al., 1979). The upper line in Figure 2.1 represents models with the highest $\dot{M}$ that exhibit steady-state burning of hydrogen at the accreted rate, $\dot{M}_{\rm RG}$. WDs in the region above the upper line in Figure 2.1 will still burn hydrogen at a constant rate (albeit more slowly than it is being accreted), and their envelopes will grow until optically-thick

Table 2.1. Stably Burning WDs at the Stability Boundary: Global Properties

$M_{\rm WD}$ ($M_\odot$)	$\dot{M}_{\rm stable}$ ($10^{-7} M_\odot\,{\rm yr}^{-1}$)	$\Delta M_{\rm H}$ ($M_\odot$)	$t_{\rm sweep}$ (yr)	L ($10^3\,L_\odot$)
0.51	0.25	4.9×10^{-5}	2810	1.74
0.60	0.48	2.4×10^{-5}	720	3.36
0.70	0.76	1.2×10^{-5}	226	5.32
0.80	1.07	6.7×10^{-6}	88.7	7.51
0.90	1.41	3.5×10^{-6}	35.4	9.89
1.00	1.80	2.0×10^{-6}	15.5	12.7
1.10	2.40	9.6×10^{-7}	6.08	15.9
1.20	2.80	4.4×10^{-7}	2.24	19.8
1.30	3.50	1.3×10^{-7}	0.534	24.9
1.34	3.80	6.0×10^{-8}	0.226	27.0

winds or Roche-lobe overflow can slow the accretion rate (Hachisu et al., 1996). We don't investigate these systems in our study except to find the value of $\dot{M}_{\rm RG}$ for each mass.

The internal structures of 0.60 $M_\odot$, 1.00 $M_\odot$, and 1.34 $M_\odot$ WDs accreting at $\dot{M} = 5.0 \times 10^{-8}\ M_\odot\,{\rm yr}^{-1}$, $2.0 \times 10^{-7}\ M_\odot\,{\rm yr}^{-1}$, and $4.0 \times 10^{-7}\ M_\odot\,{\rm yr}^{-1}$, respectively, are shown in Figure 2.3.

The cores are largely isothermal and degenerate, but on top of them is a hot helium layer that is the ash of the stable burning. Above the ash is the radiative hydrogen envelope with most of the burning occurring just above the Helium ash. To further illustrate the presence of a thick, hot helium layer, Figure 2.4 shows the elemental abundance and temperature profile of the same 1.00 $M_\odot$ WD shown in Figure 2.3. Additionally, we see the expected pattern of a hydrogen-helium transition zone above the hot ash, coinciding with a rising ^{14}N mass fraction due to CNO burning.

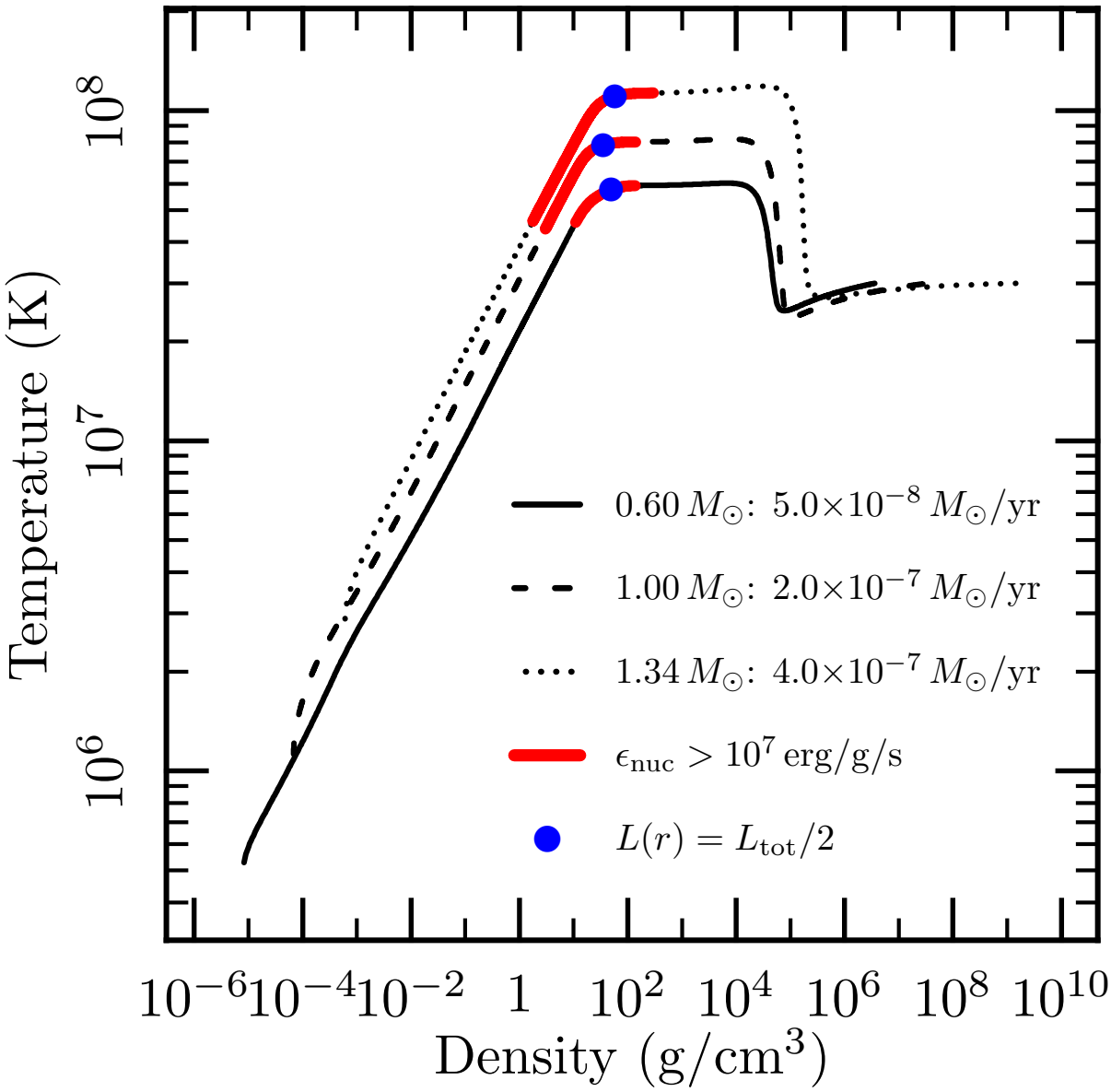

Figure 2.3 The temperature-density profile of 0.60 $M_\odot$, 1.00 $M_\odot$, and 1.34 $M_\odot$ WDs accreting at $\dot{M} = 5.0 \times 10^{-8}\ M_\odot\,\mathrm{yr}^{-1}$, $\dot{M} = 2.0 \times 10^{-7}\ M_\odot\,\mathrm{yr}^{-1}$, and $\dot{M} = 4.0 \times 10^{-7}\ M_\odot\,\mathrm{yr}^{-1}$, respectively. Areas of significant hydrogen burning are marked, as well as the point where the exiting luminosity is half of the total luminosity of the star.

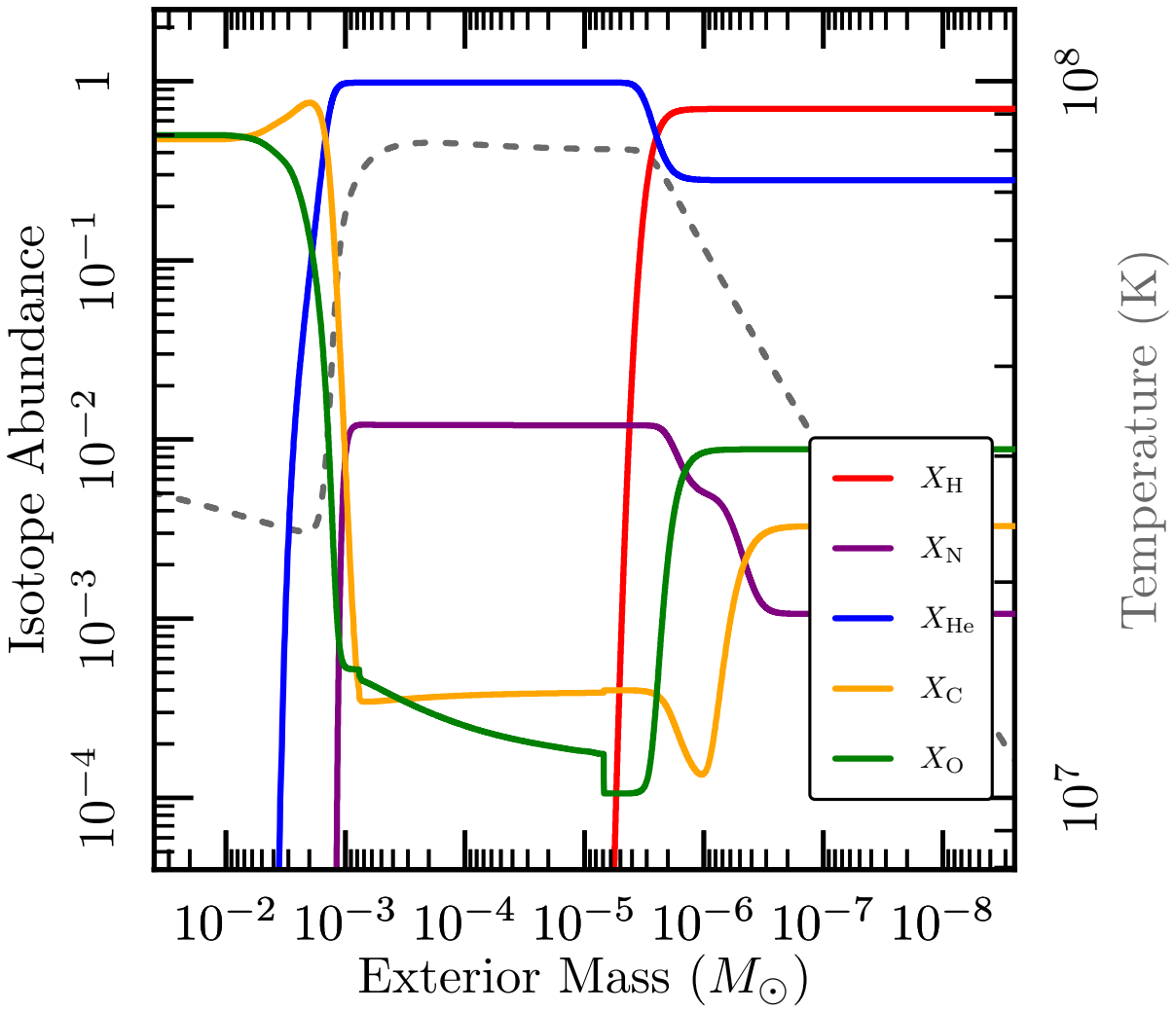

Figure 2.4 The abundance profile of a 1.00 $M_\odot$ WD accreting at $\dot{M} = 2.0 \times 10^{-7}\ M_\odot\,\mathrm{yr}^{-1}$. The temperature profile (dashed line) has also been included to show that the hottest region is the layer of helium ash that dominates the burning conditions rather than the cooler core.

Table 2.2. Stably Burning WDs at the Stability Boundary: Properties at $L(r) = L_{\rm phot}/2$

$M_{\rm WD}$ ($M_\odot$)	P (10^{17} dyne/cm^2)	ρ (g/cm^3)	T (10^7 K)	β -	$X_{\rm H}$ -	$\Delta R/R$ -
0.51	2.31	47.5	5.08	0.928	0.258	0.558
0.60	2.25	36.0	5.69	0.882	0.335	0.496
0.70	2.48	36.7	6.24	0.846	0.286	0.430
0.80	2.74	35.9	6.72	0.812	0.290	0.376
0.90	3.15	37.0	7.22	0.783	0.291	0.323
1.00	3.63	38.9	7.72	0.753	0.280	0.285
1.10	4.37	42.1	8.32	0.723	0.272	0.244
1.20	5.41	44.8	9.05	0.687	0.284	0.210
1.30	7.66	52.4	10.2	0.644	0.293	0.168
1.34	9.76	61.0	10.9	0.630	0.290	0.141

From Figures 2.3 and 2.4 as well as Table 2.2, we see that there is a temperature $T_{\rm stable}$ at which the stable burning occurs, and that $T_{\rm stable}$ is an increasing function of both $\dot{M}$ and $M_{\rm WD}$. We can explain this dependence with a few assumptions about the nature of the hydrogen-rich envelope. We expect the burning to occur at a depth where the burning timescale, $t_{\rm burn} \sim Q_{\rm CNO}/\epsilon_{\rm CNO}$ (where $\epsilon_{\rm CNO}$ is the nuclear energy generation rate per unit mass and $Q_{\rm CNO}$ is the amount of energy released per unit mass of hydrogen undergoing complete CNO burning) is approximately equal to the accretion timescale, $t_{\rm acc} = \Delta M/\dot{M}$. If we assume a thin shell, where the pressure is approximately $P = GM_{\rm WD}\Delta M/(4\pi R_{\rm core}^4)$, (where $R_{\rm core}$ is the radius at the base of the hydrogen-rich envelope) we get the burning condition to be $\epsilon_{\rm CNO} = (Q_{\rm CNO}G\dot{M}M_{\rm WD})/(PR_{\rm core}^4)$. Furthermore, the opacity in the hydrogen-rich layer is dominated by electron scattering and the envelope is radiative, so the accretion rate can be related to temperature and

pressure via $XQ_{\rm CNO}\dot{M} = L \propto M_{\rm WD}T^4/P$. For our uses, we want to eliminate pressure, so we use $P \propto M_{\rm WD}T^4/\dot{M}$. Finally, we expand $\epsilon_{\rm CNO}$ as a power law in temperature, and with the assumption pressure is due primarily to gas pressure, we may use $\epsilon_{\rm CNO} \propto \rho T^\nu = (P/T)T^\nu = M_{\rm WD}T^{\nu+3}/\dot{M}$. Putting this all together we find

$$T_{\rm stable} \propto \dot{M}^{3/(\nu+7)} M_{\rm WD}^{-1/(\nu+7)} R_{\rm core}^{-4/(\nu+7)}, \tag{2.1}$$

where $\nu = 23.58/T_7^{1/3} - 2/3$ and $T_7 = T/10^7$ K as shown in Hansen et al. (2004). Note that $R_{\rm core}$ is negatively correlated with $M_{\rm WD}$ but positively (though weakly) correlated with $\dot{M}$. As a result, we expect $T_{\rm stable}$ to *increase* with increasing $M_{\rm WD}$ at constant $\dot{M}$ through the implicit $R_{\rm core}$-dependence. For a fixed mass, the radius is approximately constant with changing $\dot{M}$, so $T_{\rm stable}$ is only depending on a small power of $\dot{M}$. Using a prefactor of 3.5×10^8 K (assuming $M_{\rm WD}$ and $R_{\rm core}$ are measured in solar units and $\dot{M}$ in $M_\odot\,{\rm yr}^{-1}$), Equation (2.1) and the $\nu - T_7$ relation yield temperatures at the point of peak burning accurately to within 20%. For intermediate masses ($0.6\,M_\odot \leq M_{\rm WD} \leq 1.2\,M_\odot$), the calculated temperatures are typically well within 10% of the simulated values.

2.4 Unstable Burning

At accretion rates below the stable burning boundary ($\dot{M} < \dot{M}_{\rm stable}$) indicated in Table 2.1, the WDs undergo periodic hydrogen flashes. For accretion rates near the stable boundary, these flashes lead to little mass loss from the system. Higher mass WDs experience shorter recurrence times for a given $\dot{M}$. Equivalently, the ignition mass (the mass of accreted material at which a runaway occurs) is smaller for larger core masses

where the higher surface gravity allows for higher pressures with less mass accumulation. If we look at the "first unstable model" (the model with $\dot{M} \lesssim \dot{M}_{\rm stable}$), we can identify the minimum recurrence time (or equivalent ignition mass) for that core mass. Before exploring these boundary cases, we should justify our assumption that such a limiting configuration exists

Paczynski (1983) examined flashes on hydrogen-accreting compact objects with a simple one-zone model using linear stability analysis. His analysis showed that as the accretion rate is decreased, the steady state models go from stable (perturbations die exponentially) through quasi-stable (perturbations act as damped oscillators), quasi-unstable (perturbations oscillate with increasing amplitude), and finally fully unstable phases. When simulating the unstable-to-stable flash transition, though, he found that the transformation was very rapid. The one-zone models gave large amplitude flashes (i.e. novae) until the accretion rate reached the stable accretion rate at which point the model switched over to stable and steady burning with very little weakening of the flashes. In other words, there is essentially a discontinuity in the stability of the burning very near $\dot{M}_{\rm stable}$.

In Figure 2.5 we plot a high resolution grid of $\dot{M}$'s performed on the 1.00 $M_\odot$ model, demonstrating that as $\dot{M}$ approaches $\dot{M}_{\rm stable}$, the igntion mass and recurrence times indeed approach nearly constant values of $\Delta M_{\rm H} \approx 4.4 \times 10^{-6}\ M_\odot$ and $t_{\rm recur} \approx 40$ years. While we didn't compute this fine of a grid for each mass tested, we obtained the stable/unstable boundary resolved to within five percent of $\dot{M}_{\rm stable}$. This is precise enough

for identifying limiting recurrence times and hydrogen ignition masses.

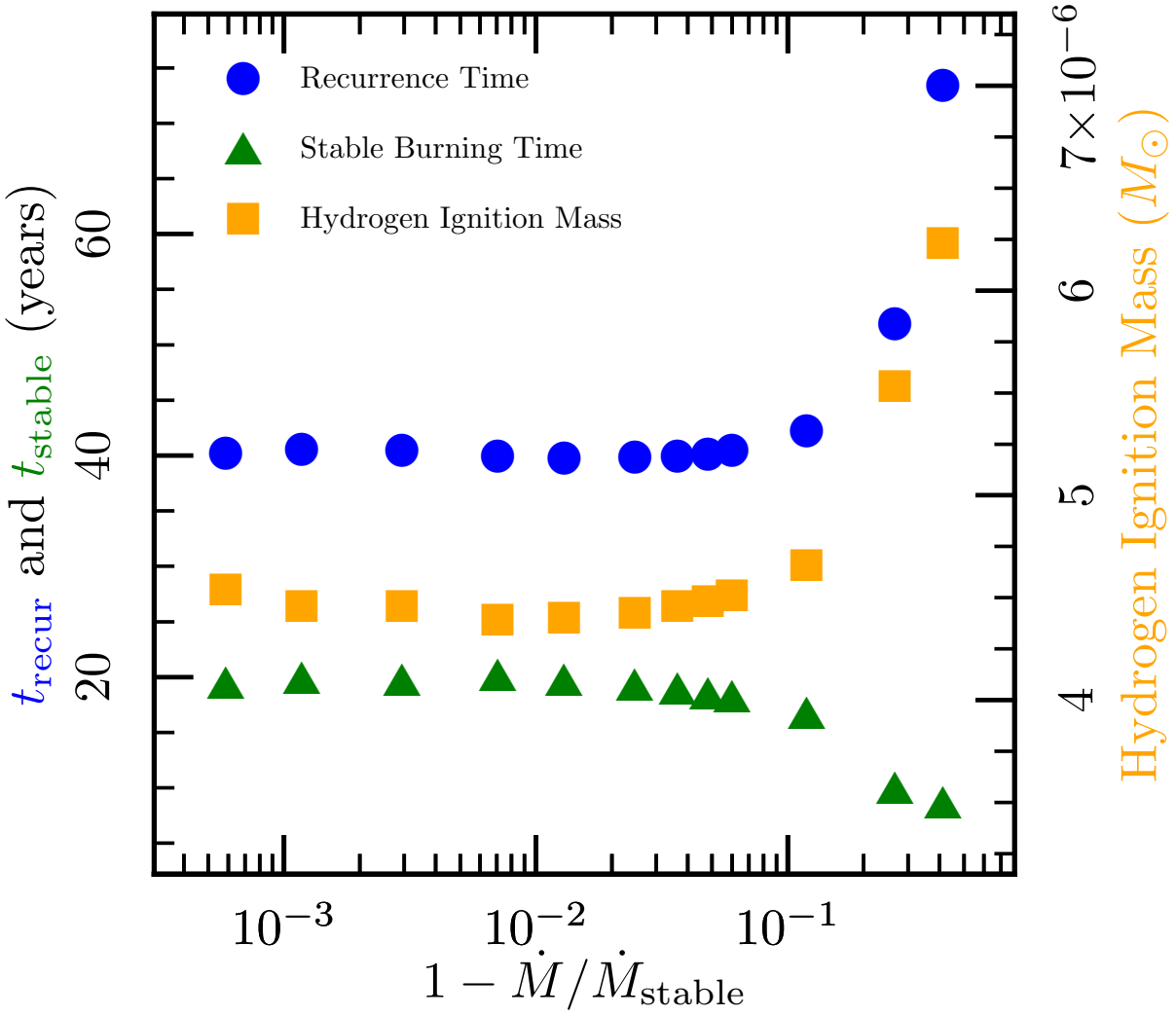

Figure 2.5 Convergence of the recurrence time, hydrogen ignition mass, and stable burning duration as $\dot{M}$ approaches $\dot{M}_{\rm stable}$ for $M_{\rm WD} = 1.00\ M_\odot$.

An observer can then use an observed nova recurrence time to infer a minimum core mass. Table 2.3 lists the recurrence times for each first unstable model. There we also list the peak temperature in the helium layer in the low-luminosity state as well as the peak temperature in the burning layer as the convective burning zone develops. The temperature in the helium layer during the low-luminosity state is always close to

the extrapolated stable burning temperature (the temperature that would be expected by the empirical power law fit at that $\dot{M}$), though the two temperatures do not track monotonically due to the varying helium mass from model to model.

Townsley & Bildsten (2004) examined how classical novae (CNe) ignition masses depend on $\dot{M}$. Their analysis assumed that the core had reached an equilibrium temperature due to prolonged thermal contact with the cycling outer layers. We see that for sufficiently high $\dot{M}$'s, the helium layer retains a significant fraction of the thermal energy generated in a nova event. So, for these $\dot{M}$'s, the ignition mass and thus nearly all other characteristics of a nova are independent of T_c. This trend is also seen in the models with highest $\dot{M}$'s in Yaron et al. (2005). The hot helium layer in the unstable models is evident in Figures 2.6 and 2.7 even while in the quiescent state. For CNe, CNO enrichment is seen in ejecta, indicating that any helium layer from previous outbursts is mixed with the hydrogen during the TNR and ejected along with a portion of the WD core. Thus, we only expect the helium layer to be relevant at $\dot{M}$'s near $\dot{M}_{\rm stable}$ where mixing may cause helium dredge-up, but not necessarily the removal of the entire layer. This would allow for the gradual build-up of an insulating helium layer.

As $\dot{M}$ decreases, more time is allowed for the helium layer to cool. This, in turn, causes the ignition mass to increase, since a higher pressure is required to start a thermonuclear runaway at a lower temperature. The trends for ignition masses in high-mass WDs are shown in Figure 2.8. Compared to their steadily burning counterparts, the first unstable model (the left-most point for each mass in Figure 2.8) has a hydrogen ignition mass that

Table 2.3. Properties of Recurrent Novae Just Below the Stability Boundary

$M_{\rm WD}$ ($M_\odot$)	$\dot{M}$ ($10^{-7} M_\odot\,{\rm yr}^{-1}$)	$t_{\rm recur}$ (yr)	$t_{\rm sweep}$[a] (yr)	$T_{\rm He}$[b] (10^7 K)	$T_{\rm peak}$[c] (10^7 K)
0.51	0.24	4200	2810	5.0	8.3
0.60	0.46	1300	720	5.8	8.8
0.70	0.70	480	226	6.4	9.3
0.80	1.00	200	88.7	7.2	10.0
0.90	1.25	90	35.4	7.0	10.7
1.00	1.7	40	15.6	8.0	11.1
1.10	2.34	13.4	6.08	8.0	12.0
1.20	2.7	4.3	2.24	9.9	13.1
1.30	3.4	1.00	0.534	9.1	14.3
1.34	3.7	0.39	0.226	10.0	15.1

[a]Time for the stable model of the same $M_{\rm WD}$ to burn through one full layer of hydrogen.

[b]Peak temperature during the low-luminosity state in the helium layer.

[c]Peak temperature during the outburst event.

is two to three times larger than the stable hydrogen mass. Thus, the static hydrogen masses from the steadily burning masses cannot be extrapolated into the RNe regime to obtain recurrence times.

2.5 Comparisons to Other Studies

Sienkiewicz (1980), Shen & Bildsten (2007), and Nomoto et al. (2007) all used linear stability analysis to test the stability of constructed steady-state burning models. This is a time-independent method that serves as a complementary check to our time-dependent

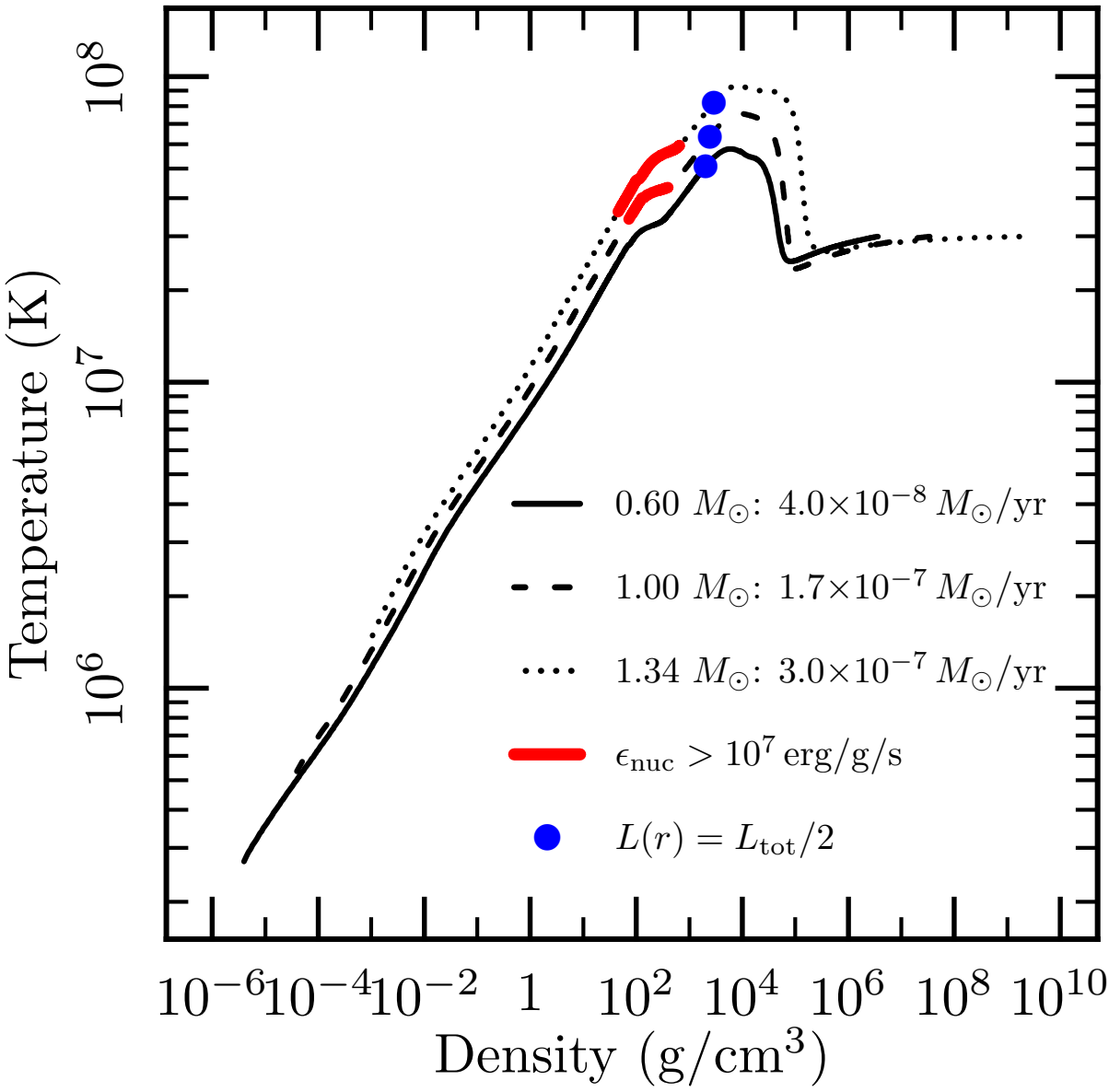

Figure 2.6 The temperature-density profile of 0.60 $M_\odot$, 1.00 $M_\odot$, and 1.34 $M_\odot$ WDs accreting at $\dot{M} = 3.0 \times 10^{-8}\ M_\odot\,\mathrm{yr}^{-1}$, $\dot{M} = 1.7 \times 10^{-7}\ M_\odot\,\mathrm{yr}^{-1}$, and $\dot{M} = 3.0 \times 10^{-7}\ \mathrm{yr}^{-1}$, respectively. Areas of significant CNO burning are marked, as well as the point where the exiting luminosity is half of the total luminosity of the star. These profiles correspond to the quiescent (pre-nova) state of a recurrent nova cycle. The hot helium layer is still present.

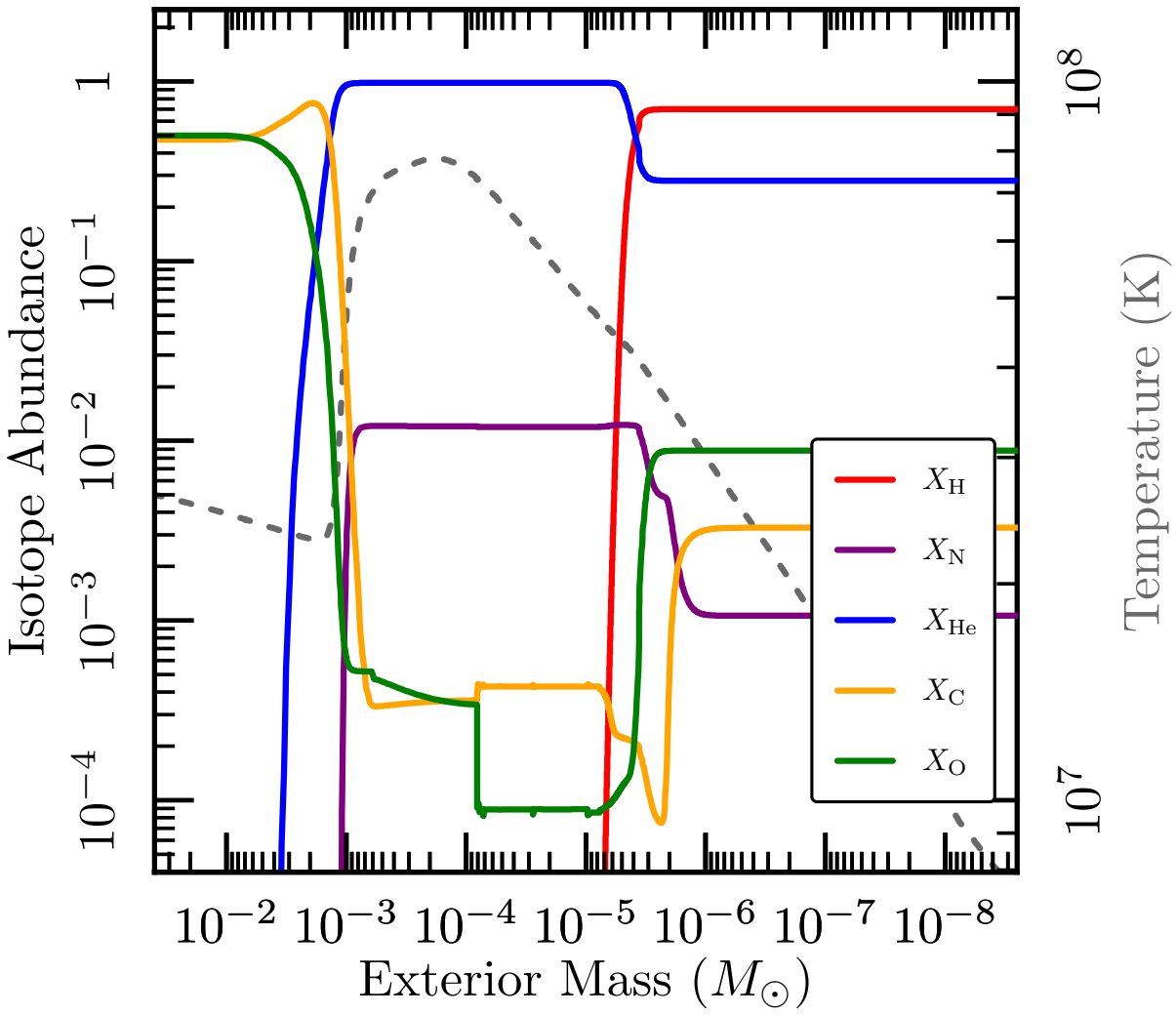

Figure 2.7 The abundance profile of a 1.00 $M_\odot$ WD accreting at $\dot{M} = 1.7 \times 10^{-7}\ M_\odot\,\mathrm{yr}^{-1}$. The temperature profile has also been included to show that the hottest region is the layer of helium ash that dominates the burning conditions rather than the cooler core. Again, this profile is from the quiescent (pre-nova) state.

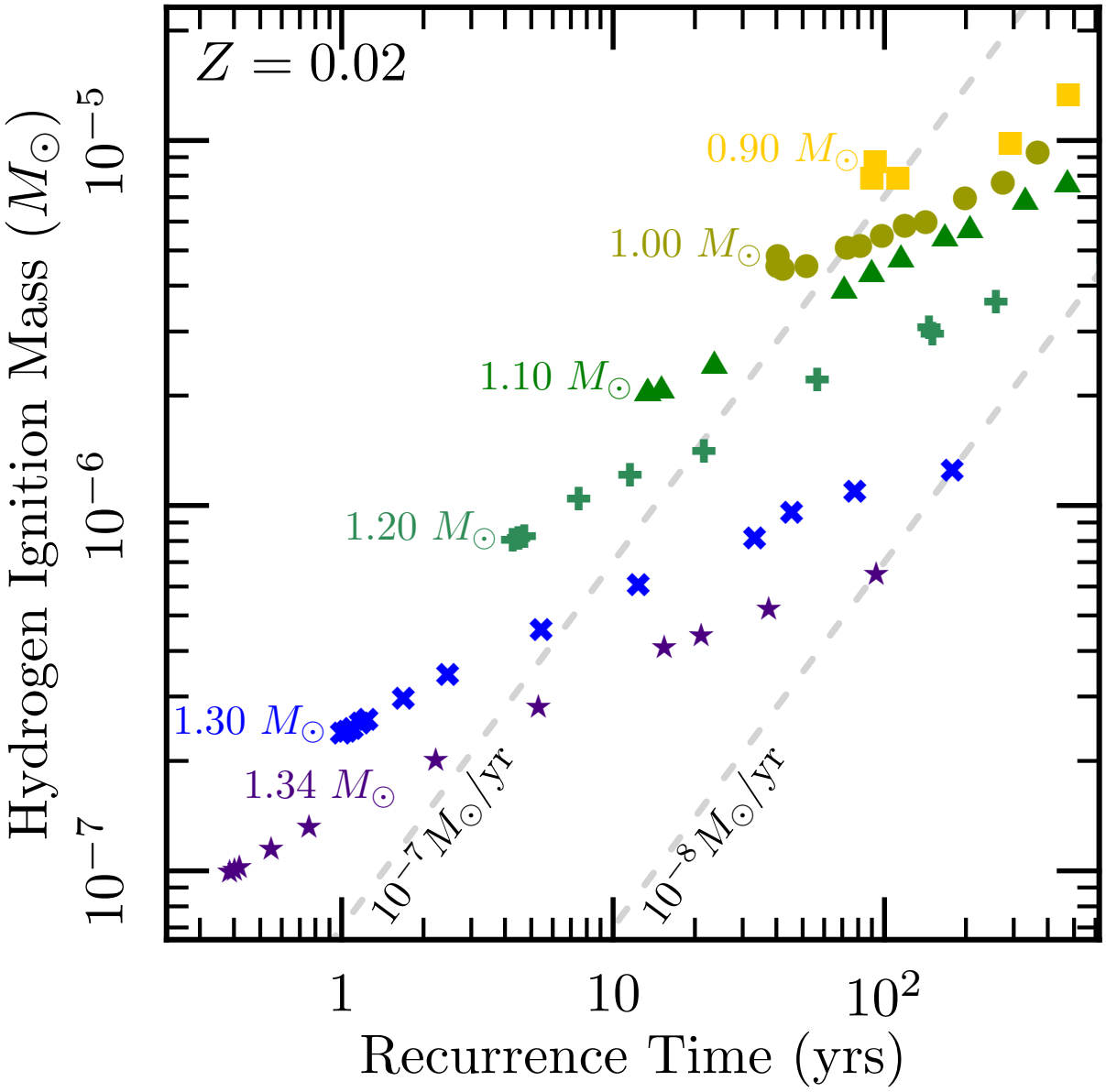

Figure 2.8 Ignition masses for high-mass WDs as a function of recurrence time. Lines of constant accretion rate (dashed) are also shown. The ignition masses reported here are the total amount of hydrogen accreted between outbursts, $X\dot{M}t_{\rm recur}$, and thus necessarily lower than the total hydrogen mass present at the time of the nova eruption. We find that over the range of $M_{\rm WD}$ and $\dot{M}$ presented here, $\Delta M_{\rm H,tot}/\Delta M_{\rm H,acc} \approx 1.2$.

calculations. We find that our stability region shown in Figure 2.1 is largely consistent with these results and plot our results along with those of Nomoto et al. (2007) and Shen & Bildsten (2007). Each of these is plotted in Figure 2.9, demonstrating the agreement between various techniques.

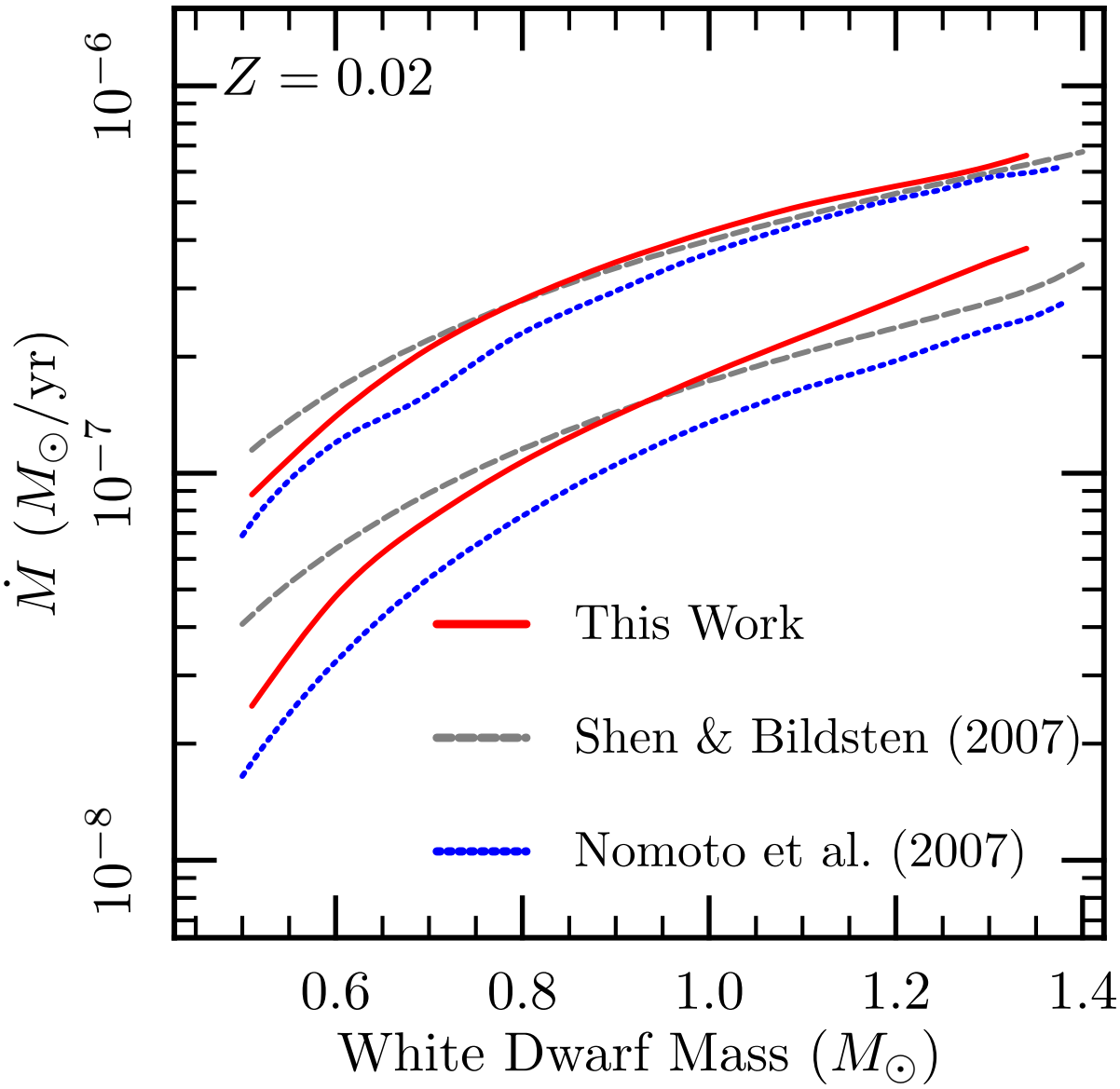

Figure 2.9 Stability regimes of this work (red solid line), Nomoto et al. (2007) (dotted blue line), and Shen & Bildsten (2007) (dashed gray line).

Shen & Bildsten (2007) studied a one-zone model for stability at various accretion rates and compared their results favorably to those of Nomoto et al. (2007), noting that the discrepancy at lower masses was likely due to their assumption of the burning layer being the mass within a scale height. Nomoto et al. (2007) compute the entire stellar model, but assumed a discontinuous transition from solar composition to nearly pure helium (Nomoto 2012, private communication). We, however, observe a transition zone where most of the burning is occurring, so accurate comparisons are not possible. Nonetheless, Figure 2.9 demonstrates agreement in the stability boundary between the linear stability analysis and time-dependent calculations.

Other recent time-dependent studies of accreting WDs in and near the stable-burning regime have been carried out by Iben (1982), Livio et al. (1989), Cassisi et al. (1998), and Yaron et al. (2005). The thorough analysis in Iben (1982) shows that recurrence times change over the course of several flashes. Hence, we only compare to simulations that computed through multiple flashes to mitigate the effect of initial condition choices. We now compare our simulations wherever possible.

Iben (1982) studied a 1 $M_\odot$ WD accreting in a quasi-static (hydrostatic) approximation for $\dot{M}$'s near and in the stable-burning regime. He assumed $X = 0.64$ in the accreted material and also neglected mass loss. Both of these assumptions should lead to longer recurrence times. The lowered hydrogen composition lowers the CNO energy generation rate, requiring a higher pressure/temperature to get to the same level of burning as would be expected if $X = 0.70$. The lack of mass loss greatly affects the time the WD spends at

high luminosities, since it must burn through most of the accreted envelope rather than removing most of it through winds. At high $\dot{M}$'s, the time spent on the high-luminosity branch is comparable to the time spent in quiescence, so ignoring mass loss will lead to appreciably longer recurence times. Additionally, the cores for Iben (1982) were typically much hotter than ours, exceeding the temperature of the quiescent helium layer from our models. We expect this would act to decrease the recurrence time since lower pressures (and thus accreted masses) are required at higher temperatures to trigger a TNR. Finally, Iben (1982) must certainly have used different opacities, which would affect the structure of the accreted envelope.

At first, data for a stripped AGB core with $T_c \approx 3 \times 10^8\,\mathrm{K}$ is presented. For $\dot{M} = 2.5 \times 10^{-7}\,M_\odot\,\mathrm{yr}^{-1}$, he reports steady and stable burning, which we also observe. At $\dot{M} = 1.5 \times 10^{-7}\,M_\odot\,\mathrm{yr}^{-1}$, he observes recurrence times at around 72 years, though they are evidently still increasing in his Figure 6. In contrast, our corresponding model had a recurrence time of 42 years. His model has approximately 36 years of intense hydrogen burning, whereas ours burns for only 17, indicating that mass loss is responsible for the much of the discrepancy. He also displays data for the same hot WD as well as one whose core has gone into a "steady-state" temperature configuration ($T_c \approx 7 \times 10^7$ K) accreting at $\dot{M} = 1.5 \times 10^{-8}\,M_\odot\,\mathrm{yr}^{-1}$. These exhibit recurrence times of $\approx 550 - 650$ years, though it is apparent in his Figures 7 and 11 that the recurrence times have not grown to their asymptotic values yet. We observe longer recurrence times at ≈ 1400 years. In this case, the neglect of mass loss is likely unimportant since the accretion phase is much longer

than the outburst phase, but the higher central temperatures of both WDs are pushing the recurrence times down relative to ours.

Livio et al. (1989) simulated a 1.0 $M_\odot$ WD with $T_c = 10^8$ K accreting at 10^{-8}, 10^{-7}, and 10^{-6} $M_\odot\,\mathrm{yr}^{-1}$. Again, this core temperature is even hotter than the stable burning temperature of the steady burners, so it will influence ignition masses. Thus, we would expect their results to exhibit shorter recurrence times and a lower stability boundary. Additionally, the accreted material in their simulations had $X = 0.7$ and $Z = 0.03$. Their M8 model, at $\dot{M} = 10^{-8}$ $M_\odot\,\mathrm{yr}^{-1}$ exhibited repeated hydrogen flashes with $t_{\mathrm{recur}} = 1520$ years and an ignition mass (total mass present above the helium layer) of $\Delta M_{\mathrm{ign}} = 1.7 \times 10^{-5}$ $M_\odot$. In our corresponding model which had the lower core temperature but the same $\dot{M}$, we find $t_{\mathrm{recur}} = 2220$ years and an ignition mass of $\Delta M_{\mathrm{ign}} = 2.6 \times 10^{-5}$ $M_\odot$, which given the core temperature for such a relatively low $\dot{M}$, is a plausible difference. For their M7 model, which accreted at 10^{-7} $M_\odot\,\mathrm{yr}^{-1}$, they found $t_{\mathrm{recur}} = 135$ years, whereas our corresponding model gives $t_{\mathrm{recur}} = 73$ years. Their M6 model, accreting at 10^{-6} $M_\odot\,\mathrm{yr}^{-1}$ expanded to red giant proportions, as did ours.

Cassisi et al. (1998) studied WDs with $M_{\mathrm{WD}} = 0.516$ $M_\odot$ and $M_{\mathrm{WD}} = 0.80$ $M_\odot$ accreting at rates comparable to the stable burning regime. Their accreting matter has $X = 0.7$ and $Z = 0.02$, and the core temperatures are well below their observed helium layer temperatures, so we expect their models to compare more favorably to ours. It appears that there was no mass loss prescription applied by Cassisi et al. (1998). We don't anticipate this causing any significant differences with our results since the stable

burning lifetimes for the configurations in question are small compared to the accretion timescales. Additionally, the opacities used in Cassisi et al. (1998) are taken from older Los Alamos tables that they claim are very similar to the OPAL opacities. They simulated a 0.516 $M_\odot$ WD accreting at rates of 2×10^{-8}, 4×10^{-8}, 6×10^{-8}, 10^{-7}, and 10^{-6} $M_\odot\,\mathrm{yr}^{-1}$. They observe that the model with $\dot{M} = 2 \times 10^{-8}$ $M_\odot\,\mathrm{yr}^{-1}$ exhibits hydrogen flashes with $t_{\mathrm{recur}} = 5400$ years, whereas our 0.51 $M_\odot$ model at the same $\dot{M}$ has $t_{\mathrm{recur}} = 5040$ years. For $\dot{M} = 4 \times 10^{-8}$, 6×10^{-8}, and 1×10^{-7} $M_\odot\,\mathrm{yr}^{-1}$, they observe steady burning, which is mostly consistent with our results, though we found that for our 0.51 $M_\odot$ WD, an $\dot{M}$ of 10^{-7} $M_\odot\,\mathrm{yr}^{-1}$ resulted in a red giant configuration. Their WD is slightly more massive, and given that we find that $\dot{M} = 9 \times 10^{-8}$ $M_\odot\,\mathrm{yr}^{-1}$ gives stable burning on our 0.51 $M_\odot$ WD, the discrepancy seems plausible. Finally, both Cassisi et al. (1998) and we observe a red giant phase for $\dot{M} = 1 \times 10^{-6}$ $M_\odot\,\mathrm{yr}^{-1}$.

For their 0.80 $M_\odot$ WD, Cassisi et al. (1998) ran simulations with $\dot{M} = 10^{-8}$, 4×10^{-8}, 10^{-7}, 1.6×10^{-7}, and 4×10^{-7} $M_\odot\,\mathrm{yr}^{-1}$. For the lowest three $\dot{M}$'s, they found $t_{\mathrm{recur}} = 3110$ years, 483 years, and 204 years, respectively. For the same mass and $\dot{M}$'s, we find $t_{\mathrm{recur}} = 3370$, 596, and 200 years, respectively. We both observe steady burning at $\dot{M} = 1.6 \times 10^{-7}$ $M_\odot\,\mathrm{yr}^{-1}$, and we both observe a red giant configuration at $\dot{M} = 4 \times 10^{-7}$ $M_\odot\,\mathrm{yr}^{-1}$.

Finally, we compare to Yaron et al. (2005), who simulated accreting WDs with masses of 0.65, 1.00, and 1.25 $M_\odot$ (among others that we do not compare to). For each of these masses, they accreted matter at rates of 10^{-8} and 10^{-7} $M_\odot\,\mathrm{yr}^{-1}$ (again with many more

at lower $\dot{M}$'s that aren't applicable to our study). They also varied the core temperature between 1×10^7 K and 5×10^7 K. It shouldn't affect our results, but we will compare only with the $T_c = 3 \times 10^7$ K results. Finally, they employed an optically thick, supersonic wind as a mass loss prescription (Prialnik & Kovetz, 1995) and allowed for mixing between the core and envelope, as evidenced by their metal-enriched ejecta.

At no point is stable burning reported in Yaron et al. (2005), though it seems that simulations with no mass loss correspond to our red giant or stable configurations (a period is still reported in their Table 3). For $M_{\rm WD} = 0.65\ M_\odot$, $t_{\rm recur} = 10200$ and 254 years are reported for $\dot{M} = 10^{-8}$ and $10^{-7}\ M_\odot\,{\rm yr}^{-1}$, respectively. Using our own 0.65 $M_\odot$ WD, we find a recurrence time of 7800 years for $\dot{M} = 10^{-8}\ M_\odot\,{\rm yr}^{-1}$ and stable burning for $\dot{M} = 10^{-7}\ M_\odot\,{\rm yr}^{-1}$. For the 1.00 $M_\odot$ case, the two reported $t_{\rm recur}$'s are 2030 and 87.4 years, whereas ours are $t_{\rm recur} = 2216$ and 72.6 years. Finally, their 1.25 $M_\odot$ WDs give $t_{\rm recur} = 384$ and 19.6 years. Our 1.25 $M_\odot$ WD models indicate $t_{\rm recur} = 258$ and 14.4 years at these $\dot{M}$'s. For the higher $\dot{M}$'s, there is little to no metal enrichmeent in the ejecta and only minor helium enrichment, so we expect the reasonable agreement in most of the calculations. The exception is the $M = 1.25\,M_\odot$, $\dot{M} = 10^{-8}\,M_\odot\,{\rm yr}^{-1}$ calculation, where the ejecta in Yaron et al. (2005) is significantly metal-enriched, indicating significant mixing with the core. It's not immediately obvious why our calculation with no enrichment has a shorter recurrence time, since CNO burning should start more easily with an enriched base layer.

2.6 Post-Outburst Novae

In addition to the models computed for stability analysis, we also ran models with $M_{\rm WD} = 0.6\,M_\odot$, $1.0\,M_\odot$, $1.1\,M_\odot$, $1.2\,M_\odot$, $1.3\,M_\odot$, and $1.34\,M_\odot$ at a lower accretion rate of $\dot{M} = 10^{-9}\,M_\odot\,{\rm yr}^{-1}$ to study the stable burning phase after a classical nova (CN). For mass loss, we used both the super Eddington wind prescription described earlier as well as Roche lobe overflow (RLOF) by putting the WDs in a binary systems with Roche lobe radii between $R_{\rm RL} = 0.4\,R_\odot$ and $1.0\,R_\odot$. Our choice for the accretion rate, masses, and orbital separation was motivated by the study of the classical novae population by Townsley & Bildsten (2005). They showed that the observed orbital period distribution of the CNe was consistent with expectations of the mass transfer rate history of cataclysmic variables. This implied that the most often observed CNe would be those in 4-7 hours orbital periods with a mass transfer rate driven by magnetic braking at $10^{-9}\,M_\odot\,{\rm yr}^{-1}$. These tight orbits then enable Roche lobe overflow when the WD undergoing the CN reaches a photospheric radius $R_{\rm WD} = R_{\rm RL}$, triggering the mass loss from the WD that creates a common envelope. Within `MESA` this mass loss is simulated by eliminating any mass beyond the Roche lobe radius, effectively demanding that the WD photosphere not exceed $R_{\rm RL}$. It is simply the hydrostatic expansion of the actively burning layer that pushes the outer layers beyond $R_{\rm RL}$. Once the hydrogen layer mass has reduced to a value where $R_{\rm WD} \lesssim R_{\rm RL}$, the mass loss ends and the period of prolonged stable burning ensues. Since the ignition masses are smaller on more massive WDs, the expectation is that, even though rarer, more massive WDs will be more prevalent in the observed

population.

Kato & Hachisu (1994) have accounted for mass loss in novae through optically thick winds driven by an opacity bump at $\log T(\mathrm{K}) \approx 5.2$ from the OPAL tables. This bump in opacity should cause a decrease in the Eddington luminosities, making our super Eddington wind prescription a plausible mass loss mechanism. We present results using both mass loss mechanisms independently, but it's likely that some combination of winds and Roche lobe overflow are present in actual novae. Finally, we again neglect convective dredge-up and the accompanying metal enrichment of the burning layer.

The evolutionary tracks of our $0.6\,M_\odot$, $1.0\,M_\odot$, $1.2\,M_\odot$, and $1.3\,M_\odot$ models just after the end of mass loss are shown on the HR diagram with respect to the stable burners of §2.3 for both mass loss prescriptions in Figure 2.10. There we show the CNe as lines with markers on them denoting equal time steps after mass loss has ended. For instance, the RLOF 0.60 $M_\odot$ model burns steadily for approximately 250 years, whereas our RLOF 1.20 $M_\odot$ model only does so for approximately a year. The duration of the supersoft source (SSS) phase is clearly dependent on both the WD mass and the amount of mass ejected. The super Eddington wind models tend to start "later" in the steady-state locus since the super Eddington winds remove more mass than RLOF. As a result, those turn-off times are always shorter than the those of the corresponding RLOF models. We found there is some cutoff mass that depends on orbital parameters below which novae fill their Roche lobe before the luminosity goes super Eddington. For the models shown, the 0.6 $M_\odot$ and 1.0 $M_\odot$ fill their Roche lobes before going super Eddington, so the RLOF

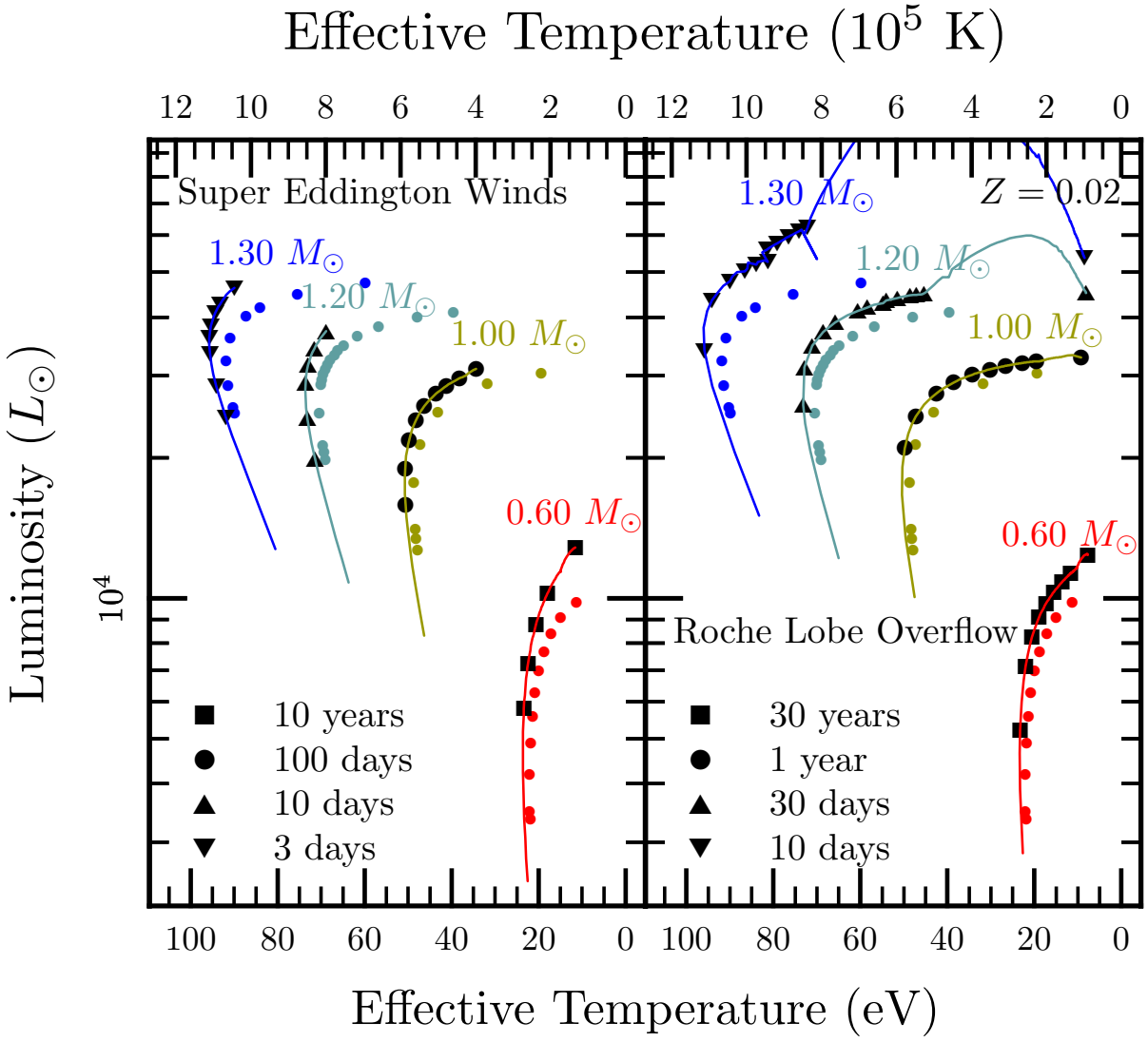

Figure 2.10 The paths of the CNe through the HR diagram after outburst (lines) with the static positions of the steadily-burning models presented earlier (circles). Models using super Eddington winds are on the left, and those using RLOF are on the right. For both mass loss mechanisms, we divide the tracks into equal time portions with markers whose time lengths are indicated in the legend.

prescription is likely more accurate. For the higher masses, the Roche lobe is bigger, allowing for greater expansion, leading to lower envelope temperatures, greater opacities, and thus a lower Eddington limit. The super Eddington models for these higher masses never expanded to the Roche lobe radius set for the RLOF models. Additionally, we can see that during the contracting phase, the RLOF 1.2 $M_\odot$ and 1.3 $M_\odot$ WDs are super Eddington (the upwards excursion), so the mass loss in those cases is certainly a lower limit.

After mass loss (on the far red end of each evolutionary track), each CN passes near or directly through the locus of stably burning phases corresponding to its mass. However, at an accretion rate of $\dot{M} = 1.0 \times 10^{-9}\, M_\odot\, \mathrm{yr}^{-1}$, the stable burning consumes hydrogen faster than it is accreted. Thus, a CN passes through phases with a progressively smaller hydrogen layer, tracing a path to and around the knee until the layer becomes thinner than that of the critically stable WD configuration. Sala & Hernanz (2005) modeled CNe in the post-outburst phase as a series of stably-burning WDs and tracked their evolution for four envelope compositions. Their Figure 1 gives HR diagram paths as well as the evolution of the hydrogen-rich layer in each of their modeled CNe. Their asymptotic luminosities and effective temperatures for the most metal-poor configuration (ONe25, at $Z_{\mathrm{env}} = 0.25$) agree well with our stable burners, though we find that the CNe themselves follow tracks that are marginally brighter and hotter than the corresponding stable burners. The depleting hydrogen layer is very apparent in Figure 2.11, where we see that the WDs using RLOF realize states with hydrogen masses and T_{eff}'s very close

to the corresponding steadily burning WDs. However, the WDs using super Eddington winds typically removed more mass than the RLOF models, so they "skip" some or most of the steady-state configurations and instead start with a much lower envelope mass. This disparity in the amount of fuel between the two configurations at the same mass explains why the turn-off times are much shorter for super Eddington winds than RLOF. In either cases, hydrogen burning becomes an insignificant source of luminosity past the lowest $\dot{M}$ stable burner state, and the WD then proceeds down the WD cooling track at nearly constant radius and hydrogen mass. Comparing to the ONe25 model in Sala & Hernanz (2005), we observe turn-off times that are always longer in the RLOF and low-mass super Eddington cases. For the higher mass super Eddington models, we observe marginally shorter turn-off times, likely driven by the skipped steady-state modes. The overall trend is that nearly all turn-off times in Sala & Hernanz (2005) are shorter than ours due to the significant metal enrichment of their envelopes, which is an important difference we elaborate on later.

Figure 2.12 shows the temperature profile of the 1.0 $M_\odot$ CN at four distinct stages: the low luminosity accreting state, the peak of hydrogen burning during the TNR, the point of highest $T_{\rm eff}$, which is near the end of stable burning, and the cooling/accumulating phase just after stable burning has ceased. For each profile, the location of the base of the hydrogen-burning layer (here approximated as the location where $X = 0.1$) is marked. For comparison, the lowest-$\dot{M}$ 1.00 $M_\odot$ stable burner is also shown in the gray line. As the hydrogen accumulates in the low-luminosity state, the profile is somewhat similar to

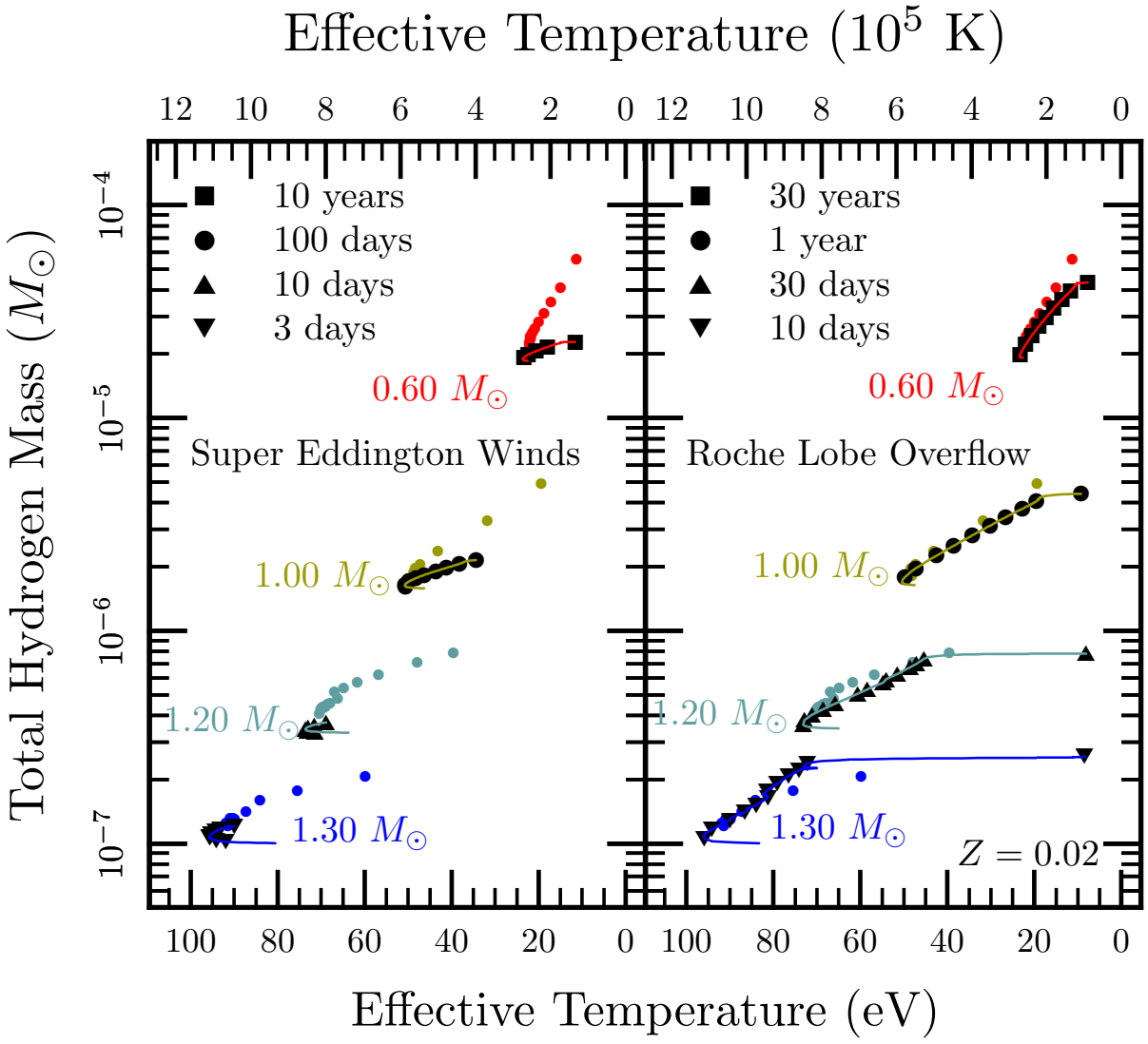

Figure 2.11 The hydrogen mass against the effective temperature of post-outburst CNe (lines) compared to steady burners of the same mass (circles). Models using super Eddington winds are on the left and those using RLOF are on the right. The RLOF novae pass through phases closely resembling their steadily-burning counterparts at the same effective temperatures, but the stronger mass loss from super Eddington winds cause novae to start stable burning at a much lower envelope mass than the corresponding RLOF models. Equal time markers are the same as mentioned in Figure 2.10.

a cooling WD, albeit with some heat still left over in the helium layer as well as some energy generation due to the compressional losses from accretion (see Figures 26 and 27 in Paxton et al. (2013)). Once the pressure at the base of the hydrogen reaches a critical threshold, the thermonuclear runaway (TNR) ensues, raising the temperature at the base to almost 2×10^8 K, which in turn drives a convective zone in the hydrogen layer. The radius then expands, triggering Roche lobe overflow until the envelope's thermal structure is reorganized so that it can carry the luminosity from the hydrogen burning. It then enters the stable burning phase, during which we see a temperature profile in the hydrogen-rich layer that is very similar to a steadily burning WD. Note that between the TNR and the SSS phase, approximately 90 percent of the hydrogen layer has been lost. A small portion of this is due to the stable burning, but the majority is due to RLOF. After stable burning ceases, the envelope cools and accretes hydrogen until the next TNR repeats the process.

Combined measurements of $T_{\rm eff}$ and the turn-off time of a CN (Henze et al., 2011) can be used to infer the WD mass. Figure 2.13 shows observed turn-off times and $T_{\rm eff}$'s in post-ouburst novae. Included in Figure 2.13 are data from M31 (Henze et al., 2011, 2013) and galactic sources (Rauch et al., 2010; Osborne et al., 2011; Beardmore et al., 2012). For the Henze et al. (2011) dataset, we've only included data that had reported uncertainties rather than limit points, which discriminates against longer-lived SSS phases since they are less likely to be observed from beginning to end. We also plot our calculations, where we define the turn-off time as the time between the beginning of mass loss and when the

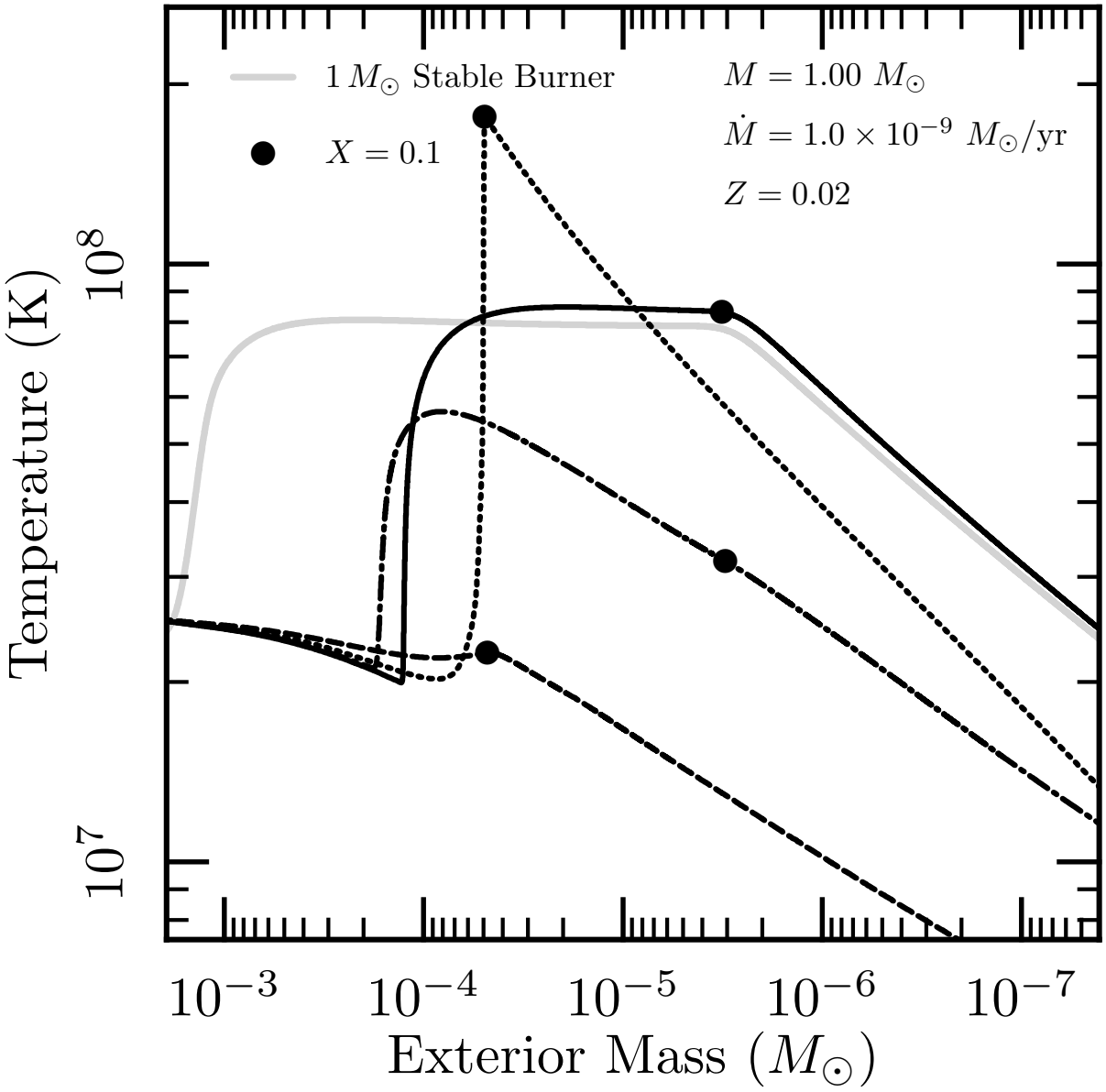

Figure 2.12 Time series of temperature profiles in a 1.00 $M_\odot$ WD accreting solar material at $\dot{M} = 1.0 \times 10^{-9}\ M_\odot\,\mathrm{yr}^{-1}$ with RLOF for mass loss. The point shows the base of the H layer. The long-dashed line is just prior to the outburst, when the luminosity is low and due primarily to compressional heating. The dotted line is the profile at the time of peak hydrogen burning, with a vigorously convective layer extending from the point of peak burning. The solid line is taken from the time at which $T_{\rm eff}$ is at a maximum, marking the end of the stable burning phase. The dash-dotted line is from shortly after the stable burning ceases, as the envelope is cooling off and accumulating hydrogen. The gray line is the profile of a 1.00 $M_\odot$ WD accreting at the lower stable limit.

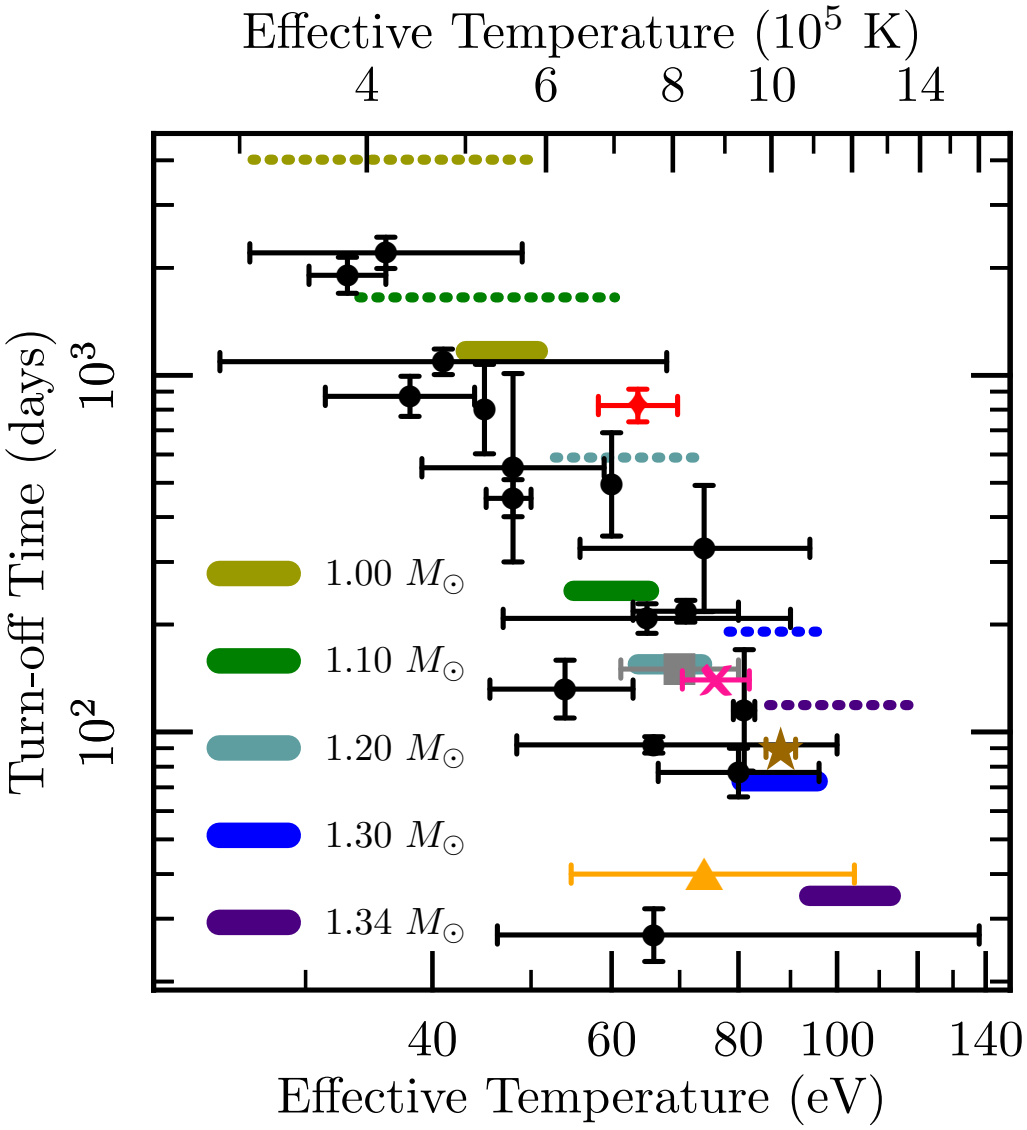

Figure 2.13 Turn-off time against $kT_{\rm eff}$ for observed CNe from the catalogue of M31 CNe in Henze et al. (2011) (black dots), the CN in globular cluster Bol 126 in M31 (Henze et al., 2013) (orange triangle), V4743 Sgr (Rauch et al., 2010) (red diamond), the recurrent nova RS Oph (Osborne et al., 2011) (brown star), HV Ceti (Beardmore et al., 2012) (gray square), as well as the results of our work. Solid lines represent the super Eddington wind models and the dotted lines represent RLOF models. The range of effective temperatures shown for the computational models are the temperatures during the latter 70% of the stable burning period. Note that the $T_{\rm eff}$ for the `MESA` simulations are from the Stefan-Boltzmann law given a luminosity and a photospheric radius. $T_{\rm eff}$'s from Henze et al. (2011, 2013) are blackbody approximations taken from X-Ray spectra, and $T_{\rm eff}$'s from the galactic novae are from NLTE models of hot WD atmospheres. These temperatures can differ by $\approx 10\%$ due to radiative transfer effects.

luminosity falls below one quarter of the peak luminosity of the stable burners of the same mass. This ending criteria isn't very crucial since the luminosity evolution after the stable burning phase is very rapid compared to time spent doing stable burning. For the computational models, we cannot report a single $T_{\rm eff}$ since it increases through most of the SSS phase. The turn-off time is well defined, so we report our results as a horizontal line in Figure 2.13 with the effective temperatures being those during the latter 70% of stable burning (the SSS is likely obscured at earlier times by the expanding ejecta shell).

The temperatures reported for the observed CNe are obtained either by approximating an X-ray spectrum as a blackbody (Henze et al., 2011, 2013) or through more sophisticated NLTE simulations (Rauch et al., 2010; Osborne et al., 2011; Beardmore et al., 2012). These two methods can yield different temperatures by $\approx 10\%$ (see Figure 4 from Henze et al. 2011), so there will necessarily be disagreement between CNe analyzed by the two different methods. Our models do not account for dredge-up and the subsequent metal enrichment of the ejecta and stably-burning envelope. This could cause two effects. First, the enriched TNR could burn more vigorously, driving stronger mass loss and thus shortening the turn-off time. Secondly, the remnant envelope after mass loss will be metal-enriched and will thus burn through the remaining hydrogen more quickly than if the same mass were at solar abundance, as shown in Sala & Hernanz (2005). Both of these factors indicate that our turn-off times are longest limits for the given mass loss prescriptions. We do not, however, expect metal enrichment to greatly alter the effective temperature of the outburst, so these can still be used to constrain WD masses. Finally,

the observed data shown in Figure 2.13 are deficient in low-temperature ($kT_{\rm BB} < 30\,{\rm eV}$) events.

Such events do exist, but the available measured turn-off times for them are lower limits since they have not been observed for a long enough time to detect both turn-on and turn-off. Additionally, observing such events is difficult due to absorption by interstellar neutral hydrogen and the overall weaker X-Ray flux. Finally, such low-mass systems may be more numerous, but since their recurrence times are significantly longer than their higher-mass counterparts, they are observed less often. In Figure 2.13 we only plot those events from Henze et al. (2011) that have established uncertainties in both the blackbody temperature and the turn-off time. The agreement between theory and observation in this region of parameter space is strong, implying that most of the novae with SSS phases that have established turn-off times and blackbody temperatures have $M \geq M_{\odot}$. As X-ray monitoring of M31 continues, more SSS's will turn off and stacked pointings allow for detection of fainter SSS's. Thus we will soon be able to probe more reliably into the lower-mass regime (Henze 2013, private communication).

Due to the variability of $T_{\rm eff}$ during the SSS phase, it is not an ideal tracer of WD mass on its own. The turn-off time, however, is a function of the luminosity and hydrogen mass layer size, assuming the mass loss history is known. Since we've seen that $\Delta M_{\rm H}$ decreases with increasing $M_{\rm WD}$ while L increases with increasing $M_{\rm WD}$, the turn-off time should be a consistent tracer of WD mass while also being relatively easy to measure. Using our high-mass CNe models, including an additional $1.34\,M_{\odot}$ CN, we find power

laws relating turn-off time to WD mass given by $M_{\rm WD} = 1.20\,M_\odot\,(513\text{ days}/t_{\rm off})^{0.081}$ (for RLOF) and $M_{\rm WD} = 1.20\,M_\odot\,(137\text{ days}/t_{\rm off})^{0.089}$ (for super Eddington winds). We then apply this relation to the catalogue of Henze et al. (2011) to get corresponding WD masses to compare to the reported ejection masses, which were inferred by Henze et al. (2011) from the turn-on time and the ejecta velocity. The results of this analysis are shown in Figure 2.14. We see the mapping from turn-off time to $M_{\rm WD}$ gives a similar relation between WD mass and ejected mass as the simulations for either mass loss prescription. Note though that the RLOF law gives super-Chandrasekhar mass WDs for sufficiently low turn-off times, which is a result of the under-prediction of mass loss in high-mass WDs in the RLOF assumption.

2.7 Case Study: M31N 2008-12a

A particularly interesting nova with a detected post-outburst SSS phase is M31N 2008-12a, which is a recurrent nova with a recurrence time of about a year (Tang et al., 2014; Henze et al., 2014a; Darnley et al., 2014) and possibly as short as six months (Henze et al., 2015). It has been erupting since at least 1992 when its recurrent X-ray emission was detected and correctly identified as the result of hydrogen burning on a WD surface by White et al. (1995). After its 2013 outburst and optical detection by the Palomar Transient factory (Tang et al., 2014), followup on Swift revealed a post-outburst supersoft phase that ended roughly 16 days after optical peak. We show their binned X-ray spectra for three durations of the SSS phase and their best-fit blackbody models in Figure 2.15.

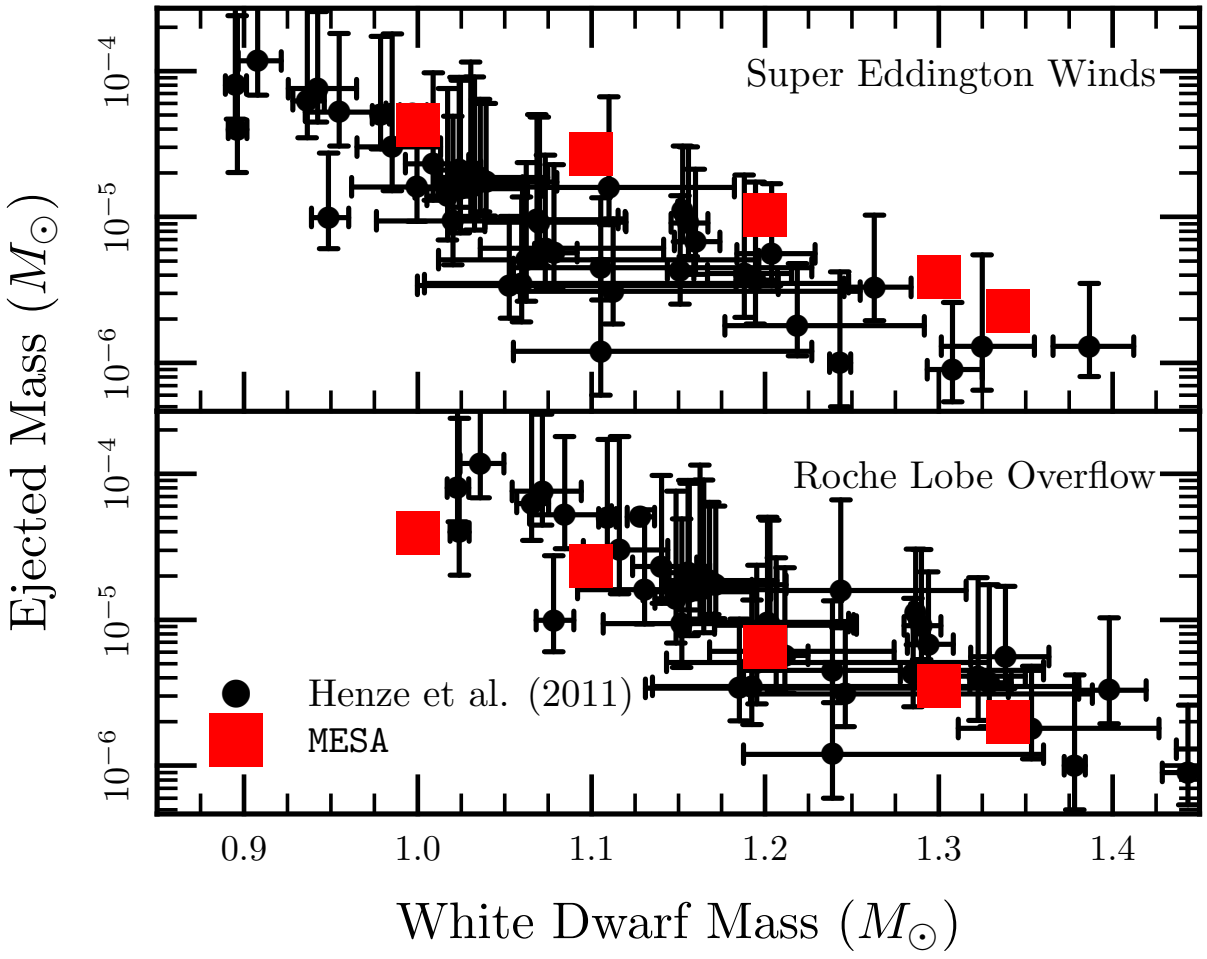

Figure 2.14 Ejected mass in a nova as a function of WD mass for both the MESA simulations as well as the same catalogue of observations used in Figure 2.13. The masses for the observed data were obtained by using a power law fit from the simulated data to convert turn-off times to masses.

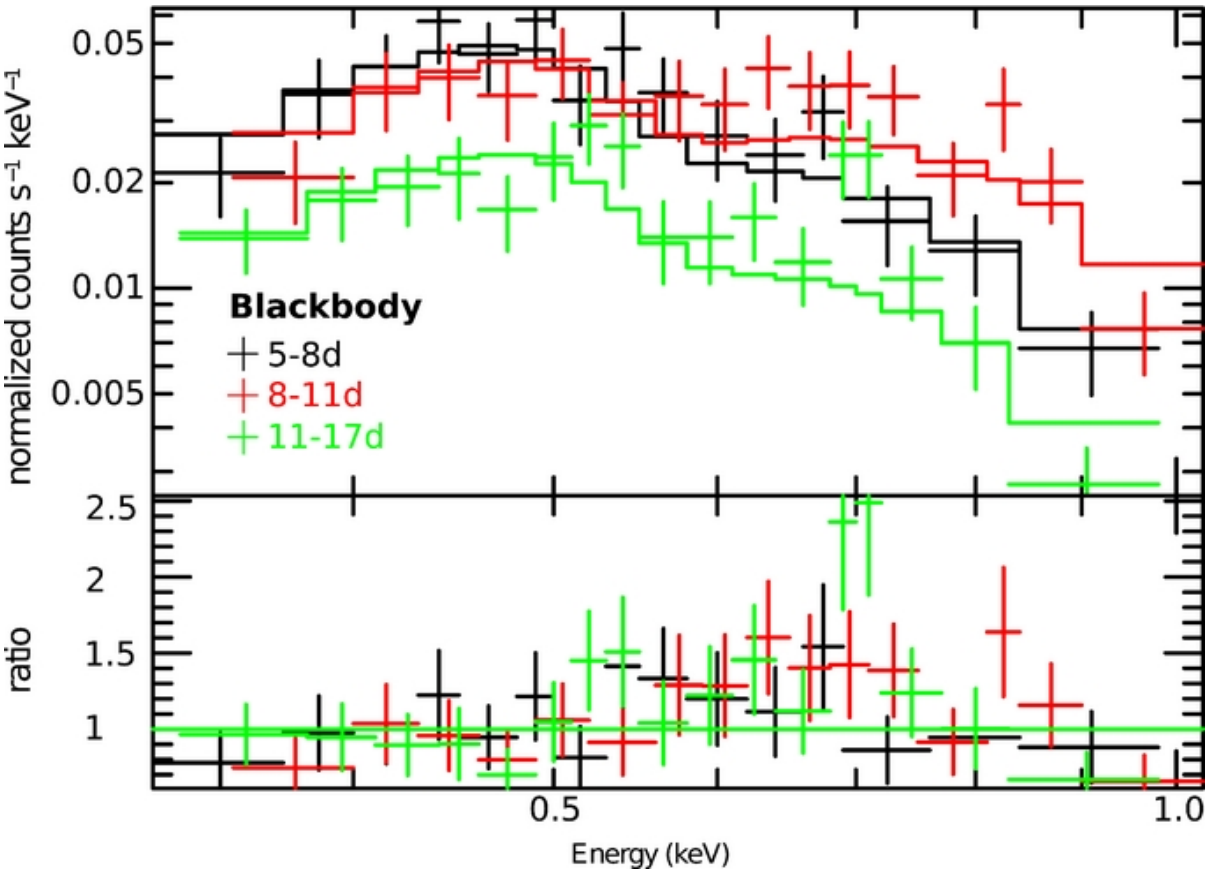

Figure 2.15 Swift XRT spectra (from 0.3 to around 1 keV) of M31N 2008-2012a taken at different time bins during the supersoft phase are shown with their best-fit blackbody spectral models assuming a fixed column $N_{\rm H} = 1.5 \times 10^{21}$ cm^{-2}.

The blackbody fits are done for two possible hydrogen columns, $N_{\rm H} = 10^{21}$ cm^{-2} and 1.5×10^{21} cm^{-2}. In either case, the peak effective temperatures are in excess of 10^6 K, and their peak luminosities are in the range of $5 \times 10^4 - 10^5$ $L_\odot$.

The short nova recurrence time, rapid evolution as an X-ray source, and high surface temperature during the SSS phase all consistently point to a high mass WD. To quantify just how large the WD mass must be to explain the observations, we expanded upon the work in §2.6 by simulating WDs with $M = 1.30$, 1.32, 1.34, and 1.36 $M_\odot$ accreting material with solar composition. We focused on models that gave the observed recurrence time of 1 year, yielding an accretion rate range of $1.7 \times 10^{-7} < \dot{M}/M_\odot \ {\rm yr}^{-1} < 3.3 \times 10^{-7}$. We used the super Eddington wind mass loss prescription for these models.

Our calculations allow us to immediately conclude that the WD in M31N 2008-12a has a mass of at least 1.3 $M_\odot$, as lower mass WDs could not yield a minimum recurrence time as short as 1 year (see Table 2.3 and Figure 2.8). The $\dot{M}$'s for the 1.32, 1.34, and 1.36 $M_\odot$ models that yielded recurrence times closest to $t_{\rm recur} = 1$ year were, respectively, 3.1×10^{-7}, 2.1×10^{-7}, and 1.7×10^{-7} $M_\odot$ yr^{-1}. These models retained $\approx 30\%$ of the accreted material through the outburst, yielding effective accretion rates onto the helium layer of $\dot{M}_{\rm WD} \approx 9 \times 10^{-8}$, 9×10^{-8}, and 6×10^{-8} $M_\odot$ yr^{-1}. Assuming this matter ultimately stays on the WD and that the effective accretion rate remains constant, these models would evolve to $M = 1.37$ $M_\odot$ within 5×10^5 years.

We next studied the location of these high mass WDs in the HR diagram during the SSS phase, all of which enter the SSS phase after only about 10-20 days from the onset

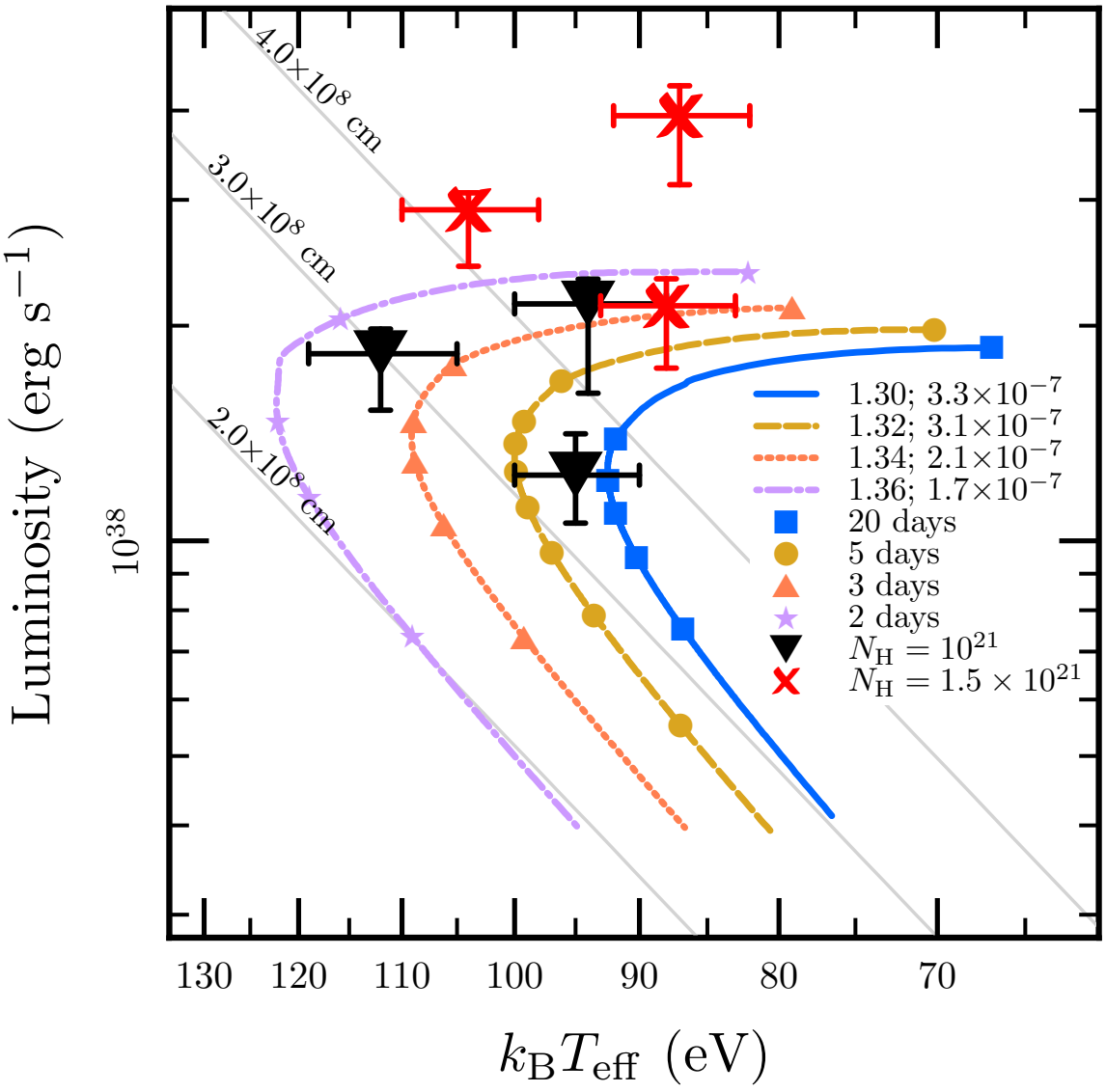

Figure 2.16 Comparison of observations vs. theoretical models on the luminosity vs. $k_B T_{\rm eff}$ plane during the SS phase of M31N 2008-12a. Best-fit results from the Swift XRT data using an absorbed blackbody model with fixed $N_{\rm H} = 1.0 \times 10^{21}$ cm^2 and $N_{\rm H} = 1.5 \times 10^{21}$ cm^2 are shown in black upside down triangles and red crosses, respectively, with the top-right point from the early stage (5-8 days after optical peak), the middle-left point from the middle stage (8-11 days after optical peak), and the lower-right point from the late stage (11-17 days after optical peak). Evolutionary tracks for the four `MESA` models with $t_{\rm recur} \approx 1$ yr are shown in thick colored lines with markers; all the tracks evolve from higher luminosity to lower luminosity. Different lines indicate different WD mass and $\dot{M}$ combinations (indicated in the legend in units of $M_\odot$ and $M_\odot$ yr^{-1}), and the markers separate periods of equal time which are also indicated in the legend. Also shown in gray are lines of constant radius.

of the TNR. As shown in Figure 2.16, all model tracks are consistent with the measured $T_{\rm eff}$ from M31N 2008-12a for either absorption model, and luminosities are similar as well. However, the WDs have different rates of evolution in the HR diagram depending on their mass as denoted by the solid points that denote the elapsed time between each point, similar to Figure 2.10. For example, the 1.34 $M_\odot$ WD evolves through the SSS phase in about 15 days, whereas the 1.36 $M_\odot$ WD is in a SSS phase for only 8 days. Clearly, the 1.30 $M_\odot$ WD evolves far too slowly. So, this comparison again points to WD masses of $1.30 < M/M_\odot < 1.36$ in our super Eddington wind model, with mass loss due to Roche lobe overflow indicating more massive WDs. The turnoff times could be shorter if there was substantial mixing of elements heaver than hydrogen into the burning layer during the TNR, pointing to WD masses at the lower end, i.e., $M = 1.30\ M_\odot$.

2.8 Concluding Remarks

We have presented stably burning WD models, found the lowest $\dot{M}$'s that permit such stable burning, and verified that they are consistent with other time-dependent studies as well as time-independent linear analysis studies of stability. We've shown that the hot helium ash left over from hydrogen burning dominates the thermal structure of both stably and unstably burning WDs at high $\dot{M}$'s. This helium layer is important because it sets the recurrence times for rapidly accreting recurrent novae where dredge up is unable to reach the WD core, but it is also important because it is likely to ignite unstably once it has grown large enough. The mass of helium in the WD, $\Delta M_{\rm He}$, is not a static

property of a stably burning model. For the 1.00 $M_{\odot}$ example shown in Figure 2.4, $\Delta M_{\rm He} \approx 1.5 \times 10^{-3}\ M_{\odot}$, but it will continue to grow at the accretion rate, $\dot{M}$, until the pressure and the temperature at the base become high enough to initiate unstable helium burning. Sienkiewicz (1980), Iben & Tutukov (1989), and Cassisi et al. (1998) showed that the stable burning regimes for hydrogen and helium are mutually exclusive for the case of solar composition accretion. However, Yoon et al. (2004b) offer a way to merge the two stability regimes if a large amount of differential rotation is allowed in the burning shells. Our calculations assume no rotation, and we observed unstable helium burning for WDs that were allowed to continuously accrete.

Finally, we showed how CNe pass through the stably burning phases after their outburst and subsequent mass loss. The duration of this SSS phase is highly sensitive to the mass of the underlying WD, spanning for hundreds of years for $M_{\rm WD} \approx 0.60\ M_{\odot}$ to mere tens of days for $M_{\rm WD} \approx 1.30\ M_{\odot}$. This variety of durations indicates a mapping from observed turn-off times to WD mass, though a study of the effects of metal enhancement and a better understanding of mass loss is necessary to get a more precise relationship. We then used the results of this work to constrain the mass of the WD in nova M31N 2008-12a to $1.30 < M_{\rm WD}/M_{\odot} < 1.36$.

We thank Ken Nomoto for helpful discussions regarding the calculations in Nomoto et al. (2007). We also thank Pablo Marchant for his useful binary Roche lobe overflow routines that were used in this work and Jeno Sokoloski for consultation regarding RNe observations. Finally, we thank Martin Henze and the referee for very helpful comments.

Most of the simulations for this work were made possible by the Triton Resource. The Triton Resource is a high performance research computing system operated by the San Diego Supercomputer Center at UC San Diego. This work was supported by the National Science Foundation under grants PHY 11-25915, AST 11-09174 and AST 12-05574.

Chapter 3

Photoionization Heating of Nova Ejecta

The expanding ejecta from a classical nova remains hot enough ($\sim 10^4$ K) to be detected in thermal radio emission for up to years after the cessation of mass loss triggered by a thermonuclear instability on the underlying white dwarf (WD). Nebular spectroscopy of nova remnants confirms the hot temperatures observed in radio observations. During this same period, the unstable thermonuclear burning transitions to a prolonged period of stable burning of the remnant hydrogen-rich envelope, causing the WD to become, temporarily, a super-soft X-ray source. In this chapter, we show that photoionization heating of the expanding ejecta by the hot WD maintains the observed nearly constant temperature of $(1-4)\times 10^4$ K for up to a year before an eventual decline in temperature due to either the cessation of the supersoft phase or the onset of a predominantly adiabatic

expansion. We simulate the expanding ejecta using a one-zone model as well as the Cloudy spectral synthesis code, both incorporating the time-dependent WD effective temperatures for a range of masses from 0.60 $M_\odot$ to 1.10 $M_\odot$. We show that the duration of the nearly isothermal phase depends most strongly on the velocity and mass of the ejecta and that the ejecta temperature depends on the WD's effective temperature, and hence its mass.

3.1 Introduction

Classical novae (CNe) are caused by the ejection of $\Delta M_{\rm ej} \sim 10^{-4}\,M_\odot$ of matter from an accreting white dwarf (WD) triggered by a thermonuclear instability in recently-accreted hydrogen-rich matter (Gallagher & Starrfield, 1978; Starrfield et al., 2008). The expanding ejecta are bright in the radio for hundreds of days after the optical peak (Seaquist & Bode, 2008) and are well modeled by assuming the radiation comes from thermal bremsstrahlung emission from an expanding medium of nearly constant electron temperature $T_e \approx (1-4) \times 10^4$ K (Seaquist & Palimaka, 1977; Hjellming et al., 1979; Taylor et al., 1988; Eyres et al., 1996). Such temperatures are also observed via nebular spectroscopy long after optical peak in novae like V1974 Cygni 1992 (Austin et al., 1996) and T Pyxidis V351 (Shore et al., 2013). However, between the fading of the optical emission (which may correspond to the end of mass ejection) and the end of the radio emission several hundred days later, the ejecta undergo an expansion in volume by several orders of magnitude. In the absence of a heating source, the ejecta would

undergo adiabatic expansion, leading to a large temperature decline to values orders of magnitude less than the observed 10^4 K. The cause of these much higher temperatures for such prolonged periods is the focus of this chapter.

With the rise of frequent X-ray monitoring of classical novae, it is becoming increasingly clear that most, if not all, CNe are followed by a super-soft X-ray source (SSS) phase during which the WD shrinks in radius to nearly its pre-nova size, but continues to burn a remnant hydrogen envelope at nearly the Eddington luminosity as modeled by Starrfield et al. (1974), Fujimoto (1982a), Sala & Hernanz (2005), Hachisu & Kato (2010), and Wolf et al. (2013). This phase has been decteced in many galactic novae (Oegelman et al., 1984; Shore, 2008; Krautter, 2008; Schwarz et al., 2011), and observations in M31 are making it clear that a SSS phase is likely to follow every classical nova outburst (Henze et al., 2011, 2014b). During the SSS phase, the WD has $L \approx 10^4\,L_\odot$ and since it is compact, is a strong source of radiation at $kT_{\rm eff} \approx 50-100$ eV. This SSS phase can be as short as a few days for novae with the most massive WDs (Tang et al., 2014; Henze et al., 2014a) and as long as a decade for low-mass WDs like V723 Cas (Ness et al., 2008). We show here that the SSS phase is a sufficiently powerful source of photoionizing heating to sustain the high ejecta temperature long after the optical peak.

We start in Section 3.2 by reviewing the physics of photoionization balance and establish our simplified model of hydrogen and helium ionization in nova ejecta. We derive the temporal evolution of the ejecta temperature in Section 3.3 and discuss computational models in Section 3.4. We compare our semi-analytic results to the computational results

in Section 3.5, and end by showing how this new understanding can inform us about the properties of CNe ejecta, and, potentially, the WD mass.

3.2 Photoionization Balance

For the late time evolution of interest to us, we chose to model the nova ejecta at age t as one zone of constant mass $\Delta M_{\rm ej}$ in a uniform density sphere (i.e. not a shell) of radius $r(t) = v_{\rm ej}t$ expanding at constant velocity $v_{\rm ej}$. A hot WD of mass M and radius $R_{\rm WD}$ resides at the center. The ejecta has a composition $\mathbf{X}$, here represented as a vector of mass fractions. The number density of any given isotope, i, in the ejecta is

$$n(X_i) = \frac{3X_i\Delta M_{\rm ej}}{A_i m_p 4\pi v_{\rm ej}^3 t^3}, \tag{3.1}$$

where A_i is the mass number of isotope i and m_p is the proton mass. The electron-ion coupling time is always much shorter than the age, t, during the time relevant for our calculations, so there is only one temperature, $T(t)$. We express the fundamental equation of thermodynamics in terms of ejecta volume V, entropy S, and total number of particles N as

$$TdS = NkT\left(\frac{3dT}{2T} + \frac{dV}{V}\right) . \tag{3.2}$$

For a spherical ejecta of pure ionized hydrogen ($N = 2N_e$) with $r = vt$, this becomes

$$T\frac{ds}{dt} = n_e kT\left(3\frac{d}{dt}\ln T + \frac{6}{t}\right) . \tag{3.3}$$

where we now consider the specific entropy $s = S/V$ and n_e is the number density of electrons.

The only source of heating we will consider is that from the central, hot, WD in the SSS phase, which is a system that has been modeled extensively (Starrfield et al., 1974; Fujimoto, 1982a; MacDonald & Vennes, 1991; Sala & Hernanz, 2005; Hachisu & Kato, 2010; Wolf et al., 2013). We extended the work of Wolf et al. (2013) to generate the time-dependence of $T_{\rm eff}$ for a range of WD masses, as shown in Figure 3.1. These simulations used the 1-D stellar evolution code `MESA` (Paxton et al., 2011, 2013), following the time-dependent evolution of WDs accreting solar composition material at 10^{-9} $M_\odot$ yr^{-1} through several nova flashes with super-Eddington winds as the primary mode of mass loss. In particular, we only display the results from the end of mass loss until the end of quasi-stable hydrogen burning for one representative nova cycle. The original simulations did not have data for a 0.8 or 1.1 $M_\odot$ WD, so we generated additional data for this work. At any given age since mass loss ended, we know the WD radius and $T_{\rm eff}$, and hence the radiation field that powers the photoionization heating. This is the only information we use from the `MESA` models. The ejecta parameters $\Delta M_{\rm ej}$ and $v_{\rm ej}$ used are independent of the `MESA` models, and, in general, would vary significantly for novae on WDs of different masses.

3.2.1 Strömgren Breakout

Our first concern is whether the photoionization source is adequate to maintain a large region of mostly ionized plasma in the ejecta. Hence, we start by finding the Strömgren sphere radius, $R_{\rm S}$, and compare it to the ejecta dimension, $v_{\rm ej}t$. For simplicity, we assume pure ionized hydrogen ($n_e = n_p$) within the Strömgren sphere, and equate the rate of emission of H-ionizing photons by the WD, $Q_{\rm H}$, with the rate of recombinations in that volume,

$$Q_{\rm H} = \frac{4}{3}\pi R_{\rm S}^3 \alpha n_{\rm p} n_e \ , \tag{3.4}$$

where α is the radiative recombination rate of hydrogen.

At early times $R_{\rm S}$ is far inside the outer ejecta radius, $v_{\rm ej}t$, and the ratio scales as

$$\frac{R_{\rm S}}{v_{\rm ej}t} = \left(\frac{4\pi Q_{\rm H}}{3\alpha N_p^2}\right)^{1/3} (v_{\rm ej}t), \tag{3.5}$$

where N_p is the total number of protons. Hence, at early times, the Strömgren sphere is inside the ejecta, and only breaks out at an age of

$$t_{\rm S} \approx 30 \text{ d} \left(\frac{v_{\rm ej}}{10^3 \text{ km/s}}\right)^{-1} \left(\frac{\Delta M_{\rm ej}}{10^{-5}\ M_\odot}\right)^{2/3} \left(\frac{Q_{\rm H}}{10^{48}\ \text{s}^{-1}}\right)^{-1/3}, \tag{3.6}$$

where we have scaled $v_{\rm ej}$, $\Delta M_{\rm ej}$, and $Q_{\rm H}$ to values typical of novae on intermediate-mass WDs. Table 3.1 shows that the H Strömgren sphere breaks out by 50 days for all but the most massive WDs for $\Delta M_{\rm ej} = 10^{-5}\ M_\odot$ and $v_{\rm ej} = 10^3$ km s^{-1}. This confirms a time after which all of the ejecta is exposed to the photoionizing radiation field. The pure He breakout times for singly ionized He Strömgren spheres are systematically later due to less ionizing radiation available for a pure He ejecta. The more massive WDs have longer

Strömgren breakout times at the same ejecta parameters because while they produce harder spectra than lower-mass models, the total luminosity is not significantly higher, so the total number of ionizing photons emitted, Q, decreases, requiring more time for a complete ionization of the ejecta. Additionally, the SSS phases for the most massive models are short enough that the ionization front never makes it to the ejecta radius before the ionizing source fades greatly, causing excessively long Strömgren breakout times. We explore the ionization state of the ejecta at late times in Section 3.5.

Beck et al. (1990) performed a much more detailed calculation of this breakout for a He Strömgren sphere for a mixed ejecta with heavier elements ($Z > 2$), and a lower ejected mass and velocity ($\Delta M_{\rm ej} = 1.3 \times 10^{-6}\ M_{\odot}$ and $v_{\rm ej} = 6 \times 10^{2}$ km s^{-1} than we used for Table 3.1. So as to make a close comparison, we used their parameters, including their WD $T_{\rm eff}$ (see Figure 6 of Beck et al., 1990) as inputs to our homogenous model. We found that the H and He Strömgren breakouts occur at 31 days and 77 days, respectively, very close to the breakout they reported at $t = 76$ d for the He Strömgren sphere.

3.2.2 Ionization Timescale

After the Strömgren breakout, we allow that the ejecta may no longer absorb the majority of the photoionizing radiation. We characterize this via the optical depth, τ_{ν}, through the ejecta at frequency ν,

$$\tau_{\nu}(r) = \sum_{i} n(X_i)\ \sigma_{\rm pi}(\nu, X_i)\ r, \tag{3.7}$$

Table 3.1. Strömgren Breakout Times[a]

	H		He	
$M_{\rm WD}$ ($M_\odot$)	$t_{\rm S}$[b] (d)	$Q_{\rm H,47}$[c] (10^{47} s^{-1})	$t_{\rm S}$[d] (d)	$Q_{\rm He,47}$[e] (10^{47} s^{-1})
0.60	31	8.0	95	1.2
0.80	28	11.0	69	3.6
1.00	31	8.0	60	5.6
1.10	37	5.0	67	4.4
1.20	41	4.0	214	3.6
1.30	132	2.9	387	2.7

[a] $\Delta M_{\rm ej} = 10^{-5}\ M_\odot$; $v_{\rm ej} = 10^3$ km s^{-1}

[b] Strömgren breakout time for pure hydrogen

[c] Emission rate of H-ionizing photons

[d] Strömgren breakout time for pure helium

[e] Emission rate of He-ionizing photons

where $\sigma_{\rm pi}(\nu, X_i)$ is the photoionization cross-section and the sum is over all isotopes in **X**. The time an isotope can spend in the neutral state is set by the photoionization timescale, which we define at the ejecta outer radius ($r = v_{\rm ej}t$), giving

$$\frac{1}{t_{\rm ion}(X_i)} = \pi \left(\frac{R_{\rm WD}}{r}\right)^2 \int_{I_{\rm X_i}/h}^{\infty} d\nu \, \frac{B_\nu(T_{\rm eff})}{h\nu} \sigma_{\rm pi}(\nu) \ , \tag{3.8}$$

where $B_\nu(T_{\rm eff})$ is the Planck function evaluated for the WD $T_{\rm eff}$, and I_{X_i} is the ionization energy for isotope X_i.

We consider only the two most significant elements for photoionization heating; H and He. We assume that after the breakout time $n(X_i)$ is low enough that the ejecta is optically thin for Lyman limit photons ($h\nu = 13.6$ eV). In this limit we neglect any secondary ionization caused by a recombination emission (Baker & Menzel, 1938) and consider only hydrogenic ionization processes (essentially assuming there are no neutral helium atoms). This gives two dynamical expressions for the hydrogenic number density of hydrogen and helium, respectively

$$\dot{n}(H) = -\frac{n(\rm H)}{t_{\rm ion}(\rm H)} + n_e n(\rm H^+)\alpha(T, \rm H^+) \ ; \tag{3.9}$$

$$\dot{n}(\rm He^+) = -\frac{n(\rm He^+)}{t_{\rm ion}(\rm He^+)} + n_e n(\rm He^{++})\alpha(T, \rm He^{++}) \ . \tag{3.10}$$

As long as the WD is emitting, we found that the timescale over which these quantities relax is orders of magnitude smaller than the age of the ejecta, so we can consider an

instantaneous steady state solution, where $\dot{n}(X_i) = 0$, yielding

$$n(X_i)\left(\frac{1}{t_{\rm ion}} + P_{\rm ci}(T, X_i)\right) = n_e n(X_i^{+1})\alpha(T, X_i^{+1}) \ , \tag{3.11}$$

with $P_{\rm ci}(T, X_i)$ the temperature-dependent collisional ionization rate which we adopt from Lang (1980). This equation yields the very small neutral fraction that we must know to calculate the heating rate from photoionization.

3.3 Time-dependent Entropy Evolution

Now that we have shown that photoionization balance drives the neutral fraction to a low value after the breakout of the Strömgren sphere, we can consider the entropy evolution of the expanding ejecta, which will lead us to a temperature evolution. The photoionization heating timescale is much less than the age initially after breakout so that any information regarding the initial entropy is lost. This will simplify our calculation as we consider the state of the plasma under photoionization heating and radiative cooling, where we use a cooling function $\Lambda(T)$ determined by comparative simulations run in Cloudy as detailed in Section 3.4. The resulting rate of change of specific entropy s is then

$$T\frac{ds}{dt} = \Gamma_{\rm pi} - \Lambda(T) \ , \tag{3.12}$$

where the rate of photoionization heating, $\Gamma_{\rm pi}$, is given by

$$\Gamma_{\rm pi} = \sum_i \frac{n(X_i)}{t_{\rm ion}(X_i)} E_{\rm ion}(X_i) \ , \tag{3.13}$$

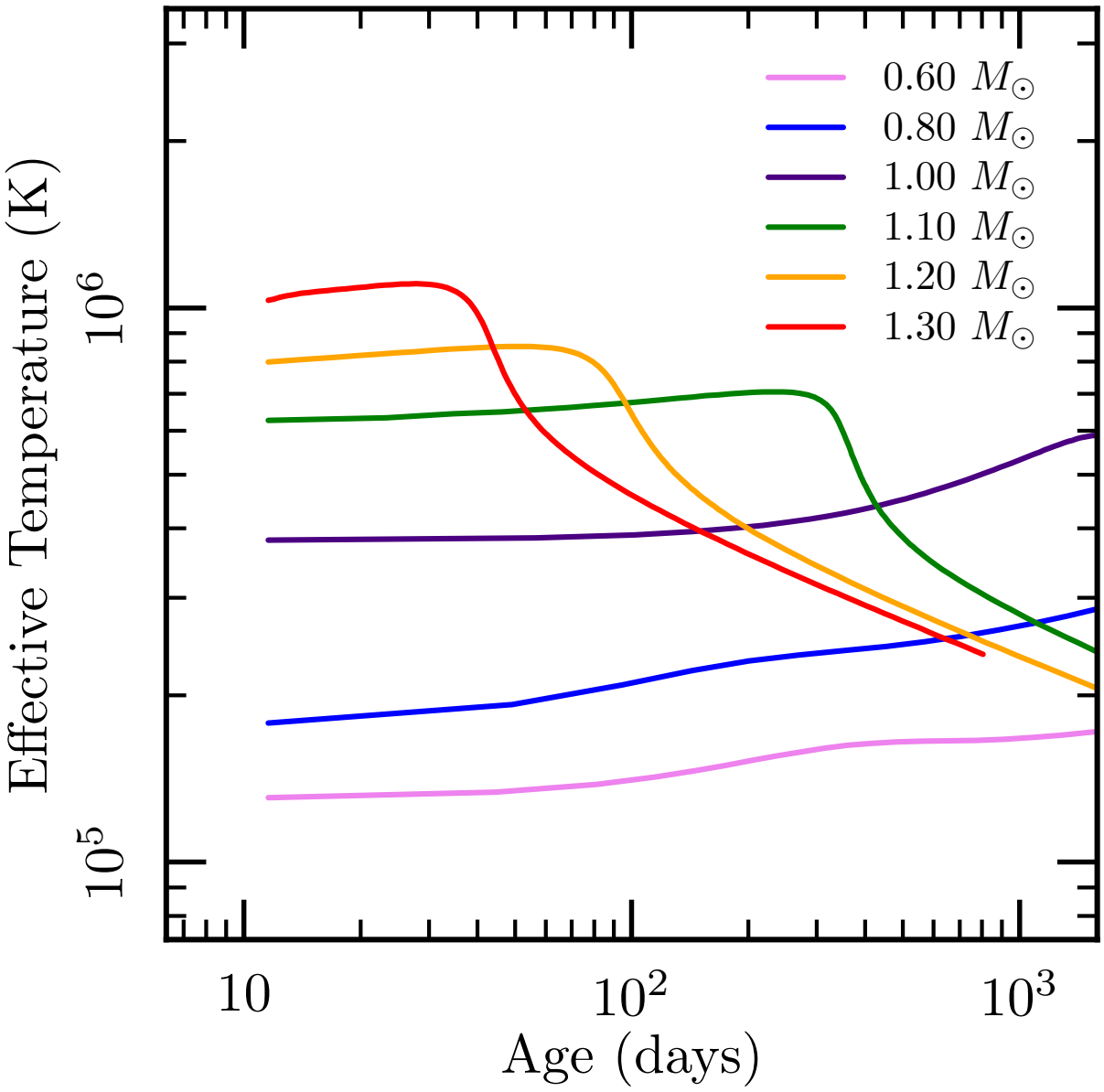

Figure 3.1 The calculated time dependent $T_{\rm eff}$'s of different mass WDs as simulated by Wolf et al. (2013), including two new cases (0.80 & 1.10 $M_\odot$) here. The age is the time since the end of mass loss driven by the thermonuclear instability. The rapid decline at later times for the three most massive WDs corresponds to the end of their SSS phases.

with $E_{\rm ion}(X_i)$ being the average photoelectron energy. Under the optically thin assumption $E_{\rm ion}$ is given by Draine (2011) as

$$E_{\rm ion}(X_i) = \frac{\int_{Z^2 I_{\rm H}/h}^{\infty} d\nu \, \frac{B(\nu,T)}{h\nu} \sigma_{\rm pi}(\nu, X_i)(h\nu - Z^2 I_{\rm H})}{\int_{Z^2 I_{\rm H}/h}^{\infty} d\nu \, \frac{B(\nu,T)}{h\nu} \sigma_{\rm pi}(\nu, X_i)}. \tag{3.14}$$

Using equations (3.3) and (3.12) we find the equation for $T(t)$ as

$$\frac{dT}{dt} = \frac{1}{3kn_e} \left[\Gamma_{\rm pi} - \Lambda(T)\right] - \frac{2T}{t} \ . \tag{3.15}$$

Finding a temperature evolution, $T(t)$, requires solving equations (3.13) & (3.15) simultaneously.

Before showing the detailed solutions of equation (3.15), it is best to first exhibit a few limits. The first limit is to assume that the plasma is nearly fully ionized, and that ionization balance is set by equation (3.11) but with little impact from collisional ionization. This yields a simple relation of $n_{\rm H}/t_{\rm ion} \approx n_e n_p \alpha$ and a heating rate of $\Gamma_{\rm pi} \approx E_{\rm ion} n_e n_p \alpha$. Since $t_{\rm ion} \ll t$ when the WD is hot, we found that ejecta of different initial temperatures would very rapidly (on a timescale much less than the age) reach a state of $\Gamma_{\rm pi} \approx \Lambda(T)$ and a temperature, $T_{\rm iso}$ nearly independent of the electron density. The scale of these heating and cooling terms (which nearly cancel in equation (3.15)) are so much larger than the $2T/t$ adiabatic expansion term that the ejecta evolves from one isothermal (heating balances cooling) state to the next under a condition of thermal and photoionization balance. The resulting nearly isothermal evolution of this phase then arises from the condition of $\Gamma_{\rm pi} \approx \Lambda(T)$ for different WD $T_{\rm eff}$'s. There is nearly no sensitivity to the actual electron density when in this limit, so ejecta clumping will not

matter, and all initial entropy information is lost.

However, the heating term, $\Gamma_{\rm pi}/n_e$, in equation (3.15) is $\propto t^{-3}$, implying that there will come a time, which we call $t_{\rm iso}$, beyond which the heating term is comparable to, or less than, the adiabatic expansion term, $2T/t$, and we expect to see a temperature decline. If we neglect radiative cooling, this critical timescale, $t_{\rm iso}$, is when $\Gamma_{\rm pi}/3kn_e = E_{\rm ion}n_p\alpha/3k = 2T/t$. For the case of pure, ionized Hydrogen this gives

$$t_{\rm iso} \approx 250\,{\rm d}\left(\frac{\Delta M_{\rm ej}}{10^{-5}\ M_\odot}\right)^{1/2}\left(\frac{v_{\rm ej}}{10^3\ {\rm km/s}}\right)^{-3/2}\left(\frac{E_{\rm ion}}{10\ {\rm eV}}\right)^{1/2}\left(\frac{kT}{1\ {\rm eV}}\right)^{-1/2}\times \left(\frac{\alpha}{10^{-13}\ {\rm cm^3\,s^{-1}}}\right)^{1/2}. \quad (3.16)$$

We will show in the following section that our detailed thermal evolution calculations for these remnants can be simply described by the arguments above, with nearly all solutions exhibiting a nearly isothermal phase for $t < t_{\rm iso}$, followed by a temperature decline.

3.4 Cloudy Simulations

We also simulated the nova ejecta using the radiative transfer code Cloudy (version 13.03, Ferland et al., 2013), which has been successfully used to model nova ejecta in the past by Schwarz (2002), Vanlandingham et al. (2005), and Schwarz et al. (2007). Cloudy allows a user to specify the density structure of a gas, its composition, and an incident radiation field. It then computes the ionization state of the material, yielding

line strengths, temperatures, and many other details, including realistic cooling curves.

To make the models in Cloudy as similar to our semi-analytic approach as possible, we set the radiation field at a given time to be a blackbody spectrum with the $T_{\rm eff}$ and radius set by the `MESA` models for that WD mass. The constant density gas reaches an outer radius $r_{\rm out}(t) = v_{\rm ej}t$ and an inner radius $r_{\rm in}(t) = 0.01 r_{\rm out}(t)$ essentially reproducing our constant density sphere model. To account for temperature decline from adiabatic expansion, we insert a "cooling" term

$$\Lambda_{\rm exp} \approx 2 \times 10^{-16} \Delta M_{\rm ej,-5}\, v_{\rm ej,3}^{-3}\, T_4\, t_8^{-4} \text{ erg s}^{-1} \text{ cm}^{-3}, \tag{3.17}$$

that matches the second term in equation (3.3), where $\Delta M_{\rm ej,-5} = \Delta M_{\rm ej}/(10^{-5}\ M_\odot)$, $v_{\rm ej,3} = v_{\rm ej}/(1000 \text{ km s}^{-1})$, $T_4 = T/(10^4 \text{ K})$, and $t_8 = t/(10^8 \text{ s})$. The ejecta material was set to have a solar (Cloudy's default abundance set) composition so that cooling by metals would be included. We then divide the WD evolution histories into twenty-one times, divided equally in log age, and use Cloudy to compute a temperature/ionization structure for the ejecta. These calculations assume that the cloud has reached both a photoionization and thermal equilibrium with the applied radiation field. We already established in Section 3.3 that these are valid assumptions at early times while $t_{\rm ion} \ll t$, so these Cloudy simulations provide physically motivated snapshots at those early times of concern for us. Essentially, these simulations in their current form solve (3.15) assuming $dT/dt = 0$ and do not incorporate dynamic effects other than the artificially inserted adiabatic cooling.

For these simulations, we found that the temperature was rather constant with radius,

leading to a single temperature for each model that we defined as the mass-average over the outer 50% of the mass. These temperature histories are what we compare to the semi-analytic models in Section 3.5. For later use in our semi-analytic work (e.g. equation (3.15)) we also extracted a cooling curve by finding the volumetric cooling rate at each grid point, subtracting off the portion of that cooling due to expansion from equation (3.17), and then dividing by $n_{\rm H} n_e$. The resulting cooling curves depend on the WD $T_{\rm eff}$ (and hence WD mass) due to different degrees of ionization and line cooling. We thus generated characteristic Cloudy cooling curves for each WD mass by choosing a time in the Cloudy calculations about halfway through the observed temperature plateau in log age. At times beyond these, the heating and cooling timescales become comparable to the age, and we can no longer trust the equilibrium Cloudy calculation, but rather should solve the fully time-dependent problem. We make progress on that aspect in the Section 3.5.

Since Cloudy is inherently a multi-zone code, we can use it to test our assumption that the density profile and composition has little influence on the temperature structure of the ejecta. We ran four models with our fiducial ejecta parameters of $\Delta M_{\rm ej} = 10^{-5}\ M_\odot$ and $v_{\rm ej} = 1000\ {\rm km\,s^{-1}}$ with the radiation field given by the 1.00 $M_\odot$ WD model. These four models used two different density distributions, constant and inverse square, as well as two sets of elemental abundance ratios, solar and nova. The nova abundances are a built-in option in Cloudy and are intended to model the abundanes observed in the ejecta of nova V1500 Cygni (Ferland & Shields, 1978). Since the adiabatic cooling is

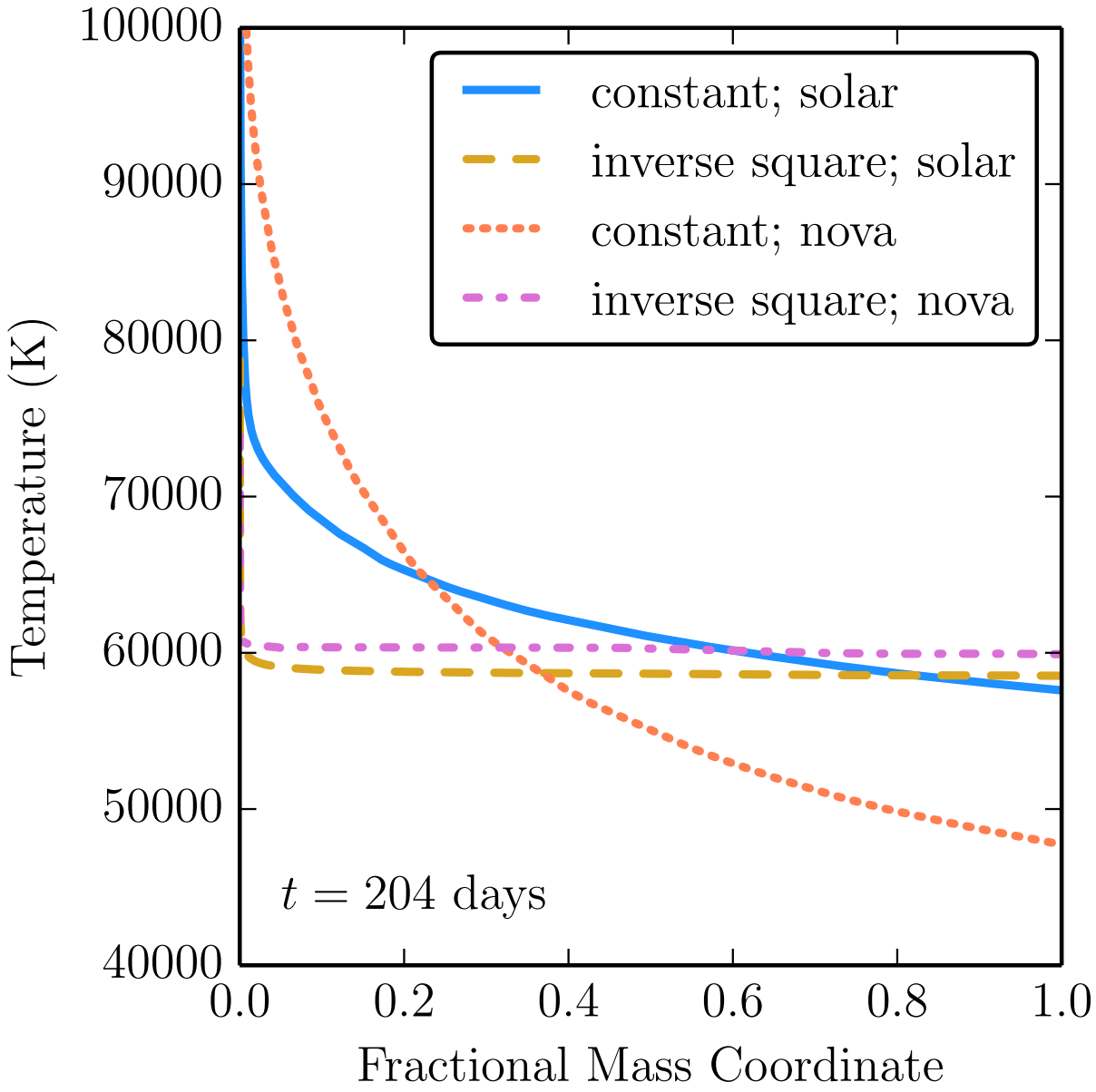

Figure 3.2 Temperature profiles of Cloudy simulations of nova ejecta with varying density profiles and compositions. Each represents 10^{-5} $M_\odot$ of ejected material with an outer velocity of 1000 km s^{-1} being heated by radiation from a 1.00 $M_\odot$ WD SSS. The abscissa measures the total enclosed mass at a given shell radius, with the outermost point being the position enclosing all the mass and a radius of $v_{\rm ej}t$.

necessarily radius-dependent for a non-constant density profile, the simple extra cooling of equation (3.17) could not properly model expansive cooling. To be consistent, we included no extra cooling from expansion in this comparision study, resulting in hotter temperatures and longer "plateau" periods. The temperature profiles of all four cases at a time approximately 200 days after ejection are shown in Figure 3.2. Importantly, the temperature range changes no more than by order unity in the constant density models and is nearly exactly isothermal in the inverse square cases. Also, the temperatures for these models do not change greatly as the density profile and/or composition are changed, allowing us to use our simple solar composition and constant density assumptions in our semi-analytic model. One important difference between the different density profiles is that the opacity at the lyman-limit diverges as we let the inner radius go to zero in the inverse square case. While a vanishing central radius is certainly unphysical, we must be aware that the time to become optically thick is sensitive to the choice for an inner radius. In this comparison we continued to use $r_{\rm in} = 0.01 v_{\rm ej} t$, which causes the initial optically thick phase to last significantly longer than the similar constant density models, sometimes approaching 100 days.

3.5 Results

The results of the one zone semi-analytic model and Cloudy simulations for WD mass 0.60, 0.80, 1.00, and 1.10 $M_\odot$ are shown in Figure 3.3 and Table 3.2 from the time-dependent WD models described earlier. All temperatures are in the 10^4 K region, con-

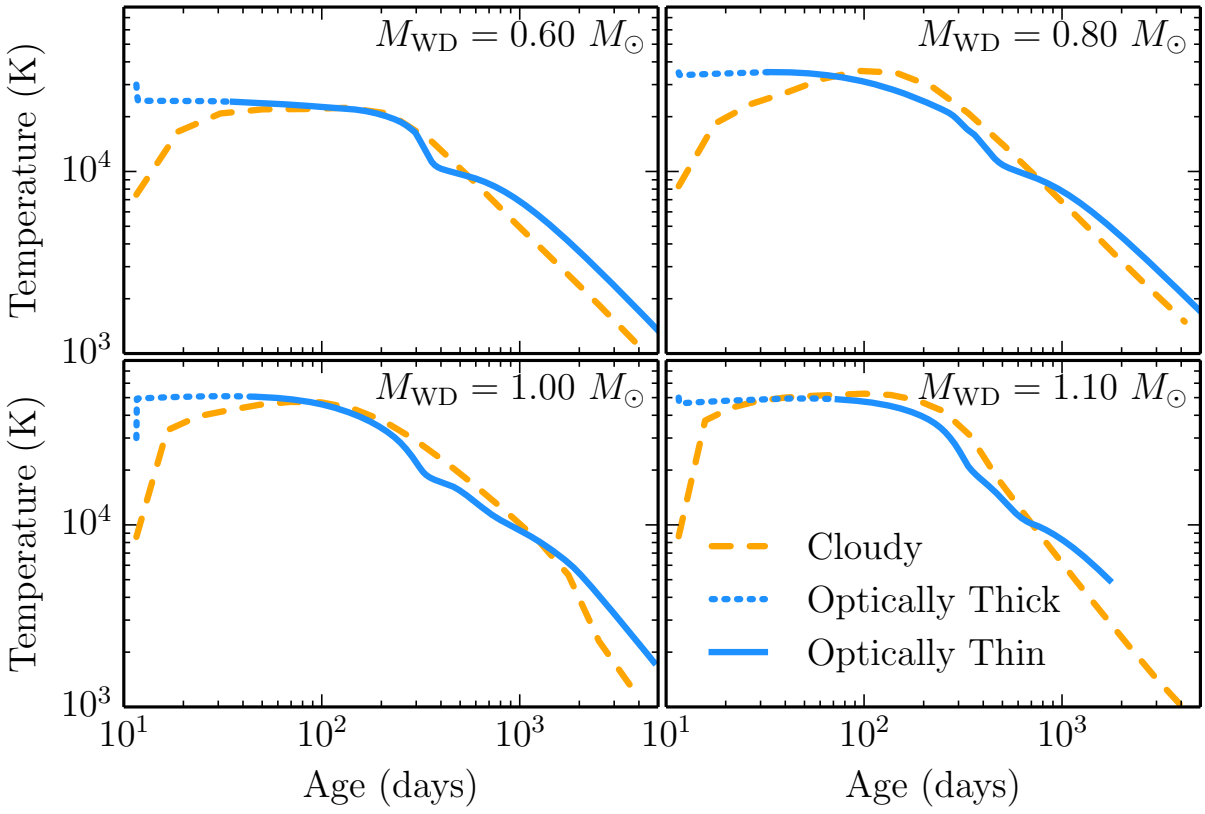

Figure 3.3 Temperature evolution of the nova ejecta for four WD masses using our semi-analytic model (blue) with cooling curves extracted from Cloudy and simulations run in Cloudy (dashed gold). $\Delta M_{\rm ej} = 10^{-5}\ M_\odot$ and $v_{\rm ej} = 1000\ {\rm km\,s^{-1}}$ for all models, and the time evolution of the incident radiation is set by the underlying WD mass via the histories shown in Figure 3.1. The dotted line indicates that the ejecta is optically thick at the Lyman limit edge at early times.

sistent with that inferred from radio observations and nebular spectroscopy, and show a long plateau of nearly constant temperature at the value expected for photoionization and thermal equilibrium. Results for the two higher-mass WD models are not shown for reasons described below.

The four WD evolutions shown exhibit a period of isothermal expansion lasting around 100-200 days that we will refer to as the plateau. Numerically, we defined this as the duration over which the the temperature stayed within 20% of the plateau tem-

perature $T_{\rm iso}$. These durations are in accord with the timescale predicted by Equation (3.16), and show that, even with the WD still providing a high level of photoionization, the adiabatic expansion term eventually plays an important role.

The two methods - one-zone model and Cloudy simulations - agree well for all four cases. The two higher WD mass simulations (1.20 $M_{\odot}$ and 1.30 $M_{\odot}$) showed much shorter plateau phases (up to 80 days). However, this was due to the sharp decrease in $T_{\rm eff}$ at early times relative to the 4 lower mass WDs, see Figure 3.1. The plateau phases were so short in these cases that the ejecta remained optically thick at the photoionization edge throughout and in our model these solutions would not have been self-consistent. For this reason we consider only the WDs in the mass range $0.60 - 1.10\ M_{\odot}$. Note that for lower ejecta masses and higher ejecta velocities expected of novae on higher-mass WDs, it is possible that the plateau phase would occur after the ejecta has become optically thin. In this work, though, we hold the ejecta parameters constant and thus do not consider the resulting inconsistent results from higher-mass WDs. Most of these results can be motivated and explained by our analytic work that derived equation (3.16), yielding the dependence of $t_{\rm iso}$ on the ejecta parameters and the average photoelectron energy. Such an understanding will be key to using these observed quantities to constrain either the WD mass or the ejecta properties.

To exhibit this physics, we explored the sensitivity of the plateau phase properties ($T_{\rm iso}$ and $t_{\rm iso}$) by varying $v_{\rm ej}$, $\Delta M_{\rm ej}$ and $E_{\rm ion}$ in simulations of a pure H ejecta photoionized by a 1.00 $M_{\odot}$ WD. We found that variations in ejecta properties ($v_{\rm ej}$ and $\Delta M_{\rm ej}$) affect

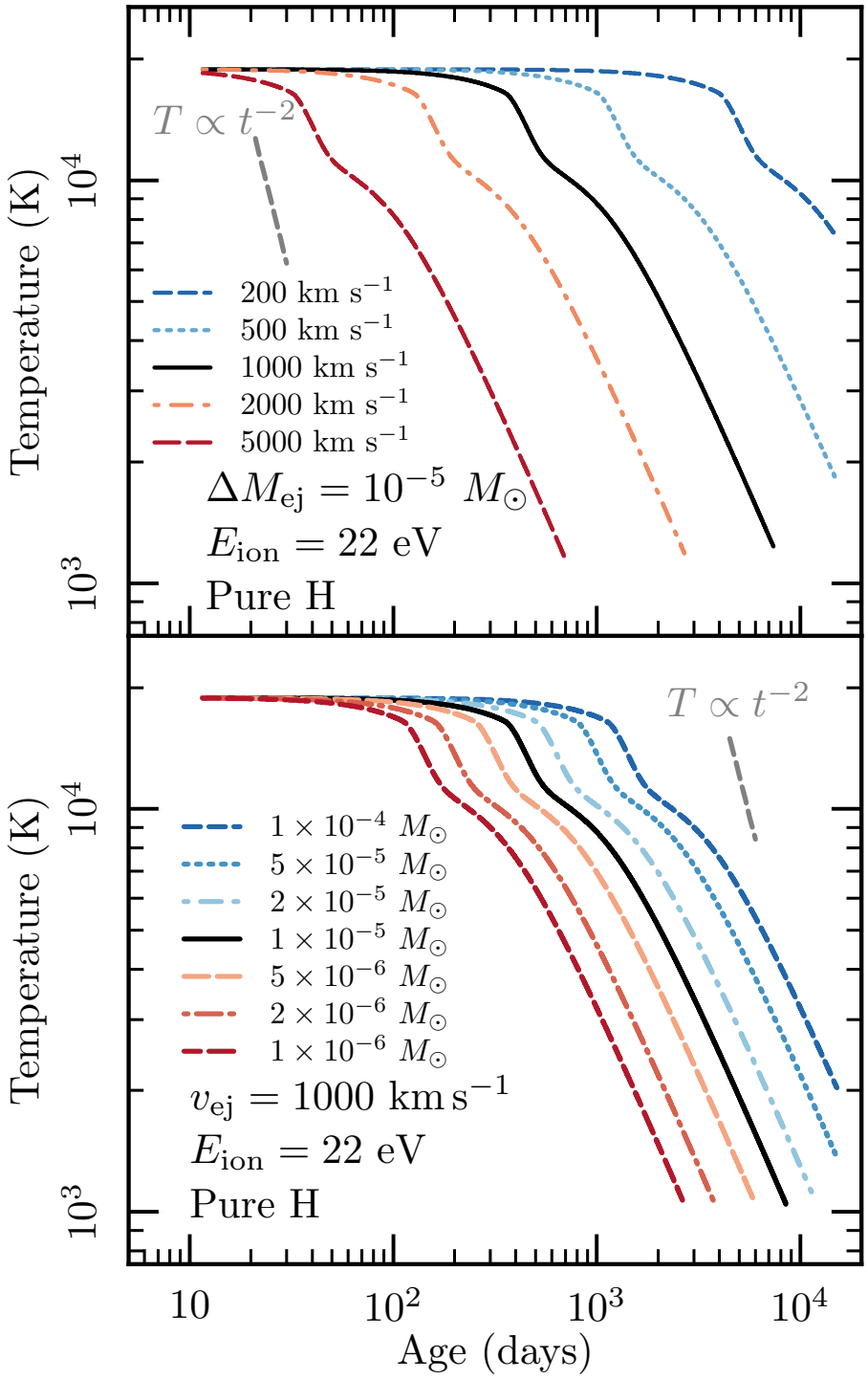

Figure 3.4 Ejecta temperature evolution for variations in ejecta velocity (top panel) and ejecta mass (bottom panel). Simulations carried out assuming pure H ejecta with constant $E_{\rm ion}$ and negligible contribution from collisional ionizations ($P_{\rm ci} = 0$). Unless otherwise indicated $\Delta M_{\rm ej} = 10^{-5}\ M_\odot$, $v_{\rm ej} = 10^3$ km s^{-1} and $E_{\rm ion} = 22$ eV.

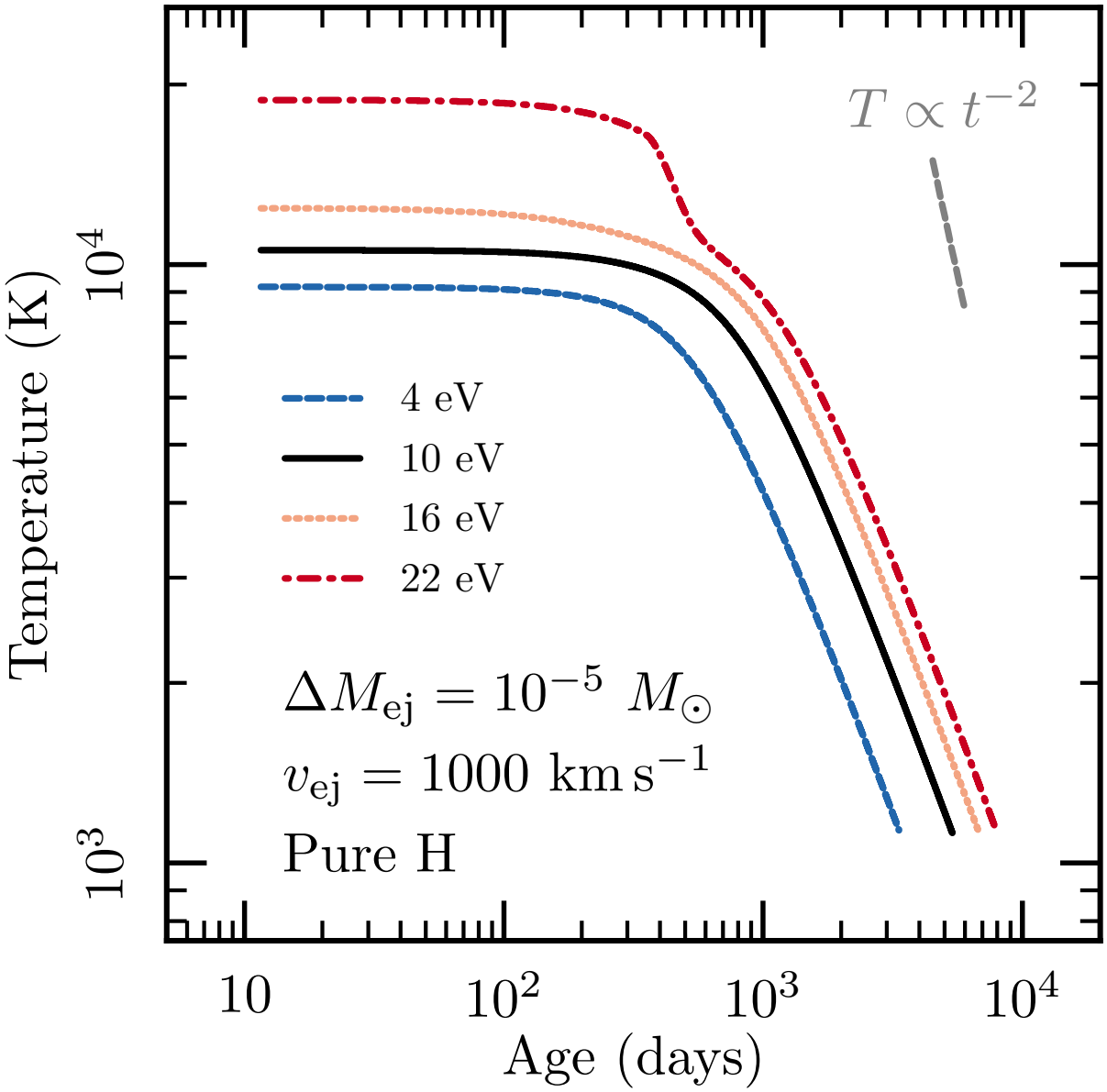

Figure 3.5 Ejecta temperature evolution for varying average energies of photoelectrons from 4 eV $\leq E_{\rm ion} \leq$ 22 eV. Simulations carried out assuming pure H ejecta with constant $E_{\rm ion}$ and negligible contribution from collisional ionizations ($P_{\rm ci} = 0$). Unless otherwise indicated $\Delta M_{\rm ej} = 10^{-5}\ M_\odot$, $v_{\rm ej} = 10^3$ km s^{-1}.

Table 3.2. Isothermal Evolution of Nova Ejecta[a]

WD Mass ($M_\odot$)	Average Temperature[b] (10^4 K)	$t_{\rm iso}$[c] (days)	$t_{\rm thin}$[d] (days)
0.60	2.2	229	36
0.80	3.2	155	33
1.00	4.7	152	47
1.10	4.5	217	74

[a]$\Delta M_{\rm ej} = 10^{-5}\ M_\odot;\ v_{\rm ej} = 10^3\ {\rm km\,s^{-1}}$

[b]Time-averaged temperature over isothermal phase

[c]Time after temperature drops 20% from early times.

[d]Duration of optically thick (to lyman-limit photons) phase

the duration of the plateau but do not alter its temperature. This is revealed in Figure 3.4 where the ejecta mass varies between $10^{-6}\ M_\odot \lesssim \Delta M_{\rm ej} \lesssim 10^{-4}\ M_\odot$ with velocities in range $10^2\ {\rm km\,s^{-1}} \leq v_{\rm ej} \leq 5 \times 10^3\ {\rm km\,s^{-1}}$. For calculating Figure 3.4 the $E_{\rm ion}$ was held constant in time for simplicity.

This highlights that the dynamic behavior of the ejecta is described by these two quantities, $v_{\rm ej}$ and $\Delta M_{\rm ej}$, that we can parametrize into a factor

$$\zeta \equiv \frac{\Delta M_{\rm ej}}{10^{-5}\ M_\odot} \left(\frac{v_{\rm ej}}{10^3\ {\rm km\,s^{-1}}}\right)^{-3}. \tag{3.18}$$

Using Equation (3.16), ζ can be inferred from the observed parameters $t_{\rm iso}$ and $T_{\rm iso}$ as

$$\zeta(t_{\rm iso},\ T_{\rm iso}) = \left(\frac{t_{\rm iso}}{250\ {\rm d}}\right)^2 \left(\frac{kT_{\rm iso}}{1\ {\rm eV}}\right) \left(\frac{E_{\rm ion}}{10\ {\rm eV}}\right)^{-1} \left(\frac{\alpha}{10^{-13}\ {\rm cm^3\,s^{-1}}}\right), \tag{3.19}$$

potentially yielding insights into the ejecta properties from observations. The average photo-electron energy $E_{\rm ion}$ depends on the WD's $T_{\rm eff}$ and is the main determinant of $T_{\rm iso}$,

as is evident in Figure 3.5. Hence, the plateau temperature is most sensitive to the WD $T_{\rm eff}$ (and hence WD mass).

The plateau phase space behavior of ζ is shown in Figure 3.6 with dashed lines of constant ζ. For nearly all cases, we see that $T_{\rm iso}$ is highly independent of the ejecta information, $v_{\rm ej}$ and $\Delta M_{\rm ej}$. This implies that changes made to the dynamic properties of the ejecta should be relatively insignificant for the temperature, making it a potentially clean diagnostic for WD mass. This also implies that changes to the ejecta profile (e.g. non-spherically symmetric ejections) or homogeneity would unlikely impact $T_{\rm iso}$.

The thermal evolution of the ejecta at late times is simple if the SSS phase has ended, as the ejecta undergoes an adiabatic temperature decline, and $T \propto t^{-2}$ thereafter. The recombination time is far longer than the age when $t > t_{\rm iso}$, so that this plasma would maintain itself in a highly ionized state even though photoionization has ended. Hence, it would still be a thermal bremsstrahlung radio emitter during the adiabatic decline. If the SSS remains on at $t > t_{\rm iso}$, we can still approximate the thermal evolution. In this limit, photoionization heating is still operative, so the temperature decline would not be as steep as the adiabatic relation. Rather, for the cases we considered here, the photoionization timescale is still much less than the age, $t_{\rm ion} \ll t$, so that the heating remains operative, and the required small neutral fraction is easily maintained. If we assume negligible radiative cooling, rather safe as $T < 10^4$ K, then equation (3.15) simplifies to an integrable form. If the ejecta temperature was T_0 at $t = t_0$, then its value

at a time $t > t_{\rm iso}$ is simply

$$\frac{T}{T_0} \approx \frac{t_0^2}{t^2} \exp\left(\frac{t_{\rm iso}^2}{t_0^2} - \frac{t_{\rm iso}^2}{t^2}\right), \tag{3.20}$$

exhibiting the less steep than adiabatic decline that is evident in nearly all our results. Differentiating between a decline from SSS shutoff versus onset of dominance of adiabatic expansion with an active photoionization source could be attempted by comparing $T(t)$ inferred from radio observations or nebular spectroscopy to $T \propto t^{-2}$ versus the more complicated relation of equation (3.20). Alternatively, a shut-off of the X-ray source could be confirmed by direct measurements like those of Schwarz et al. (2011) and Henze et al. (2011, 2014b). Equation (3.20) assumes a constant ionizing source, but the WD models used in Figure 3.3 are still increasing in effective temperature when adiabatic expansion takes over, so their decline is even less steep then equation (3.20) would indicate.

3.6 Conclusions

We have shown that the photoionizing emission from the hot white dwarf following a classical nova is adequate to explain the inferred ejecta temperatures $> 10^4$ K that persist for nearly a year after the optical outburst. For the typical WD mass, $\approx 0.8 M_\odot$, of a CNe this nearly isothermal phase lasts for about one year (see equation (3.16)) and has a temperature of $T \approx (2-3) \times 10^4$ K, in good agreement with many observed novae. Even when the SSS phase lasts for decades, the balance between heating and cooling eventually ends, and the ejecta transitions into a phase of temperature decline roughly approximated analytically by equation (3.20). If the SSS phase ends early, then the ejecta

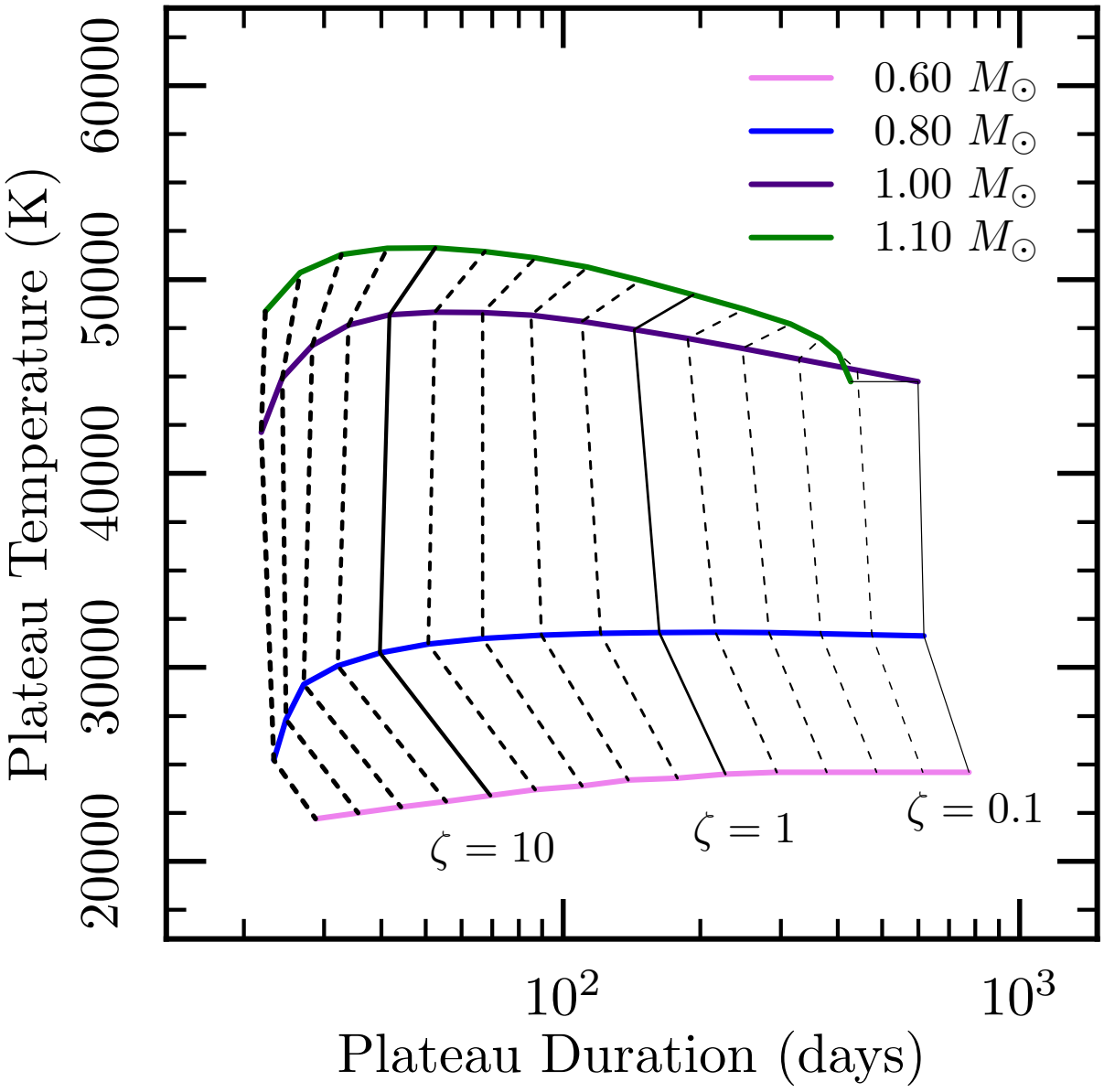

Figure 3.6 Characteristic plot of the plateau phase with dotted lines of constant ejecta parameter $\zeta = 10^{14} \times \frac{\Delta M_{\rm ej}}{v_{\rm ej}^3}$ spaced evenly in log space. A line of a particular color connects models of identical WD mass.

temperature would evolve adiabatically, as $T \propto t^{-2}$.

Though our preliminary calculations allow us to see the basics of how photoionization heating is balanced by cooling at early times, and how the heating is weak compared to adiabatic expansive effects at late times, work remains to realize the quantitative accuracy adequate to infer CNe ejecta properties or WD masses. We certainly identified a degeneracy in how the ejecta information ($\Delta M_{\rm ej}$ and $v_{\rm ej}$) affect the plateau phase duration, which should allow observers to make predictions about the properties of a given nova, complementing existing radio techniques (Seaquist & Palimaka, 1977; Hjellming et al., 1979; Heywood et al., 2005). For example, equation (3.19) makes possible the inference of an ejecta mass range based on the length of the isothermal temperature evolution inferred in the radio combined with the measured velocity of the ejecta and temperature.

However, specific events would be best modeled by a unique Cloudy simulation that reflects the known properties of the event as inferred from the optical, as well as the X-ray supersoft phase. That would also allow for inclusion of unusual abundances constrained from modeling the nebular spectroscopy as in Schwarz (2002), Vanlandingham et al. (2005), and Schwarz et al. (2007), which would in turn impact the mapping of the observed ejecta temperature to the WD mass. The ideal calcuation could use a more realistic ejecta density profile, like a Hubble flow (Seaquist & Palimaka, 1977) with an appropriate filling factor, though our efforts imply that the ejecta temperature is relatively independent of the specific density structure for the first year or so. We hope that the

expanded efforts with the Karl G. Jansky Very Large Array to monitor nearby galactic novae will enable a new era of quantitative analysis of the late time radio observations (Roy et al., 2012).

We thank Laura Chomiuk, Tommy Nelson, Jeno Sokoloski and Dean Townsley for discussions on the radio observations that inspired our efforts, and Orly Gnat for advice on using Cloudy. We also thank our referee for the paper this chapter is based on, Steve Shore, for his many helpful insights that improved the paper. This work was supported by the National Science Foundation under grants PHY 11-25915, AST 11-09174, and AST 12-05574. Most of the `MESA` simulations for this work were made possible by the Triton Resource, a high-performance research computing system operated by the San Diego Supercomputer Center at UC San Diego. We are also grateful to Bill Paxton for his continual development of `MESA`.

Chapter 4

Non-Radial Pulsations in Post-Outburst Novae

After an optical peak, a classical or recurrent nova settles into a brief (days to years) period of quasi-stable thermonuclear burning in a compact configuration nearly at the quiescent white dwarf (WD) radius. During this time, the underlying WD becomes visible as a strong emitter of supersoft X-rays. Observations during this phase have revealed oscillations in the X-ray emission with periods on the order of tens of seconds. A proposed explanation for the source of these oscillations are internal gravity waves excited by nuclear reactions at the base of the hydrogen-burning layer. In this work, we present the first models exhibiting unstable surface g-modes with periods similar to oscillation periods found in galactic novae. However, when comparing model mode periods of our models to the observed oscillations of several novae, we find that the modes

which are excited have periods shorter than that observed.

4.1 Introduction

A nova is an optical event caused by a thermonuclear runaway on the surface of a white dwarf (WD) (Gallagher & Starrfield, 1978). The thermonuclear runaway drives a rapid expansion of the WD where it shines brightly in the optical and loses much of its hydrogen-rich envelope via some combination of dynamical ejection, optically-thick winds, and/or binary interactions. Eventually enough mass is lost from the envelope so that the photospheric luminosity matches the nuclear burning luminosity and the WD radius recedes to a more compact configuration (Kato et al., 2014). Hydrogen burning does not cease, though, as a remnant envelope is slowly burned over days to decades. The hot and compact WD shines brightly in the UV and soft X-rays, appearing very similar to a persistent supersoft source (SSS) (Wolf et al., 2013). Dozens of SSSs from post-outburst novae are seen in M31 (Henze et al., 2010; Henze et al., 2011, 2014b; Orio, 2006; Orio et al., 2010) and the Milky Way (Schwarz et al., 2011, and references therein) every year.

Many, if not all, SSSs exhibit periodic oscillations in their X-ray light curve with periods ($P_{\rm osc}$) in the range of 10-100 seconds, whose precise origin is unclear (Ness et al., 2015, and references therein). Odendaal et al. (2014) argue that in the case of Cal 83, its 67 s period could be the rotational period of the WD. Ness et al. (2015) point out that the observed drift of the precise $P_{\rm osc}$ of ± 3 s can't be easily explained by accretion

spin-up or spin-down (due to high inertia of the WD) or by Doppler shifts of the emitting plasma due to the orbital motion. Furthermore, the $P_{\rm osc} = 67$ s of Cal 83 is the longest in the known sample, so other WDs would need to be rotating even more rapidly. While the rotation rates of accreting WDs are still not well understood, spectroscopic measurements to date do not point to rapid rotation (Sion, 1999; Szkody et al., 2012; Kupfer et al., 2016).

Rotation is thus not a very promising mechanism for explaining these oscillations, though it cannot be ruled out until an independent determination of the WD rotation period is obtained in an oscillating SSS. A more promising explanation first proposed by Drake et al. (2003) is that the oscillations are caused by non-radial surface g-modes excited by the ϵ-mechanism at the base of the hydrogen burning layer. However, the oscillations observed by Drake et al. (2003) for nova V1494 Aquilae were much longer. At $P_{\rm osc} \approx 2500$ s, these modes were more credibly explained as being driven by the κ-mechanism, where an ionization zone, rather than temperature-sensitive burning, is the source of an instability. Indeed, longer periods ($\sim 10 - 100$ minutes) have been observed in Cal 83 (Crampton et al., 1987; Schmidtke & Cowley, 2006) and nova V4743 Sgr (Ness et al., 2003), all consistent with oscilations most similar to ZZ Ceti, driven by the outermost convection zone. These longer-period oscillations are not the focus of this work.

The expected $P_{\rm osc}$ for ϵ-mechanism-driven g-modes was estimated in Ness et al. (2015) for a typical WD mass, envelope mass, and a constant-flux radiative envelope to be on the

order of 10 s, in great agreement with the observed periods. Their calculation, however, could not assess whether the mode would grow unstably or damp out.

The configuration of a thin hydrogen-burning radiative envelope on a WD is similar to early planetary nebulae nuclei, as explored by Kawaler (1988). With a detailed non-adiabatic pulsational analysis, Kawaler (1988) found that g-modes were indeed excited by the ϵ-mechanism. In a 0.618 $M_{\odot}$ planetary nebula nucleus model, higher-order modes with $P_{\rm osc} \approx 200$ s were excited first when the luminosity was around $\log L/L_{\odot} \approx 3.1$, and lower order modes with $P_{\rm osc} \approx 70$ s only being excited after the luminosity dropped to $\log L/L_{\odot} \approx 2.6$.

Encouraged by the promising results of Kawaler (1988) and Ness et al. (2015), we present in this chapter the first detailed non-adiabatic calculations of the unstable modes in post-outburst nova models using the open source stellar evolution code `MESA star` (rev. 9575; Paxton et al., 2011, 2013; Paxton et al., 2015) and the accompanying non-adiabatic stellar pulsation tool `GYRE` (Townsend & Teitler, 2013; Townsend et al., 2017). In §4.2 we explain the simulation details to obtain post-outburst nova models from `MESA star` for input into `GYRE`. Then in §4.3 we discuss mode propagation in our models and compare to previous simulations of oscillations in a planetary nebula nucleus. In §4.4, we present the periods and growth timescales of the modes calculated by `GYRE` from the nova models. We comment on how these modes compare to observed oscillation periods in §4.5 before summarizing in §4.6.

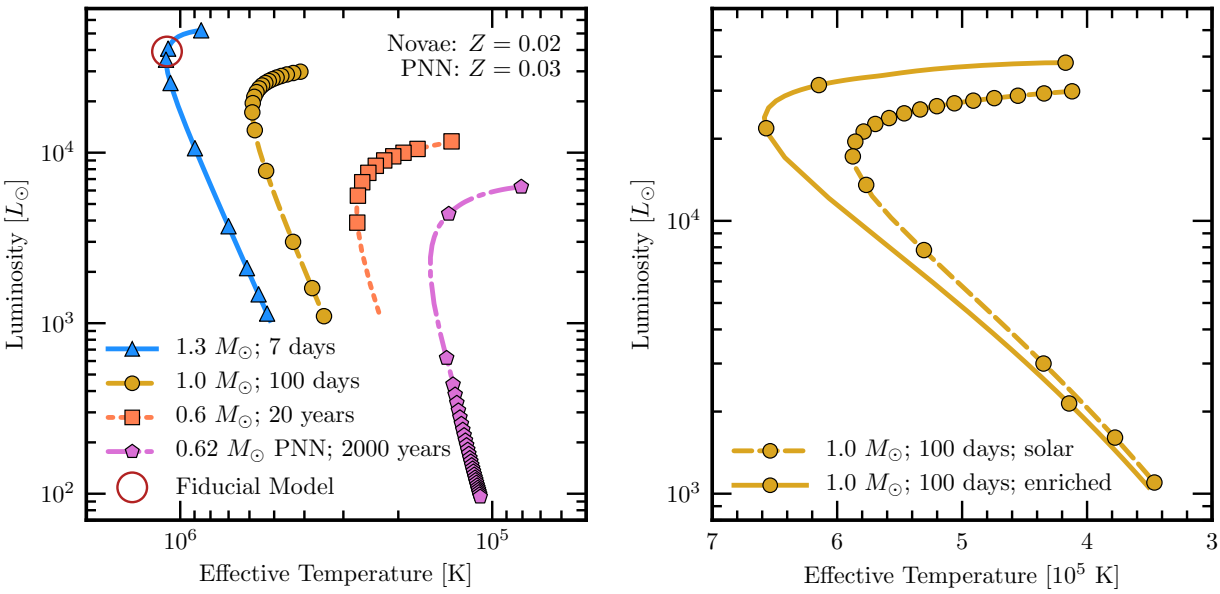

Figure 4.1 Evolution of all stellar models through the HR diagram. Different markers separate equal times of evolution. For example, between two yellow circles, 100 days have elapsed. **Left:** The three nova models that accrete solar composition material from the end of mass loss until their luminosities reach 10^3 $L_\odot$. Also shown is the $M = 0.6172$ $M_\odot$ planetary nebula nucleus introduced in Section 3. The maroon circle indicates a fiducial model of the 1.3 $M_\odot$ nova that we use as an example later in this chapter. **Right:** Comparison between the 1.0 $M_\odot$ nova models accreting solar composition and 25% core composition, 75% solar composition material. Again, markers along each track mark intervals of equal time.

4.2 Stellar Models

To generate models for use in pulsational analysis, we use the `MESA star` code. Specifically, we use an inlist based on the `nova` test case scenario, which in turn was based off of the nova calculations of Wolf et al. (2013). In these models, hydrogen-rich material is accreted at a rate of 10^{-9} $M_\odot$ yr^{-1}, which is a typical rate expected for cataclysmic variables (Townsley & Bildsten, 2005). Mass loss was handled by the built-in super-Eddington wind scheme described in Denissenkov et al. (2013) and Wolf et al. (2013), as well as a modified version of the built-in Roche lobe overflow mass loss scheme.

The precise nature of the mass loss is not important because mass is lost in some form until the hydrogen rich layer is reduced to the maximum mass that can sustain steady hydrogen burning in a compact form, which is a function primarily of the WD mass. At this point the WD shrinks and enters its post-outburst phase, as found by Wolf et al. (2013); Kato et al. (2014). The precise nature of the mass loss greatly affects properties of the nova at the time of optical peak, which we are not interested in. However, extra mass loss in excess of that required to reduce the hydrogen layer mass down to a stable burning mass can truncate the duration of the post-outburst phase. To create the most favorable conditions for mode excitation, we shut off mass loss or gain once the WD shrinks to radii similar to the reddest steady-state burners found by Wolf et al. (2013). In general, super Eddington winds dominate mass loss for novae on higher-mass WDs, and Roche lobe overflow dominates mass loss for novae on the lowest-mass WD.

These models are non-rotating, though rotationally-induced instabilities can be responsible for mixing between core and accreted material (MacDonald, 1983; Livio & Truran, 1987; Sparks & Kutter, 1987). Rotation may also affect the stability and structure of g-modes in a stellar model, so we discuss the effects of modest rotation on the expected modes in §4.3. No diffusion is allowed, though at this high of an accretion rate, its effects on metal enrichment of the thermonuclear runaway would not be very pronounced (Iben et al., 1992; Prialnik & Kovetz, 1995; Yaron et al., 2005). Finally, we do not allow for any convective undershoot during the thermonuclear runaway, which would also act to enhance the ejecta with metals (Casanova et al., 2010, 2011a,b; Glasner et al.,

2012). Mixing due to rotational instabilities, diffusion, and/or convective dredge-up are all causes of the metal enhancement of nova ejecta indicated by optical and UV spectra (Gehrz et al., 1998; Downen et al., 2013) as well as evidence for dust formation (Geisel et al., 1970; Ney & Hatfield, 1978; Gehrz et al., 1980).

Rather than considering how exactly to parameterize and combine the mixing effects of rotational, diffusion-induced, and turbulent instabilities, we instead include a model where the accreted material is 25 percent core material, where "core composition" is defined as the composition sampled where the helium mass fraction first drops below one percent. The remaining 75 percent of accreted material is solar composition.

All inlists, models, and additional code used to produce these models will be posted on the `MESA` users' repository, `mesastar.org`.

In total, four models were calculated: pure solar material accretion models for WD masses of 0.6 $M_\odot$, 1.0 $M_\odot$, and 1.3 $M_\odot$ and a metal-enriched accretion model for a 1.0 $M_\odot$ WD. The starting models were the endpoints of the similar nova simulations carried out by Wolf et al. (2013). The solar composition models were evolved through 2-3 nova cycles to erase initial conditions, while the metal-rich models were evolved through several flashes at an intermediate metallicity before being exposed to 25% enrichment to ease the transition. In all cases, model snapshots at every timestep after the end of mass loss to the end of the SSS phase were saved and form the basis for the analysis in the rest of this work.

Figure 4.1 shows the evolution of these nova models as well as a planetary nebula

nucleus model with $M = 0.617\ M_\odot$ introduced in §4.3 through the HR diagram. The general trends are that higher mass WDs and more metal-rich accretion give faster, bluer, and more luminous evolution. Note that the markers break the evolution into stretches of equal duration, but the actual timesteps taken in the evolution were much shorter, taking somewhere between 30 and 60 timesteps to get through the SSS phase. Also indicated in Figure 4.1 is the location of a fiducial model from the 1.3 $M_\odot$ simulation. We will refer to this model in subsequent sections as an example case for mode analysis.

4.3 Non-Radial Pulsation Analysis

With model snapshots of each of the novae throughout the SSS phase, we can use `GYRE` to determine their oscillation modes, focusing only on the $\ell = 1$ (dipole) modes. We begin by looking at the adiabatic properties of our fiducial model before delving into non-adiabatic analyses.

4.3.1 Adiabatic Pulsation

`GYRE` analyzes a stellar model to find its radial and non-radial pulsation modes. While a non-adiabatic calculation is required to determine which of these modes are excited in a given stellar model, we can learn a lot from simpler adiabatic calculations to see what modes are available for excitation.

We aim to explain the observed oscillations as g-modes in the outer atmosphere, so some g-modes in our model must "live" in the outermost parts of our model. The upper

panel of Figure 4.2 shows a propagation diagram of our fiducial 1.3 $M_\odot$ model during its SSS phase. Also indicated is the region of strong hydrogen burning, where we expect mode driving to occur.

After using `GYRE` to search for the eigenmodes of this model, we indeed find g-modes that live in the outer atmosphere with periods on the order of a few to tens of seconds. Horizontal displacement eigenfunctions for the g-modes with radial orders $n = -1, -2,$ and -4 (in the Eckart-Osaki-Scuflaire classification scheme, as modified by Takata (2006)) are shown in the middle panel of Figure 4.2 with their periods indicated as horizontal lines spanning their allowed propagation regions (where their frequencies lie below both the Lamb and Brunt Väisälä frequencies) in the upper panel. The bottom panel shows the distributions of inertia in these modes (normalized so they integrate to unity), confirming that the modes indeed exist only within their allowed propagation regions. We see that the lowest order mode lives mostly in the burning region and the lower-density region above it. This makes this mode comparatively more easy to excite than the other two, which have much of their energy in the higher-density helium-rich region below.

These are merely the modes in which the star is able to pulsate. To excite one, a driving force must do work on the mode, and a non-adiabatic caluclation is required to find such unstable modes. We discuss the relevant driving force and our non-adiabatic calculations next.

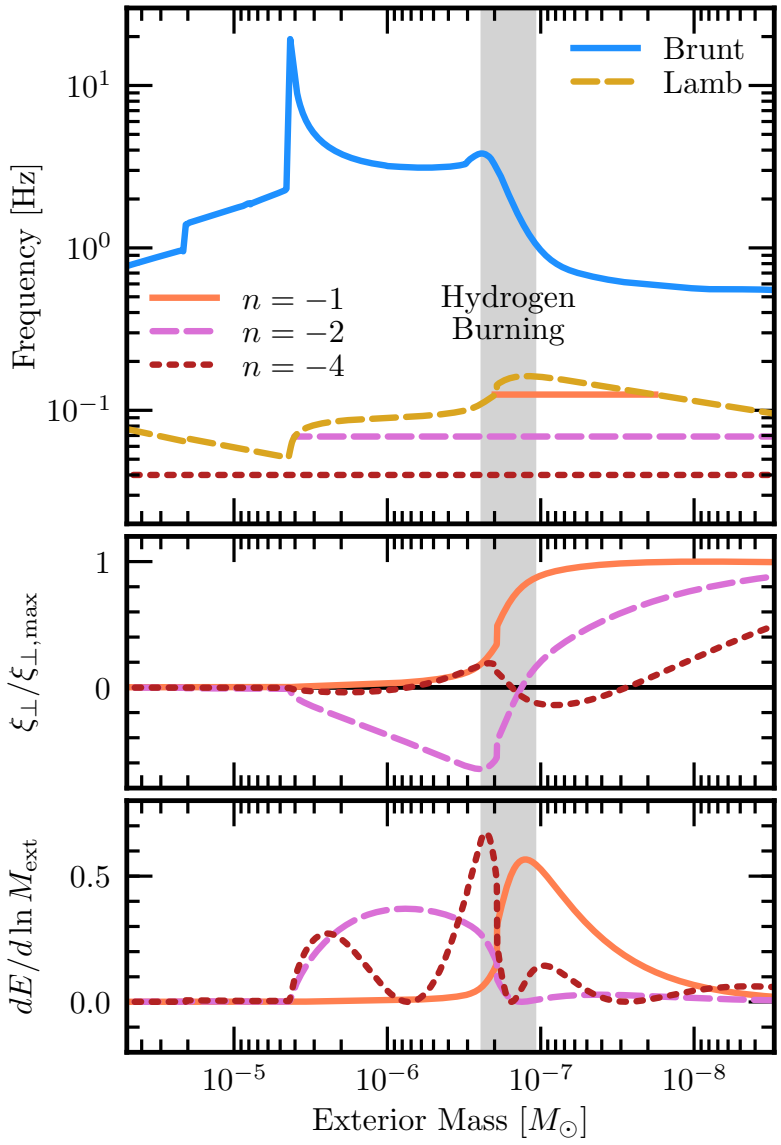

Figure 4.2 Profiles of the fiducial 1.3 $M_\odot$ model introduced in Figure 4.1. **Top panel**: Propagation diagram of the outermost 10^{-4} $M_\odot$. The shaded area indicates the region over which 80% of the stellar luminosity is generated by CNO burning. Regions where the $n = -1, -2$ and -4 modes can propagate are plotted as horizontal lines at their respective frequencies. **Middle panel**: Eigenfunctions for the same three modes. Horizontal displacement dominates over radial displacement for these modes, so only the horizontal displacement is shown, normalized to a maximum of unity. **Bottom panel**: Mode inertia of these same modes, normalized so the total inertia is unity. Since the abscissa is shown logarithmically, the plotted value is actually the derivative of the inertia with respect to $\ln[M(R) - M(r)] = \ln M_{\rm ext}$ so that equal areas under the curve indicate equal mode inertias.

4.3.2 Non-adiabatic Pulsations and the ϵ-Mechanism

The driving force relevant to novae in the SSS phase as well as planetary nebula nuclei is the ϵ-mechanism. In the ϵ-mechanism, the nuclear energy generation rate per unit mass ϵ is enhanced during a compression and attenuated during rarefaction. In this way, heat is added near the maximum temperatre of the cycle and removed near the minimum temperature, creating a heat engine that converts thermal energy into work (Eddington, 1926).

This phenomenon requires temperature sensitivity to produce feedback between the pulsation and ϵ. For temperatures of interest to this work ($T \lesssim 10^8$ K), the CNO cycle is not yet beta-limited, and we still have $\epsilon \propto T^{9-14}$, so the ϵ-mechanism can be relevant.

There is, however, a minor complication. With periods on the order of tens of seconds, oscillations in temperature and density occur on the same timescales as the lifetimes of isotopes in the CNO cycle (Kawaler, 1988). This leads to lags between the phases of maximum temperature/density and the phase of maximum energy generation. As a result, the temperature and density sensitivities of the nuclear energy generation rate will differ from those in a non-oscillating system at the same average temperature and pressure.

The method for computing corrected derivatives of the energy generation rate were presented in Kawaler (1988), but since that work examined oscillations in a planetary nebula nucleus, which burns at a lower temperature than our nova models, an assumption in that work does not apply here. The details of how we calculate the derivatives and

include them in GYRE are in Appendix A.

Before studying the modes excited in the nova models, we first analyze a planetary nebula nucleus model similar to that of Kawaler (1988) to verify that we obtain a similar set of excited modes.

4.3.3 Planetary Nebula Nucleus

The planetary nebula nucleus (PNN) model from Kawaler (1988) was created by first evolving a star with a ZAMS mass of a 3.0 $M_{\odot}$ star with a metallicity of $Z = 0.03$ to the AGB and then stripping its envelope gradually away.

The MESA test suite includes a test case, make_co_wd, which evolves a star to the AGB and through one thermal pulse from the helium burning shell, and then greatly increases the efficiency of AGB winds to reveal the WD. We used this test case as a basis and changed three controls to create our PNN model. First, we set the metallicity to 0.03 instead of the test case's default value of 0.02. Secondly, we evolve the model from the pre-main sequence (rather than interpolating from a default suite of models) due to the specific metallicity. Finally, we adusted the initial mass to 3.30 $M_{\odot}$ so that the final mass of $M = 0.6172\ M_{\odot}$) closely resembled the mass of the PNN in Kawaler (1988) of $M = 0.6185\ M_{\odot}$.

Once the model reached an effective temperature greater than 10,000 K, we changed its nuclear network to match the network used in the nova simulations (cno_extras.net). At $T_{\rm eff} = 60,000$ K, we halted the enhanced mass loss that accelerated the thermal pulse

phase in order to resume normal PNN evolution. We then saved profiles for pulsational analysis at every timestep once $T_{\rm eff}$ exceeded 80,000 K, and we halted evolution when the luminosity dropped below 100 $L_{\odot}$.

The evolution of the model's g-mode properties through its PNN phase is shown in Figure 4.3 for six lowest-order modes. The first mode to be excited was a g-mode with radial order $n = -6$. The period of this mode stayed consistently near 150 s and its growth time stayed in the range of hundreds to thousands of years (still shorter than the hydrogen-burning lifetime of the PNN). The period agrees well with the $k = 6$ column of Table 3 in Kawaler (1988), but we find growth timescales that are longer by one or more orders of magnitude with the mode being stabilized sooner than in Kawaler (1988).

Other modes have matching or very nearly matching periods, but the growth times we find are typically much longer than those of Kawaler (1988). In addition to the modes shown in Figure 4.3, we see the $n = -7$ and $n = -8$ modes excited, but not the $n = -9$ mode as in Kawaler (1988), consistent with the general trend of higher stability in our models.

We searched for modes both while accounting for the phase lags in the energy generation rate and while not accounting for them. In both PNN and nova models, adding in the effects of phase lags increases growth times and stabilizes modes that would otherwise be unstable. This is because the phase of peak heat injection is moved away from the phase of peak temperature/density, weakening the heat engine set up by the ϵ-mechanism.

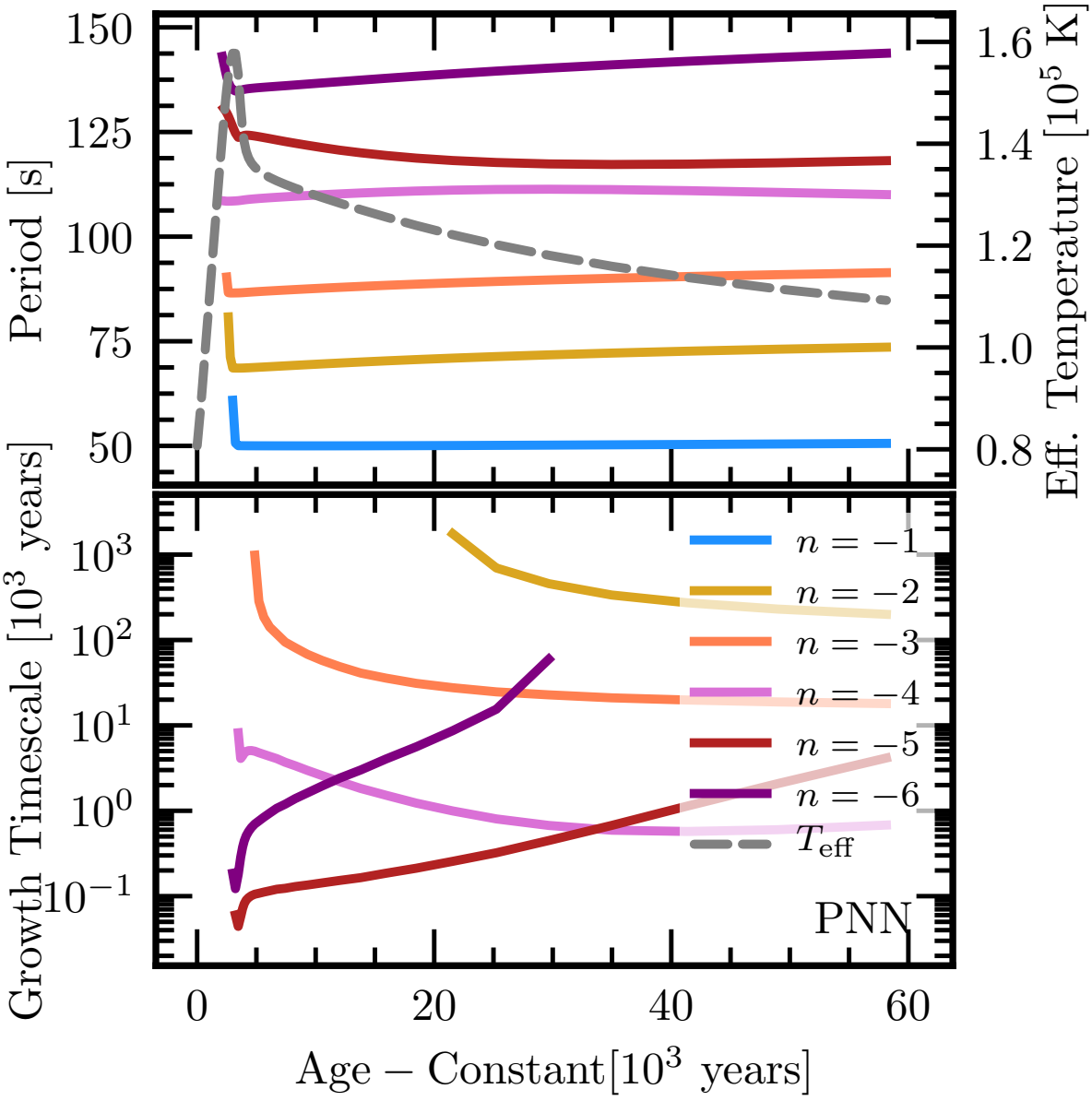

Figure 4.3 Evolution of $\ell = 1$ g-modes in the planetary nebula nucleus model through the depletion of its hydrogen envelope. The top panel shows how the periods of the six lowest-order g-modes change in time. The effective temperature is also shown for comparison to evolution in the HR diagram. The bottom panel shows the evolution of the growth timescale for each mode if it is unstable.

4.4 Supersoft Nova Modes

Figure 4.4 shows the evolution of the periods of low-order g-modes in the post-outburst nova models as well as the evolution of these modes' growth timescales. The effective temperature evolution is also shown in these figures, revealing that the most rapid excitation occurs in the approach to the peak effective temperature at the "knee" of the HR diagram shown in Figure 4.1.

We find unstable modes excited on timescales shorter than the supersoft phase lifetime in all four nova models. Excited modes had periods as short as 7 seconds in the 1.3 $M_\odot$ model and as long as 80 seconds for the 0.6 $M_\odot$ model. Unlike the PNN model, only lower-order modes were excited. The $n = -1$ and $n = -2$ modes are excited at some point in every model, while the $n = -3$ mode is excited in the 1.3 $M_\odot$ and enriched 1.0 $M_\odot$ models only. In the 1.0 $M_\odot$ and 1.3 $M_\odot$ models, only the $n = -1$ mode exhibits short enough growth timescales for the mode to grow by several e-foldings before it is stabilized, but the 0.6 $M_\odot$ model actually excites its $n = -2$ mode earlier and more rapidly than the $n = -1$ mode.

The general trend is that more massive WDs exhibit shorter periods and shorter growth times. We find that metal enrichment has little effect on the mode periods, but it significantly reduces growth timescales and the duration of the SSS phase.

The models made in `MESA star` are non-rotating, but we can probe the effects of rotation on the mode periods and growth timescales by using the traditional approximation (Bildsten et al., 1996; Townsend, 2005).

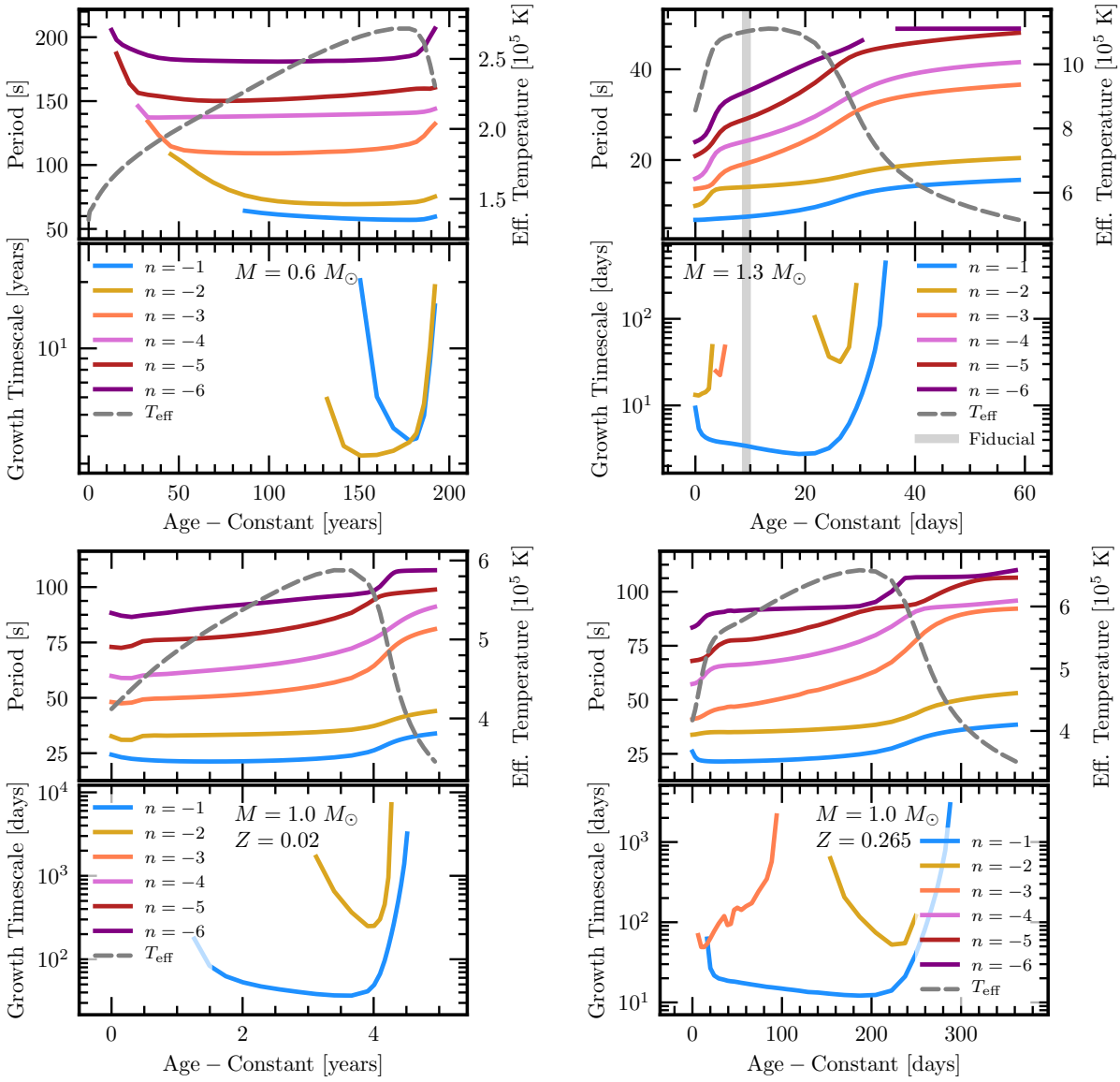

Figure 4.4 Evolution of the $\ell = 1$ g-modes of each post-outburst nova model (masses and compositions indicated in each plot). Similar to Figure 4.3, the top panels show mode periods and effective temperatures while the bottom panels show growth timescales. Points in a top panel represent unstable modes only if an accompanying point at the same age and mode order appears in the lower panel. A gray vertical band in the 1.3 $M_\odot$ plot indicates from where the fiducial model referenced elsewhere in this work is taken.

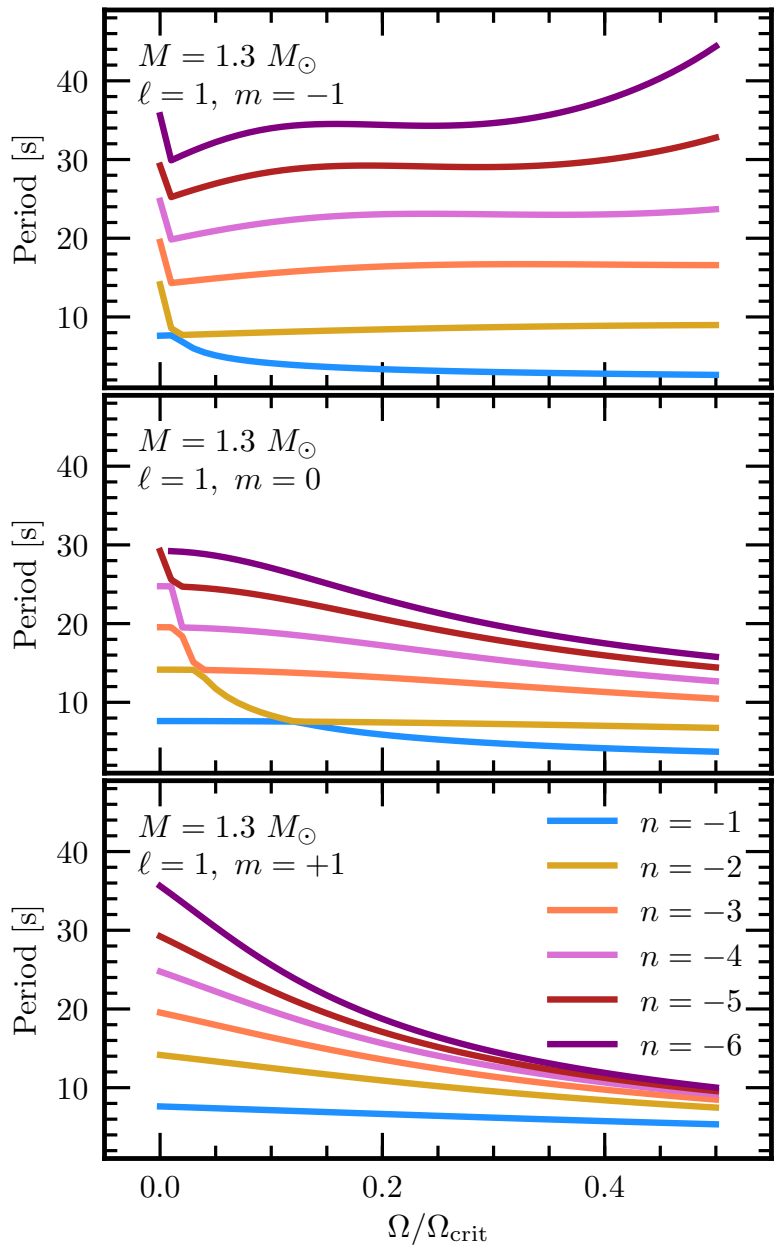

Figure 4.5 Dependence of the mode periods on the rotation rate as a fraction of the critical rotation rate for the $m = -1$ (top), $m = 0$ (middle), and $m = +1$ (bottom) modes in our 1.3 $M_\odot$ fiducial model. At any given rotation rate, the mode with a period of 8–9 seconds is excited with a growth timescale of around 2.5 days. For the $m = +1$ case, this is always the $n = -1$ mode, but due to avoided crossings, the excited mode switches to the $n = -2$ mode in the $m = -1$ and $m = 0$ cases at a modest fraction of the Keplerian rotation frequency. No other modes are ever excited on timescales shorter than or comparable to the SSS lifetime.

We investigated how the periods and growth times for $\ell = 1$ modes changed in response to varying the rotation rate Ω in our fiducial 1.3 $M_\odot$ model. Figure 4.5 shows how periods of $\ell = 1$ modes are affected by rotation up to an Ω of half of the critical rotation rate $\Omega_{\rm crit} = \sqrt{8GM/(27R^3)}$. We now summarize the results.

Higher-order zonal ($m = 0$) and prograde ($m = 1$) modes' periods decreased modestly with increasing Ω, but for higher-order retrograde ($m = -1$) modes, periods increased modestly after an initial drop due to a series of avoided crossings. However, across all Ω's, there was only ever one mode excited on timescales comparable to or shorter than the nova evolution timescale. The period of this mode is 8–9 seconds and its growth timescale is 2.5 days, in great agreement with the non-rotating results shown in Figure 4.4. Due to the avoided crossings, this mode changes in radial order from $n = -1$ to $n = -2$ at about 2% and 12% of $\Omega_{\rm crit}$ for the $m = -1$ and $m = 0$ cases, respectively. With no significant change in the periods of the excited mode, we expect no observable effect from rotation on these oscillations other than incidental effects rotation may have on the accretion and runaway processes.

4.5 Comparison to Observation

The goal of this work was to explain the oscillations in post-outburst novae and persistent supersoft sources described in Ness et al. (2015) and references therein. We've demonstrated that the ϵ-mechanism is indeed an effective means to excite g-modes with periods similar to those in observed SSSs.

However, we have only demonstrated that these modes are unstable in the linear regime. We cannot predict amplitudes for these oscillations to construct a X-ray light curve for comparison. A more complex non-linear calculation would be required to make such a robust prediction.

Fortunately, our work has confirmed, as expected, that the periods are most sensitive to the mass of the underlying WD rather than composition or rotation. Thus, a nova with a known WD mass and observed oscillations would provide a means to check the efficacy of g-modes as a source for these oscillations. We now review the oscillating post-outburst novae presented in Ness et al. (2015) and compare them to our models.

4.5.1 RS Ophiuchi

RS Ophiuchi (RS Oph) is a recurrent nova with recurrence times as short as nine years. From spectral measurements, Brandi et al. (2009) find a best orbital solution for a WD with a mass in the range of $1.2 - 1.4\ M_{\odot}$. From the recurrence time alone, models from Wolf et al. (2013) limit the WD mass to $M > 1.1\ M_{\odot}$, while the effective temperature and duration are most consistent with models with a mass near $1.3\ M_{\odot}$.

However, according to Ness et al. (2015), RS Oph has oscillations with a period of 35 seconds, which is significantly longer than the $\approx 6 - 10$ second periods seen in the $n = -1$ mode of our $1.3\ M_{\odot}$ model. Even giving a generously low mass of $1.0\ M_{\odot}$ would require exciting the mode only at late times when it is already stabilizing or by tapping into the $n = -2$ mode during the brief duration that it is unstable.

4.5.2 KT Eridani

KT Eridani (KT Eri) is a nova that also exhibited oscillations with periods of roughly 35 s at multiple times in its supersoft evolution (Beardmore et al., 2010; Ness et al., 2015). Jurdana-Šepić et al. (2012) estimate from the supersoft turn-on time and possible presence of neon enrichment, the mass of the underlying white dwarf is $1.1 M_{\odot} \leq M_{\rm WD} \leq 1.3\ M_{\odot}$. With a turn-off time of around 300 days (Schwarz et al., 2011), models from Wolf et al. (2013) are consistent with this contraint. Similar to RS Oph, the lowest order (and most easily excited) modes from the 1.0 and 1.3 $M_{\odot}$ models still cannot explain the observed oscillations, but second or third order modes are not out of the question if they could be excited.

4.5.3 V339 Delphini

V339 Delphini (V339 Del) was a nova with an observed 54 s oscillation (Beardmore et al., 2013; Ness et al., 2013). Shore et al. (2016) provide an estimate for the ejecta mass of V339 Del of $2 - 3 \times 10^{-5}\ M_{\odot}$. With this and its SSS turn-off time of 150-200 days, V339 Del is consistent with a WD mass of $M_{\rm WD} \approx 1.0 - 1.1\ M_{\odot}$ (Wolf et al., 2013). Again returning to our 1.0 $M_{\odot}$ models, we must rely on even higher order $n < -2$ to explain the observed oscillations. The $n = -3$ mode is unexcited in the solar composition model, and in the metal-enriched model, it is only marginally unstable in that its growth timescale is comparable to the duration in which it is unstable. Even then the $n = -3$ mode has a period that is slightly too short during this phase, but higher-order modes are never

excited at all. It is difficult to explain the oscillations in V339 Del with our models.

4.5.4 LMC 2009a

LMC 2009a is a recurrent nova, having first been detected in outburst in 1971. From its recurrence time as well as the SSS duration and temperature of the 2009 outburst, Bode et al. (2016) estimate the mass of the underlying WD to be $M_{\rm WD} \approx 1.1\ M_\odot - 1.3\ M_\odot$. The oscillations during the SSS phase reported in Ness et al. (2014, 2015); Bode et al. (2016) had a period of 33 seconds. With a similar period and mass estimate to KT Eri, the g-mode explanation of these oscillations is similarly tenuous.

Our models show that metal enrichment does not change mode periods substantially, and even relatively rapid rotation cannot greatly affect the periods of excited modes. Rather, it seems that without some more exotic physics that can couple to higher-order modes, the g-modes we see in our model cannot adequately explain the oscillations observed in the novae detailed in Ness et al. (2015).

4.6 Conclusions

We have used `MESA` models to confirm the earlier work of Kawaler (1988) on planetary nebula nuclei. We then extended that work to see what, if any, modes are excited in post-outburst novae via the ϵ-mechanicsm. In all our models, we found unstable modes with growth timescales shorter than the lifetime of the post-outburst supersoft phase.

While metal-enhancement of the WD envelope did expedite the evolution through the

post-outburst phase and the growth of any excited modes, it did not greatly influence the periods of these modes. Similarly, rotation only affected the periods of higher-order modes that were not excited, so it is unlikely to have a strong effect on any oscillations this mechanism might produce.

Finally, we compared our results to the observed oscillations of several novae. Broadly, the excited modes we find for comparable nova models have periods that are too short to explain the observed ocsillations, and neither metal enhancement nor rotation are sufficient to excite higher-order modes or increase an excited mode's period.

This work was supported by the National Science Foundation under grants PHY 11-25915, ACI 13-39581, ACI 13-39606, and ACI 13-16-63688 as well as by NASA under TCAN grant number NNX14AB53G. We thank Steve Kawaler for helpful discussions regarding his previous work on planetary nebula nuclei.

Chapter 5

Open Questions and Next Steps

The preceding work prompts several prospective new lines of research. We outline two such topics here. First is the long-term evolution of rapidly-accreting WDs, which is of high interest given their status as candidates for type Ia supernovae. Another obvious question stemming from chapter 4 is the possible explanation of oscillations seen in post-outburst novae as convectively-excited g-modes that live deeper in the star than the modes examined in chapter 4. We conclude this dissertation with some thoughts and initial analysis of these two questions.

5.1 Fates of Rapidly Accreting White Dwarfs

Rapidly accreting WDs ($\dot{M} \gtrsim 10^{-8}\ M_\odot\ \mathrm{yr}^{-1}$) have been touted as promising candidates for type Ia since they offer a way to grow the mass of a C/O WD from $M_{\mathrm{WD}} \approx 1.0\ M_\odot$ to the Chandrasekhar mass $M_{\mathrm{Ch}} \approx 1.38\ M_\odot$. Classical novae resulting from slower accretion

rates are thought to lose mass due to the combination of mixing with core material and powerful mass loss (Prialnik & Kovetz, 1995). At higher accretion rates, novae occur on short enough recurrence times that diffusion is not able to mix in core material, and the runaways are mild enough that turbulent mixing at the base of the convection zone is not as effective in dredging up core material. Similarly, mass loss is not as powerful for these milder novae, and as a result, such nova cycles result in a net gain of mass. In the case of steady and stable burning, there is trivially net mass growth.

Crucially, this scenario for type Ia supernovae requires growth of the *carbon/oxygen* core. Nova cycles and steady burning result in growth of the *helium* layer. Inevitably, the growing helium layer will ignite, driving its own nova-like transient that may very well eject all the mass gained over previous hydrogen novae and/or steady burning, scuttling the whole process. After this helium flash, stable helium burning analagous to stable hydrogen burning would be able to grow the core mass, but as figure 5.1 shows, there is no accretion rate where both hydrogen and helium can stably *and steadily* burn.

Since the helium can only be burned via intermittent shell flashes and we don't believe that C/O WDs are born more massive than $M_{\rm WD} \approx 1.0\ M_{\odot}$, the main question then becomes: do helium flashes on a $M_{\rm WD} \approx 1.0\ M_{\odot}$ WD lead to long-term growth of $M_{\rm WD}$? Also, if $M_{\rm WD}$ *can* grow, can it do so in a time short enough to occur within the rapid mass-transferring phase of the binary? What would these helium flashes look like, and could the long-lived supersoft phases after them be a significant contaminant in the known sample of supersoft X-ray sources?

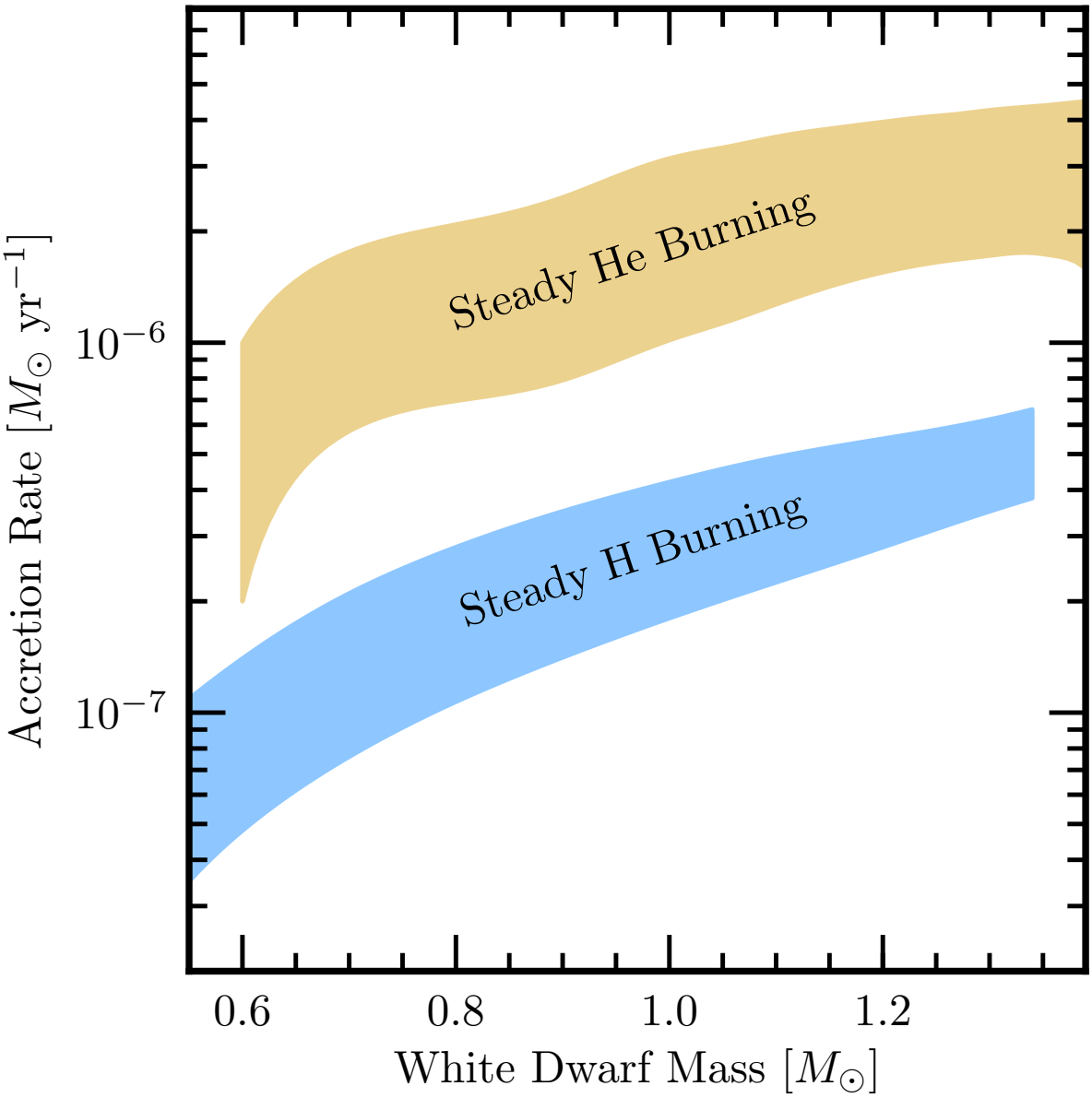

Figure 5.1 Regions where stable and steady burning of H and He are possible on a non-rotation WD. The steady H-burning region comes from Wolf et al. (2013) and the steady He-burning region comes from simulations from Brooks et al. (2016). The H-burning region assumes accretion of solar composition material, while the He-burning region assumes accretion of hydrogen-deficient material with $Z = 0.02$, which is consistent with the ash from steady hydrogen burning of solar material. Since the two regions do not overlap, there are no accretion rates that support simultaneous steady and stable burning of hydrogn and helium.

We discuss these questions now, first looking at the work others have done.

5.1.1 Previous Work

As discussed in chapter 2, Cassisi et al. (1998) and Piersanti et al. (1999) studied the rapid accretion of hydrogen onto low-mass WDs. While they found steady hydrogen burning and an eventual helium flash, they could not compute through it since the convection from the helium runaway reached the hydrogen, bringing potent nuclear fuel to the hot depths of the helium runaway. They posited that the resulting flash would become dynamical and eject most, if not all of the accreted material.

Yoon et al. (2004a) were able to nearly stabilize helium burning in a rapidly accreting WD model by tracking the transport of angular momentum. By accreting matter with Keplerian angular momentum (as is expected from the inner accretion disk), the H-rich material is spun up relative to the core. A shear layer develops at the core-envelope interface, driving strong shear heating, which acts to stabilize helium burning by providing an extra source of flux at the base. However, this work did not account for magnetic effects on angular momentum transport like the Spruit-Tayler dynamo, which act to quickly enforce rigid rotation (Piro, 2008). Without the strong shear layer, the stabilization vanishes and the helium shell would remain thermally unstable.

Another possible amelioration of this issue came from Hillman et al. (2016). In their work, they simulated rapid hydrogen accretion to get an average effective accretion rate of He at different initial masses of the WD, effectively determining the mass growth efficiency

at high accretion rates. They then simulated accreting pure helium at this effective rate since following many hydrogen flashes was computationally expensive. They found that while the first several helium flashes indeed caused a net mass loss over the entire cycle, these flashes heated up the WD core and caused subsequent flashes to become less violent, eventually leading to net mass gain in a non-rotating WD model.

There are two shortcomings of this work, though. First, the only mixing mechanism allowed between flashes is elemental diffusion. Convective overshoot (Glasner & Livne, 1995; Glasner et al., 1997, 2005, 2007; Glasner et al., 2012; Kercek et al., 1998, 1999; Rosner et al., 2001; Alexakis et al., 2004; Casanova et al., 2010, 2011a,b) and rotationally-induced instabilities (Durisen, 1977; Kippenhahn & Thomas, 1978; MacDonald, 1983; Livio & Truran, 1987; Kutter & Sparks, 1987; Sparks & Kutter, 1987) also cause mixing between accreted and core material that contribute to core erosion, even after the core is heated substantially. Supersolar metal enrichment is ubiquitous in classical and recurrent novae, as indicated by UV, optical, and IR spectroscopy (Downen et al., 2013; Gehrz et al., 1998) and photometry consistent with dust formation (Geisel et al., 1970; Ney & Hatfield, 1978; Gehrz et al., 1980). Whatever mechanism is responsible for the metal enrichment is capable of reaching through the helium layer and to the core, making long-term growth of the helium layer through hydrogen flashes unlikely.

A way around this problem would be stable burning, which introduces the second issue with the work of Hillman et al. (2016). Their stellar models cannot reproduce the steady burning observed with `MESA` and other codes (see chapter 2). Even so, it's still

possible that non-diffusive mixing mechanisms could cause the removal of more mass than is accreted in one helium flash cycle. The results of Hillman et al. (2016) are promising, but they need to be verified.

Finally, another solution has been proposed by Hachisu et al. (1996), where the accretion rate is above the stable burning regime. In this case, the WD swells up in response to the rapid accretion rate and enters a wind phase according to the wind prescription of Kato & Hachisu (1994). The helium flash then happens within a large, extended envelope. Hachisu et al. (1996) argue that mass loss from such helium flashes is minimal by pointing to the results of Kato et al. (1989), which detailed mass loss from helium novae, which should be similar to these helium flashes. However, Kato et al. (1989) only looked at helium novae on a 1.3 $M_{\odot}$ WD, where mass loss should trivially be weaker than at lower masses. It's also unclear if any mixing mechanisms are used in their work, so while not ruled out, this scenario does not point to definitive mass growth from $M_{\rm WD} \approx 1.0 M_{\odot}$.

5.1.2 Next Steps

To properly tackle these questions, we need to address several issues. First we need a realistic mass transfer scenario that can support high enough $\dot{M}$'s for a long enough time to grow $M_{\rm WD}$ from 1.0 $M_{\odot}$ to 1.38 $M_{\rm odot}$. Secondly, we need a better understanding of (or a least constraints on) mixing at both the H-He and He-C/O interfaces during accretion and thermonuclear runaways.

As preliminary work, we have already generated a plausible mass transfer history

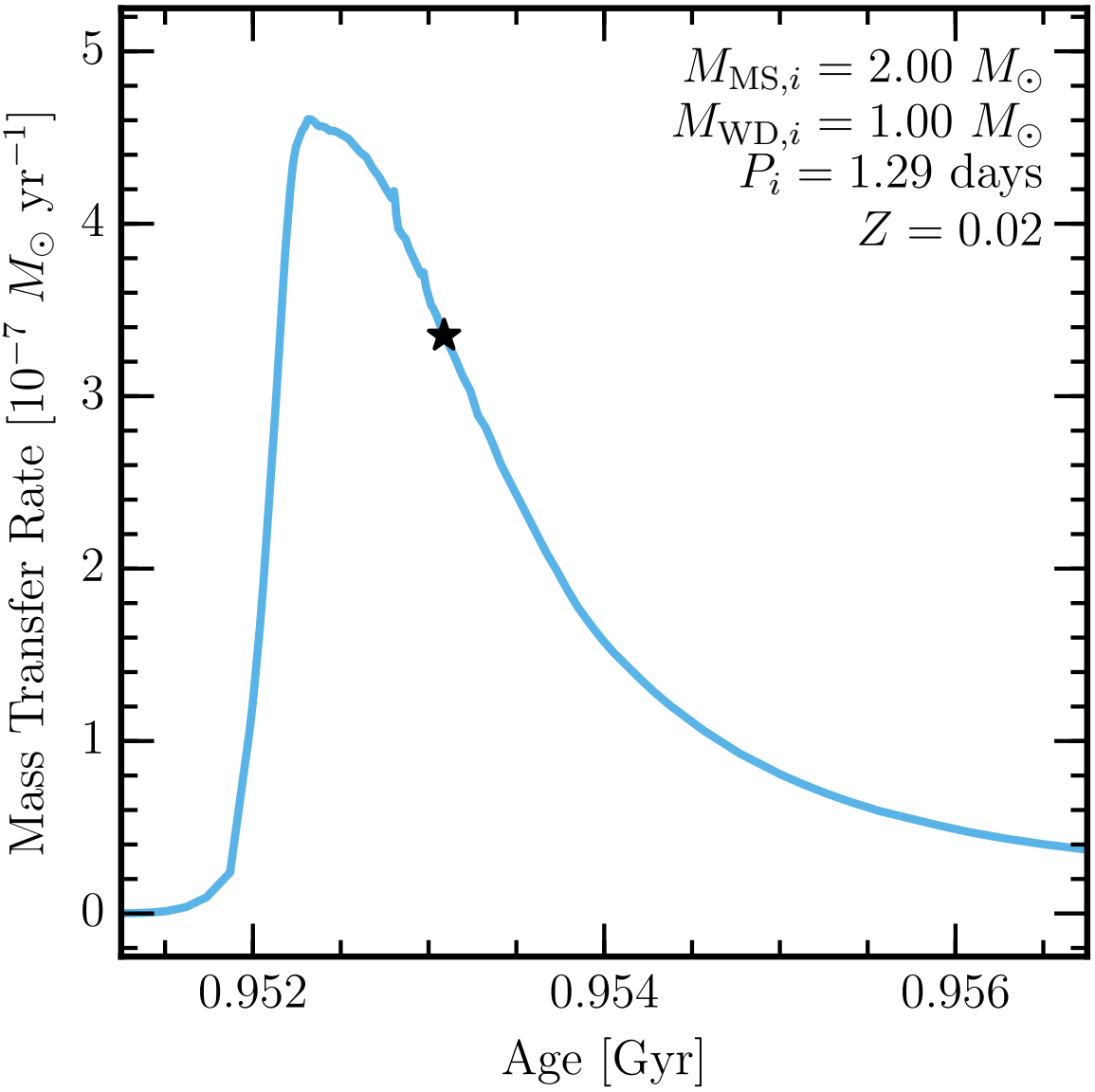

Figure 5.2 Evolution of the mass transfer rate from the donor to the WD in the system described in the text. The star represents where, under simple mass retention assumptions, $M_{\mathrm{WD}} = M_{\mathrm{Ch}}$.

between a 2.0 $M_{\odot}$ star as it leaves the main sequence transferring matter on a thermal timescale to a 1.0 $M_{\odot}$ WD with an initial binary period of 1.29 days. The evolution of the mass transfer rate is shown in Figure 5.2. This simulation was a successful comparison to the work of Langer et al. (2000), confirming their work as well as the capabilities of `MESA` to simulate the binary systems needed for this work.

Refinements to the mixing mechanisms during accretion and runaway are still needed, though. The treatment of diffusion in degenerate matter is under active development in `MESA`. Rotational mixing mechanisms are implemented in `MESA`, including the Spruit-Tayler Dynamo, which is expected to enforce nearly rigid rotation, simplifying previous difficulties associated with strong shear in numerical models.

Convective overshoot is still a process that is calibrated empirically on a case-by-case basis. Efforts like those of Arnett et al. (2015) hope to naturally include effects like overshoot and semiconvection in a theory of convection that will supersede mixing length theory, but this has not yet been realized in a stellar evolution code. For now, we must rely on multi-dimensional studies of novae to understand the degree to which overshoot mixes material at the boundary. To date, these simulations have been too expensive to carry out through much more than a single eddy turnover time, but a new software tool, MAESTRO (Nonaka et al., 2010) might be able to change that. MAESTRO is a multidimensional hydrodynamic code that essentially assumes that sound waves travel at infinite speed. For the very subsonic convective velocities at the base of the thermonuclear runaway, this is an excellent approximation. The end result is a simulation that can take

long enough timesteps to calculate through the entirety of the overshoot phase, which is a relatively short period of time over the course of the nova evolution, but an eternity compared to the dynamical time at the base of the convective zone.

With MAESTRO, we hope to better paramaterize how much mixing happens during the runaway. Combining such a parameterization with the improved diffusion and rotation capabilities in `MESA` will allow a more realistic simulation of shell flashes of all kinds on WDs, and in particular, we can answer the question of long-term mass growth of WDs undergoing rapid accretion of hydrogen.

5.2 Excitation of Core g-Modes

A more immediate outgrowth of this work is the open question still left from chapter 4: What *is* causing the observed oscillations in X-ray light curves?

We showed that the ϵ-mechanism could excite low-order modes, but those modes had periods much shorter than the observed periods. However, we also found modes at higher periods that were not excited by the ϵ-mechanism. If these modes could be excited by other means, they could still be the source of the observed oscillations.

One possible source of excitation would be stochastic excitation from the base of the convection zone during the thermonuclear runaway. This mechanism has been used by Fuller et al. (2015) to explain angular momentum transport via waves in massive stars and by Fuller (2017) to explain heat transport in pre-supernova supergiants.

With stochastic excitation, waves are generated by the motions of fluid elements at

the convective boundary. The generated waves have periods on the order of the convective turnover time,

$$P_{\rm wave} \sim \frac{\alpha_{\rm MLT} H}{v_{\rm conv}}, \tag{5.1}$$

where $\alpha_{\rm MLT}$ is the mixing length in units of the pressure scale height H and $v_{\rm conv}$ is the convective velocity. Near the base of the convective zone of our 1.3 $M_\odot$ model from chapter 4 during peak burning, the eddy turnover times are about 20 seconds, close to the 35 second period seen in several of the novae with masses estimated to be near 1.3 $M_\odot$.

The energy put into these waves is roughly

$$L_{\rm waves} \sim \mathcal{M} L_{\rm conv}, \tag{5.2}$$

where $\mathcal{M}$ is the mach number of the convective motion, which is typically a few percent, and $L_{\rm conv}$ is the energy carried by convection, which can easily exceed 10^9 $L_\odot$ in novae.

From the `MESA` calculations we've already done, we can estimate the total amount of energy put into these modes. What remains to be done is to use `GYRE` to see how fast this energy is radiatively damped. If the waves can survive through the outburst through to the supersoft phase, they may indeed explain the observed oscillations.

Appendix A

Phase Delays in CNO Burning

To calculate the sensitivity of the CNO burning rate to density and temperature perturbations, we followed the method of Kawaler (1988) with several changes. For completeness, we outline the entire calculation here.

Thermonuclear burning in the post-outburst nova is dominated by the CNO cycle. We consider only the basic CN cycle since it produces most of the energy. The reactions involved are

$$
\begin{aligned}
{}^{12}\mathrm{C} + p &\rightarrow {}^{13}\mathrm{N} + \gamma, && \text{(A.1)}\\
{}^{13}\mathrm{N} &\rightarrow {}^{13}\mathrm{C} + e^{+} + \nu_e, && \text{(A.2)}\\
{}^{13}\mathrm{C} + p &\rightarrow {}^{14}\mathrm{N} + \gamma, && \text{(A.3)}\\
{}^{14}\mathrm{N} + p &\rightarrow {}^{15}\mathrm{O} + \gamma, && \text{(A.4)}\\
{}^{15}\mathrm{O} &\rightarrow {}^{15}\mathrm{N} + e^{+} + \nu_e, && \text{(A.5)}\\
{}^{15}\mathrm{N} + p &\rightarrow {}^{12}\mathrm{C} + \alpha. && \text{(A.6)}
\end{aligned}
$$

We will index the reactants of equations (A.1)–(A.6) as 1–6. That is, ^{12}C will be denoted by the number 1 in subscripts and ^{15}N by 6. These indices will be cyclic so that $1 - 1 = 6$

and $6 + 1 = 1$.

For an isotope i that is both produced and destroyed via proton captures, the total number of ions of isotope i is represented by N_i. Then the net rate of production of these isotopes is

$$\frac{DN_i}{Dt} = -N_i n_p \langle \sigma v \rangle_i + N_{i-1} n_p \langle \sigma v \rangle_{i-1}, \tag{A.7}$$

where D/Dt is the Lagrangian time derivative, n_p is the number density of protons, and the $\langle \sigma v \rangle$'s are the thermally-averaged reaction rates. If the isotope is created via a beta decay, the second term is replaced by $N_{i-1}\lambda_{i-1}$ where λ_{i-1} is the decay rate of isotope $i-1$. Similarly, if the isotope is destroyed by a beta decay, then we replace the first term in (A.7) with $-N_i\lambda_i$. The total number of ions of isotopes is related to its mass fraction X_i and mass number A_i via $N_i \propto X_i/A_i$. Thus we can rewrite (A.7) in terms of the mass fraction via

$$\frac{DN_i}{Dt} \propto \frac{1}{A_i}\frac{DX_i}{dt}. \tag{A.8}$$

For simplicity, we also introduce a generalized destruction rate, K_i that is λ_i for isotopes destroyed via beta decay and $n_p \langle \sigma v \rangle_i$ for those destroyed by proton captures. This gives a generalized rate equation of

$$\frac{DX_i}{Dt} = -X_i K_i + \frac{A_i}{A_{i-1}} X_{i-1} K_{i-1}. \tag{A.9}$$

In the background equilibrium state, these rates all vanish once the mass fractions have settled to the preferred configuration. Now we introduce Lagrangian perturbations

(denoted by the δ symbol) in temperature and density with frequency σ,

$$\rho \rightarrow \rho_0 + \delta\rho\, e^{i\sigma t} \qquad T \rightarrow T_0 + \delta T\, e^{i\sigma t}, \tag{A.10}$$

where subscripts of 0 indicate the constant equilibrium values. The generalized destruction rates, K_i will also change, but only for reactions involving proton captures:

$$K_i = \lambda_i \rightarrow \lambda_{i,0} \qquad K_i = n_p \left\langle \sigma v \right\rangle_i \rightarrow K_{i,0} + K_{i,0} \left[\frac{\delta\rho}{\rho} + \nu_i \frac{\delta T}{T} \right] e^{i\sigma t}, \tag{A.11}$$

where $\nu_i = d \ln \left\langle \sigma v \right\rangle_i / d \ln T$. Similarly, the mass fractions X_i and their derivatives will also change:

$$X_i \rightarrow X_{i,0} + \delta X_i\, e^{i\sigma t} \qquad \frac{DX_i}{Dt} \rightarrow i\sigma \delta X_i\, e^{i\sigma t}. \tag{A.12}$$

Phase lags will only be present if the values of δX_i are complex. Now applying the perturbations of (A.11) and (A.12) to (A.9), subtracting off the equilibrium solution, and dividing out the exponential dependence gives

$$i\sigma \delta X_i = -\left(\delta X_i K_{i,0} + X_{i,0} \delta K_i\right) + \frac{A_i}{A_{i-1}} \left(\delta X_{i-1} K_{i-1,0} + X_{i-1,0} \delta K_{i-1}\right), \tag{A.13}$$

where we've left the perturbation of the generalized rate as a generic δK_i. Specializing to the three classes of isotopes (creation by beta decay, destruction by beta decay, or no beta decays) and noting that by conservation of mass,

$$\frac{A_i}{A_{i-1}} \left(\delta X_{i-1} K_{i-1,0} + X_{i-1,0} \delta K_{i-1}\right) = X_{i,0} K_{i,0} \left(\frac{\delta X_{i-1}}{X_{i-1,0}} + \frac{\delta K_{i-1}}{K_{i-1,0}} \right), \tag{A.14}$$

we get

$$i\frac{\sigma}{K_{i,0}}\frac{\delta X_i}{X_{i,0}} = -\left(\frac{\delta X_i}{X_{i,0}} + \frac{\delta K_i}{K_{i,0}}\right) + \left(\frac{\delta X_{i-1}}{X_{i-1,0}} + \frac{\delta K_{i-1}}{K_{i-1,0}}\right), \quad \text{(A.15)}$$

$$\frac{i\sigma + K_{i,0}}{K_{i,0}}\frac{\delta X_i}{X_{i,0}} - \frac{\delta X_{i-1}}{X_{i-1,0}} = \frac{\delta K_{i-1}}{K_{i-1,0}} - \frac{\delta K_i}{K_{i,0}}, \quad \text{(A.16)}$$

$$\frac{i\sigma + K_{i,0}}{K_{i,0}}\frac{\delta X_i}{X_{i,0}} - \frac{\delta X_{i-1}}{X_{i-1,0}} = (\nu_{i-1} - \nu_i)\frac{\delta T}{T_0} \qquad (i = 1, 4), \quad \text{(A.17)}$$

$$\frac{i\sigma + \lambda_i}{\lambda_i}\frac{\delta X_i}{X_{i,0}} - \frac{\delta X_{i-1}}{X_{i-1,0}} = \frac{\delta\rho}{\rho_0} + \nu_{i-1}\frac{\delta T}{T_0} \qquad (i = 2, 5), \quad \text{(A.18)}$$

$$\frac{i\sigma + K_{i,0}}{K_{i,0}}\frac{\delta X_i}{X_{i,0}} - \frac{\delta X_{i-1}}{X_{i-1,0}} = -\frac{\delta\rho}{\rho_0} - \nu_i\frac{\delta T}{T_0} \qquad (i = 3, 6). \quad \text{(A.19)}$$

Here (A.16) is still a general result while (A.17) - (A.19) relate the relative mass fraction perturbations to the equilibrium conditions and the temperature and density perturbations for isotopes that are created and destroyed by proton captures (A.17), created by proton captures and destroyed by beta decays (A.18), and created by beta decays and destroyed by proton captures (A.19). These constitute a set of six equations in six unknowns. For a given temperature, density, and equilibrium set of abundances, we can then query the `rates` module of `MESA` to get λ_i, $K_{i,0}(\rho_0, T_0)$, and $\nu_i(T_0)$ to get an expression for δX_i in terms of σ, $\delta T/T_0$, and $\delta\rho/\rho_0$. In general, this has the form

$$\frac{\delta X_i}{X_{i,0}} = \left(\alpha\frac{\delta\rho}{\rho_0} + \beta\frac{\delta T}{T_0}\right)e^{i\sigma t}, \quad \text{(A.20)}$$

where the α's and β's come from solving the system of equations above. They depend only on the various K_i's, ν_i's, and σ. They are in general complex, giving rise to phase delays between the temperature/density perturbation and the actual changes in abundances. Kawaler (1988) solved for these α's and β's explicitly in the limit where beta decays occur much more quickly than proton captures. This limit is valid in the case

of a PNN, but at the higher temperatures present in some of the post-outburst novae, this assumption fails, so the full matrix inversion calculation is needed to solve for these quantities.

To see how this affects wave excitation via the ϵ-mechanism, we need to relate these α's and β's to the nuclear energy generation rate. The energy generation rate due to the destruction of species i is given by

$$\epsilon_i = \frac{X_i K_i Q_i}{A_i m_p}, \tag{A.21}$$

where K_i is again the generalized destruction rate and Q_i is the energy released by the destruction of one isotope (roughly the difference in binding energies). Then the total energy generation rate is just the sum over all of these rates. After accounting for the perturbations in K_i and X_i, the perturbation in the overall energy generation rate is

$$\frac{\delta\epsilon}{\epsilon_0} = \left(A\frac{\delta\rho}{\rho_0} + B\frac{\delta T}{T_0} \right) e^{i\sigma t}, \tag{A.22}$$

where

$$A = \frac{d\ln\epsilon}{d\ln\rho} = \frac{(\sum_i \alpha_i\epsilon_i) + \epsilon_1 + \epsilon_3 + \epsilon_4 + \epsilon_6}{\epsilon_0} \tag{A.23}$$

and

$$B = \frac{d\ln\epsilon}{d\ln T} = \frac{(\sum_i \beta_i\epsilon_i) + \nu_1\epsilon_1 + \nu_3\epsilon_3 + \nu_4\epsilon_4 + \nu_6\epsilon_6}{\epsilon_0}. \tag{A.24}$$

In the long-period limit $\sigma \to 0$, we expect $A \to 1$, but in general, $A < 1$ for periods in the 1-1000 second range. Similarly, B is smaller than the expected unperturbed value for periods in this range, causing an enhanced stability in the burning rate with changes

to temperature and densities.

As a simple check that our method is consistent with the work of Kawaler (1988), the left panel of Figure A.1 reproduces Figure 3 of that paper, where the derivatives $A = d\ln\epsilon_{\rm nuc}/d\ln\rho$ and $B = d\ln\epsilon_{\rm nuc}/d\ln T$ are plotted for a particular temperature, density, and composition. We find excellent agreement with our general approach. The right panel of Figure A.1 shows how the actual values of A and B vary as a function of period for our fiducial 1.3 $M_\odot$ post-outburst nova model as well as a much hotter version of that model, demonstrating that temperature and density sensitivity indeed vanish at such high temperatures as the reaction cycle becomes limited by beta decays.

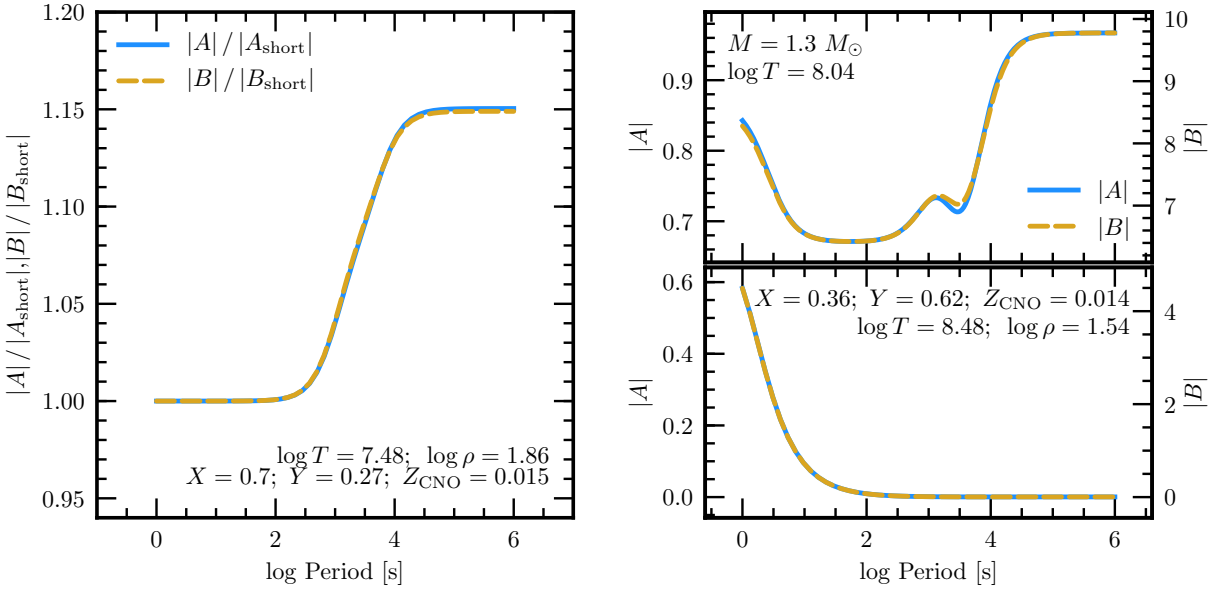

Figure A.1 **Left:** dependence of the logarithmic derivatives of the nuclear energy generation rate (relative to the long-period limit) on pulsation period. This figure corroborates the similar Figure 3 from Kawaler (1988). **Right:** the actual values of these derivatives for our fiducial 1.3 $M_\odot$ post-outburst nova model (top) and for a much hotter (3×10^8 K) model with the same composition and density.

Generally, A and B are local quantities since they depend on the local equilibrium

values for the X_i, ρ and T. Since we needed values for A and B at a large range of periods for computations with `GYRE` and for every snapshot saved during the post-outburst phase, we decided to simply sample the point of peak CNO burning and apply the modified values of A and B to all regions with significant burning. The area of peak burning is what drives the ϵ-mechanism, so this is the value and location that matters most.

To incorporate the phase lags defined above, we modify `GYRE` so that the $\epsilon_{\rm ad}$ and ϵ_S partial derivatives are evaluated via the expressions

$$\epsilon_{\rm ad} \equiv \left(\frac{\partial \ln \epsilon}{\partial \ln P}\right)_S = \frac{A}{\Gamma_1} + \nabla_{\rm ad} B, \tag{A.25}$$

$$\epsilon_{\rm S} \equiv c_P \left(\frac{\partial \ln \epsilon}{\partial S}\right)_P = -\upsilon_T A + B, \tag{A.26}$$

(all symbols have the same meaning as in Townsend et al. (2017)). For efficiency reasons, the complex coefficients A and B are pre-calculated on tables spanning a range of periods, and interpolated at runtime using cubic splines. These new capabilities will be included in version 5.1 of `GYRE`.

Bibliography

Alexakis, A., Calder, A. C., Heger, A., et al. 2004, ApJ, 602, 931

Arnett, W. D., Meakin, C., Viallet, M., et al. 2015, ApJ, 809, 30

Austin, S. J., Wagner, R. M., Starrfield, S., et al. 1996, Astronomical Journal v.111, 111, 869

Baker, J. G., & Menzel, D. H. 1938, ApJ, 88, 52

Beardmore, A. P., Osborne, J. P., & Page, K. L. 2013, The Astronomer's Telegram, 5573

Beardmore, A. P., Balman, S., Osborne, J. P., et al. 2010, The Astronomer's Telegram, 2423

Beardmore, A. P., Osborne, J. P., Page, K. L., et al. 2012, A&A, 545, 116

Beck, H., Gail, H. P., Gass, H., & Sedlmayr, E. 1990, Astronomy and Astrophysics (ISSN 0004-6361), 238, 283

Bildsten, L., Ushomirsky, G., & Cutler, C. 1996, ApJ, 460, 827

Bode, M. F., & Evans, A. 2008, Classical Novae

Bode, M. F., Darnley, M. J., Beardmore, A. P., et al. 2016, ApJ, 818, 145

Brandi, E., Quiroga, C., Mikołajewska, J., Ferrer, O. E., & García, L. G. 2009, A&A, 497, 815

Brooks, J., Bildsten, L., Schwab, J., & Paxton, B. 2016, ApJ, 821, 28

Casanova, J., José, J., García-Berro, E., Calder, A., & Shore, S. N. 2010, A&A, 513, L5

—. 2011a, A&A, 527, A5

Casanova, J., José, J., García-Berro, E., Shore, S. N., & Calder, A. C. 2011b, Nature, 478, 490

Cassisi, S., Iben, I. J., & Tornambe, A. 1998, ApJ, 496, 376

Crampton, D., Cowley, A. P., Hutchings, J. B., et al. 1987, ApJ, 321, 745

Cunningham, T., Wolf, W. M., & Bildsten, L. 2015, ApJ, 803, 76

Darnley, M. J., Williams, S. C., Bode, M. F., et al. 2014, A&A, 563, L9

Denissenkov, P. A., Herwig, F., Bildsten, L., & Paxton, B. 2013, ApJ, 762, 8

Downen, L. N., Iliadis, C., José, J., & Starrfield, S. 2013, ApJ, 762, 105

Draine, B. T. 2011, Physics of the Interstellar and Intergalactic Medium by Bruce T. Draine. Princeton University Press

Drake, J. J., Wagner, R. M., Starrfield, S., et al. 2003, ApJ, 584, 448

Durisen, R. H. 1977, ApJ, 213, 145

Eddington, A. S. 1926, The Internal Constitution of the Stars

Eyres, S. P. S., Davis, R. J., & Bode, M. F. 1996, MNRAS, 279, 249

Ferland, G. J., & Shields, G. A. 1978, ApJ, 226, 172

Ferland, G. J., Porter, R. L., van Hoof, P. A. M., et al. 2013, Revista Mexicana de Astronomía y Astrofísica Vol. 49, 49, 137

Fontaine, G., Graboske, Jr., H. C., & van Horn, H. M. 1977, ApJS, 35, 293

Fujimoto, M. Y. 1982a, ApJ, 257, 767

—. 1982b, ApJ, 257, 752

Fuller, J. 2017, MNRAS, 470, 1642

Fuller, J., Cantiello, M., Lecoanet, D., & Quataert, E. 2015, ApJ, 810, 101

Gallagher, J. S., & Starrfield, S. 1978, ARA&A, 16, 171

Gehrz, R. D., Grasdalen, G. L., Hackwell, J. A., & Ney, E. P. 1980, ApJ, 237, 855

Gehrz, R. D., Truran, J. W., Williams, R. E., & Starrfield, S. 1998, PASP, 110, 3

Geisel, S. L., Kleinmann, D. E., & Low, F. J. 1970, ApJ, 161, L101

Glasner, S. A., & Livne, E. 1995, ApJ, 445, L149

Glasner, S. A., Livne, E., & Truran, J. W. 1997, ApJ, 475, 754

—. 2005, ApJ, 625, 347

—. 2007, ApJ, 665, 1321

Glasner, S. A., Livne, E., & Truran, J. W. 2012, MNRAS, 427, 2411

Hachisu, I., & Kato, M. 2010, ApJ, 709, 680

Hachisu, I., Kato, M., & Nomoto, K. 1996, ApJL, 470, L97

Hansen, C. J., Kawaler, S. D., & Trimble, V. 2004, Stellar interiors : physical principles, structure, and evolution

Henze, M., Darnley, M. J., Kabashima, F., et al. 2015, A&A, 582, L8

Henze, M., Ness, J. U., Darnley, M. J., et al. 2014a, A&A, 563, L8

Henze, M., Pietsch, W., Haberl, F., et al. 2010, A&A, 523, A89

Henze, M., Pietsch, W., Haberl, F., et al. 2011, A&A, 533, 52

—. 2013, A&A, 549, 120

—. 2014b, A&A, 563, 2

Heywood, I., O'Brien, T. J., Eyres, S. P. S., Bode, M. F., & Davis, R. J. 2005, MNRAS, 362, 469

Hillman, Y., Prialnik, D., Kovetz, A., & Shara, M. M. 2016, ApJ, 819, 168

Hjellming, R. M., Wade, C. M., Vandenberg, N. R., & Newell, R. T. 1979, AJ, 84, 1619

Iben, Jr., I., Fujimoto, M. Y., & MacDonald, J. 1992, ApJ, 388, 521

Iben, I. J. 1982, ApJ, 259, 244

Iben, I. J., & Tutukov, A. V. 1989, ApJ, 342, 430

Iglesias, C. A., & Rogers, F. J. 1993, ApJ, 412, 752

—. 1996, Astrophysical Journal v.464, 464, 943

Jurdana-Šepić, R., Ribeiro, V. A. R. M., Darnley, M. J., Munari, U., & Bode, M. F. 2012, A&A, 537, A34

Kahabka, P., & van den Heuvel, E. P. J. 1997, ARA&A, 35, 69

Kato, M., & Hachisu, I. 1994, ApJ, 437, 802

Kato, M., Saio, H., & Hachisu, I. 1989, ApJ, 340, 509

Kato, M., Saio, H., Hachisu, I., & Nomoto, K. 2014, ApJ, 793, 136

Kawaler, S. D. 1988, ApJ, 334, 220

Kenyon, S. J. 1986, The symbiotic stars

Kercek, A., Hillebrandt, W., & Truran, J. W. 1998, A&A, 337, 379

—. 1999, A&A, 345, 831

Kippenhahn, R., & Thomas, H.-C. 1978, A&A, 63, 265

Kovetz, A., & Prialnik, D. 1994, ApJ, 424, 319

Krautter. 2008, Classical Novae, 2nd edn., ed. M. F. Bode & A. Evans (Cambridge University Press), 232

Kupfer, T., Steeghs, D., Groot, P. J., et al. 2016, MNRAS, 457, 1828

Kutter, G. S., & Sparks, W. M. 1987, ApJ, 321, 386

Lang, K. R. 1980, Astrophysical Formulae: a compendium for the physicist and astrophysicist, 2nd edn. (Berlin ; New York : Springer-Verlag)

Langer, N., Deutschmann, A., Wellstein, S., & Höflich, P. 2000, A&A, 362, 1046

Livio, M., Prialnik, D., & Regev, O. 1989, ApJ, 341, 299

Livio, M., & Truran, J. W. 1987, ApJ, 318, 316

Lodders, K. 2003, ApJ, 591, 1220

MacDonald, J. 1983, ApJ, 273, 289

MacDonald, J., & Vennes, S. 1991, ApJ, 373, L51

Maoz, D., Mannucci, F., & Nelemans, G. 2014, ARA&A, 52, 107

Massacrier, G., Potekhin, A. Y., & Chabrier, G. 2011, Phys. Rev. E, 84, 056406

Michaud, G., Alecian, G., & Richer, J. 2015, Atomic Diffusion in Stars

Mikolajewska, J., Friedjung, M., Kenyon, S. J., & Viotti, R., eds. 1988, Astrophysics and Space Science Library, Vol. 145, The symbiotic phenomenon

Ness, J. U., Schwarz, G., Starrfield, S., et al. 2008, AJ, 135, 1328

Ness, J. U., Starrfield, S., Burwitz, V., et al. 2003, ApJ, 594, L127

Ness, J. U., Schwarz, G. J., Page, K. L., et al. 2013, The Astronomer's Telegram, 5626

Ness, J.-U., Kuulkers, E., Henze, M., et al. 2014, The Astronomer's Telegram, 6147

Ness, J.-U., Beardmore, A. P., Osborne, J. P., et al. 2015, A&A, 578, A39

Ney, E. P., & Hatfield, B. F. 1978, ApJ, 219, L111

Nomoto, K. 1982, ApJ, 253, 798

Nomoto, K., Nariai, K., & Sugimoto, D. 1979, PASJ, 31, 287

Nomoto, K., Saio, H., Kato, M., & Hachisu, I. 2007, ApJ, 663, 1269

Nomoto, K., Thielemann, F. K., & Yokoi, K. 1984, ApJ, 286, 644

Nonaka, A., Almgren, A. S., Bell, J. B., et al. 2010, ApJS, 188, 358

Odendaal, A., Meintjes, P. J., Charles, P. A., & Rajoelimanana, A. F. 2014, MNRAS, 437, 2948

Oegelman, H., Beuermann, K., & Krautter, J. 1984, ApJ, 287, L31

Orio, M. 2006, ApJ, 643, 844

Orio, M., Nelson, T., Bianchini, A., Di Mille, F., & Harbeck, D. 2010, ApJ, 717, 739

Osborne, J. P., Page, K. L., Beardmore, A. P., et al. 2011, ApJ, 727, 124

Paczynski, B. 1970, Acta Astronomica, 20, 47

—. 1983, ApJ, 264, 282

Paczynski, B., & Zytkow, A. N. 1978, ApJ, 222, 604

Paxton, B., Bildsten, L., Dotter, A., et al. 2011, ApJS, 192, 3

Paxton, B., Cantiello, M., Arras, P., et al. 2013, ApJS, 208, 4

Paxton, B., Marchant, P., Schwab, J., et al. 2015, ApJS, 220, 15

Piersanti, L., Cassisi, S., Iben, I. J., & Tornambe, A. 1999, ApJ, 521, L59

Piro, A. L. 2008, ApJ, 679, 616

Prialnik, D., & Kovetz, A. 1995, ApJ, 445, 789

Rauch, T., Orio, M., Gonzales-Riestra, R., et al. 2010, ApJ, 717, 363

Robinson, E. L. 1976, ARA&A, 14, 119

Rosner, R., Alexakis, A., Young, Y.-N., Truran, J. W., & Hillebrandt, W. 2001, ApJ, 562, L177

Roy, N., Chomiuk, L., Sokoloski, J. L., et al. 2012, Bulletin of the Astronomical Society of India, 40, 293

Sala, G., & Hernanz, M. 2005, A&A, 439, 1061

Saumon, D., Chabrier, G., & van Horn, H. M. 1995, ApJS, 99, 713

Schaefer, B. E. 2010, ApJS, 187, 275

Schmidtke, P. C., & Cowley, A. P. 2006, AJ, 131, 600

Schwarz, G. J. 2002, ApJ, 577, 940

Schwarz, G. J., Shore, S. N., Starrfield, S., & Vanlandingham, K. M. 2007, ApJ, 657, 453

Schwarz, G. J., Ness, J.-U., Osborne, J. P., et al. 2011, ApJS, 197, 31

Seaquist, E. R., & Bode, M. F. 2008, Classical Novae, 2nd edn., ed. M. F. Bode & A. Evans (Cambridge University Press), 141

Seaquist, E. R., & Palimaka, J. 1977, ApJ, 217, 781

Shara, M. M., Prialnik, D., & Kovetz, A. 1993, ApJ, 406, 220

Shen, K. J., & Bildsten, L. 2007, ApJ, 660, 1444

—. 2009, ApJ, 692, 324

Shore, S. N. 2008, Classical Novae, 2nd edn., ed. M. F. Bode & A. Evans (Cambridge University Press), 194

Shore, S. N., Schwarz, G. J., De Gennaro Aquino, I., et al. 2013, A&A, 549, A140

Shore, S. N., Mason, E., Schwarz, G. J., et al. 2016, A&A, 590, A123

Sienkiewicz, R. 1980, A&A, 85, 295

Sion, E. M. 1999, PASP, 111, 532

Sion, E. M., Acierno, M. J., & Tomczyk, S. 1979, ApJ, 230, 832

Sparks, W. M., & Kutter, G. S. 1987, ApJ, 321, 394

Starrfield, S., Iliadis, C., & Hix, W. R. 2008, Classical Novae, 2nd edn., ed. M. F. Bode & A. Evans (Cambridge University Press), 77

Starrfield, S., Sparks, W. M., & Truran, J. W. 1974, ApJS, 28, 247

Szkody, P., Mukadam, A. S., Gänsicke, B. T., et al. 2012, ApJ, 753, 158

Takata, M. 2006, PASJ, 58, 893

Tang, S., Bildsten, L., Wolf, W. M., et al. 2014, ApJ, 786, 61

Taylor, A. R., Hjellming, R. M., Seaquist, E. R., & Gehrz, R. D. 1988, Nature (ISSN 0028-0836), 335, 235

Townsend, R. H. D. 2005, MNRAS, 360, 465

Townsend, R. H. D., Goldstein, J., & Zweibel, E. G. 2017, MNRAS

Townsend, R. H. D., & Teitler, S. A. 2013, MNRAS, 435, 3406

Townsley, D. M., & Bildsten, L. 2004, ApJ, 600, 390

—. 2005, ApJ, 628, 395

Tuchman, Y., & Truran, J. W. 1998, ApJ, 503, 381

van den Heuvel, E. P. J., Bhattacharya, D., Nomoto, K., & Rappaport, S. A. 1992, A&A, 262, 97

Vanlandingham, K. M., Schwarz, G. J., Shore, S. N., Starrfield, S., & Wagner, R. M. 2005, ApJ, 624, 914

White, N. E., Giommi, P., Heise, J., Angelini, L., & Fantasia, S. 1995, ApJ, 445, L125

Wolf, W. M., Bildsten, L., Brooks, J., & Paxton, B. 2013, ApJ, 777, 136

Yaron, O., Prialnik, D., Shara, M. M., & Kovetz, A. 2005, ApJ, 623, 398

Yoon, S. C., Langer, N., & Scheithauer, S. 2004a, A&A, 425, 217

Yoon, S. C., Langer, N., & van der Sluys, M. 2004b, A&A, 425, 207